Modification of Poly(lactic acid) by Melt Blending

A THESIS SUBMITTED TO THE FACULTY OF THE GRADUATE SCHOOL
OF THE UNIVERSITY OF MINNESOTA
BY

Liangliang Gu

IN PARTIAL FULFILLMENT OF THE REQUIREMENTS
FOR THE DEGREE OF
Ph.D.

Christopher W. Macosko and David C. Morse, Advisers

December, 2017

Abstract

Poly(lactic acid) (PLA), a renewable, biodegradable, and biocompatible polyester, is one of the most successful solutions to revolutionize renewable plastic production. Nevertheless, application of pristine PLA is largely limited by its brittleness in solid state and low melt strength in melt state. Various strategies have been developed to improve the performance of PLA, among which melt processing is the most viable and economical for industrial use. This thesis covers several independent aspects of PLA modification and presents some new possibilities in melt processing of PLA and PLA-based blends. Chapter 2 and Chapter 3 focus on branching of PLA with multifunctional aziridine to improve melt strength. Multifunctional aziridine as a branching agent has its advantage in fast reaction kinetics that leads to stable final product properties. Extensional rheology was extensively used to clarify the correlation between melt strength and chain structure. Chapter 4 seeks to toughen PLA by blending with poly(ethylene oxide)-poly(propylene oxide)-poly (ethylene oxide) (PEO-PPO-PEO) triblock copolymers, which are commercially known as Pluronic® (by BASF). Pluronic copolymers with large PPO block size and low PEO content can increase the elongation of break from 5% to more than 100% at a low loading of 5 wt.%, along with the additional benefits of reduced blend viscosity and easy mold-release. Chapter 5 and chapter 6 are less property-oriented, focusing on cocontinuous immiscible polymer blends. In Chapter 5, carboxylic acid/oxazoline reaction is used to compatibilize cocontinuous PLA/polystyrene (PS) blend. Reactively formed interfacial graft copolymer reduced the phase domain size to submicron scale, which is hard to achieve in melt-processed cocontinuous blends. Hierarchically porous PLA, with primary pore size 5 – 20 μm and secondary pore size 0.5 – 2 μm, was further made from compatibilized PLA/PS/linear low density polyethylene (LLDPE) blend after selective extraction of PS and LLDPE. By studying the wetting behavior of ternary PLA/PS/PE blend, we confirmed that PLA/PE interfacial tension is much higher than PLA/PS interfacial tension. Chapter 6 uses branched PE and PLA to study the effect of extensional viscosity on cocontinuity formation in immiscible polymer blends. Blending with two branched polymers broadened the range of cocontinuity. This was attributed to the ability of a strain hardening matrix to promote elongation, and hence percolation, of the minor phase.

Table of Contents

List of Figures

List of Tables

Chapter 1 Introduction

1.1 Poly(lactic acid) as a sustainable solution

With their advantages of light weight, high specific strength and low price, polymers have become indispensable in today's human society. [1] In 2015, 139 kg of plastics were consumed by each person in North America.[2] The largest market of plastics is packaging, which is growing rapidly due to the increase of single-use containers.[3] But the plastic production also leads to solid waste problems because most commodity plastics are derived from fossil hydrocarbons and it takes decades for them to degrade in the natural environment[4]. Only a small portion of those plastic wastes are incinerated for energy production. The majority are disposed to landfills or directly into the open environment.[5] In 2010, an estimated 4 – 12 million metric tons of plastic wastes ended up in the ocean.[6] Plastic debris causes many problems to the marine ecosystem, among which the ingestion of plastics by marine wildlife attracts the most public attention.[7] Contamination of fresh water systems and terrestrial habitats by plastic wastes is also increasingly reported.[8, 9] If current trends of plastic production and waste management continue, by 2050, 12,000 million metric tons of plastic waste will be in the landfills or in the environment, and the possible harm to natural environment is largely unknown.[3]

Another major concern about plastics is that the monomers used to make plastics, such as ethylene and styrene, come from natural gas and crude oil. As of 2014, roughly 8% of the world's annual gas and oil production were converted into plastics.[10 - 12] World economy and population growth is enlarging the global energy demand, which in turn speeds up the depletion of those non-renewable natural resources. Though not the ultimate solution, reducing the fossil fuel consumption in plastic industry would help relieve the energy security problem.[13] For these reasons, the polymer experts from both academic and industry have invested significant efforts into developing polymers that are more sustainable, including but not limited to poly(lactic acid) (also known as polylactide

or PLA), polyhydroxyalkanoates, poly(butylene succinate) and biopolyolefin.[5] In this context, polymers that can help reduce plastic solid wastes and fossil resource usage (degradable, recyclable, or derived from renewable resources) shall be considered as sustainable. In the long run, the sustainable polymers will gradually replace the oil-based polymers as they become more competitive in cost and performance.

PLA is the front runner of current sustainable polymers, with an expected worldwide production capacity of 800,000 tons/year by 2020.[14] It is renewable, biodegradable, biocompatible, and compostable. Current industrial practice employs ring-opening polymerization of lactide catalyzed by a Sn(II)-based catalyst to make PLA (Figure 1-1). Lactide is a six-membered cyclic dimer of lactic acid, which is produced from the fermentation of agricultural feedstocks.[15] The chiral nature of lactic acid results in distinct forms of polylactide, poly(L-lactide) (PLLA), poly(D-lactide) (PDLA), and poly(DL-lactide) (PDLLA), which are synthesized from the corresponding L-lactide, D-lactide, and meso-lactide, respectively[16]. The properties of PLA largely depend on the ratio of the L- to the D-isomers[17]. Isotactic PLAs are semicrystalline materials with a glass transition temperature (T_g) of 50 -70 °C, a melting temperature (T_m) between 170 and 190 °C, and a maximum crystallinity of 35% [18 - 21]. Thermal properties of PLA are also related to other factors such as molecular weight, thermal history, and purity. Increasing D-isomer content reduces glass transition temperature, melting temperature, and the ability to crystalize.[22, 23] PDLLA from meso-lactide is fully amorphous because of its irregular chain structure.[24]

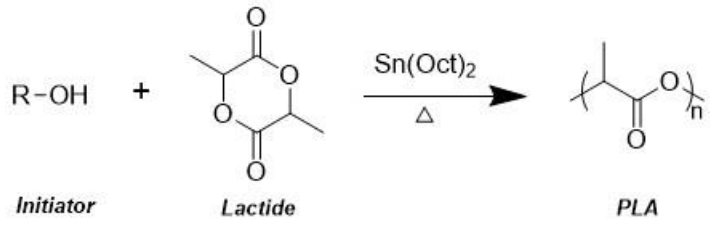

Figure 1-1 Ring-opening polymerization of lactide to make PLA.

1.2 Melt processing of PLA

Although sustainable, PLA has drawbacks as well. First, PLA is brittle. In a tensile test, the elongation at break of PLA only achieves ~ 10%. The lack of ductility imposes limitations on applications that require high toughness. It is worth mentioning that, PLA is "ductile" right after melt processing (elongation at break ~ 300%), but at room temperature it goes through physical aging which can lead to an elongation at break less than 10% within 24 hours.[25] Second, the melt strength of PLA is low. As a result, sagging and necking tends to occur in sheet extrusion process (Figure 1-2). Low melt strength also presents processing difficulties in blown film extrusion and foaming operations where elongational flow is involved. Third, during melt processing PLA parts are inherently tacky due to their high surface coefficient of friction.[19] Molded PLA has strong adhesion to the metal molds, which usually requires mold release agents to help remove the part from the mold. Other processing difficulties caused by high surface coefficient of friction include sticking of films to themselves or to rollers and difficulties in stacking of sheets or nesting of thermoformed parts. To overcome this problem, fatty acid amides are often added to PLA as slip agent. Fatty acid amides tend to migrate to the surface of the formed PLA parts, forming a crystalline structure that reduces the surface coefficient of friction.[19] Additionally, like other polyesters, PLA is susceptible to hydrolytic degradation in the melt state. Molecular weight drop would be significant if PLA is not properly dried before processing, which also compromises the end-product quality. PLA should be dried to <250 ppm moisture and maintained at this moisture level during melt processing.[26]

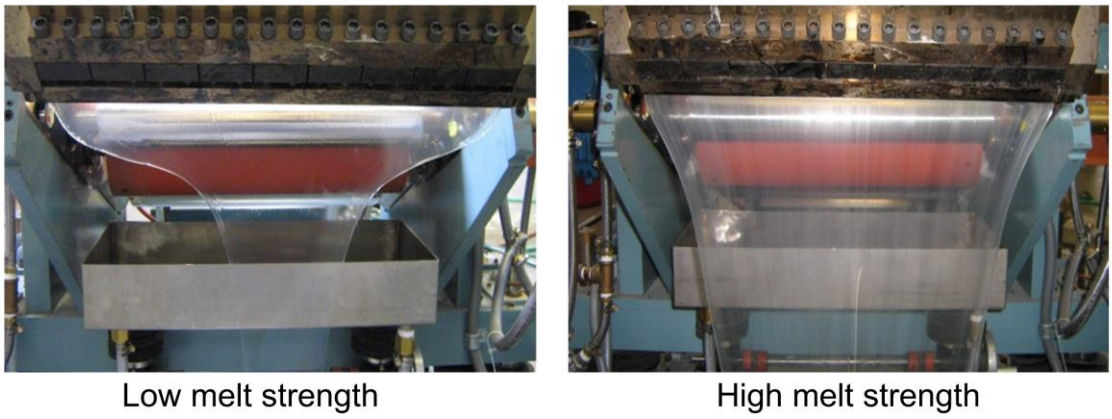

Figure 1-2 Necking of low melt strength PLA in sheet extrusion process. Images are from Interfacial Solutions LLC, now Stratsys Materials.

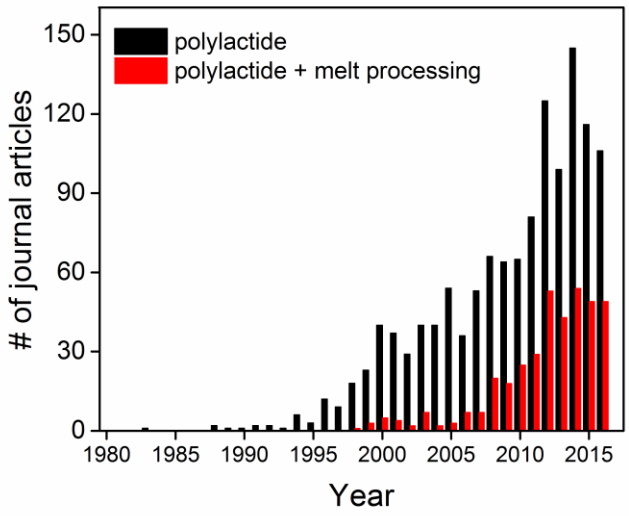

Figure 1-3 Number of peer-reviewed journal articles published on melt processing of PLA by Scholars Portal Search. The searching parameters are "polylactide in keywords" and "polylactide in keywords + melt processing in anywhere".

To improve the properties of PLA, additives are often needed. Melt processing is by far the most widely adopted method for introducing additives into PLA and converting PLA resins into various end products. The situation was very different before 2000 because of PLA's high cost.

The literature survey in Figure 1-3 shows the number of published journal articles on PLA's melt processing. There was almost no research on PLA's melt processing before 2000. The game-changing event occurred in the early 1990s when Cargill Inc. succeeded in producing high molecular weight PLA using the lactide ring opening reaction. [27 - 29] In 1997, the joint venture Cargill Dow LLC began the commercial production of PLA resins. At this landmark of transforming PLA from a specialty polymer to a commodity thermoplastic, melt processing of PLA came online owing to its large scale and easy production.

Typical melt processing involves the following steps: (a) heating the polymer above its melting temperature, (b) pumping the polymer to the shaping unit, (c) shaping the molten polymer into desired shapes and (d) cooling and solidification. The second step is most important for modifying PLA properties since melting blending with additives is accomplished in this step. The equipment for melt blending are single or twin screw extruders (Figure 1-4). Blending PLA with other flexible polymers is most extensively used method to improve the ductility of PLA[30], while reactive small molecules or oligomers are mixed with PLA to enhance its melt strength by generating branched chains. This thesis uses lab-scale twin screw mixing devices to modify PLA. The toughening and melt-strengthening aspects will be covered, together with general melt blending studies.

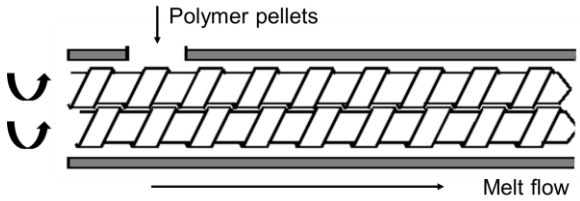

Figure 1-4 Illustration of a twin screw extruder.

1.3 Cocontinuous polymer blends

As stated in section 1.2, blending PLA with other polymers is an efficient way to enhance PLA toughness. It is of significance to understand the microstructure in PLA blends, of which cocontinuous blend is particularly interesting due to its morphological complexity. A large amount of work in this thesis is devoted to cocontinuous polymer blends of PLA, so it is essential to have a brief introduction for it.

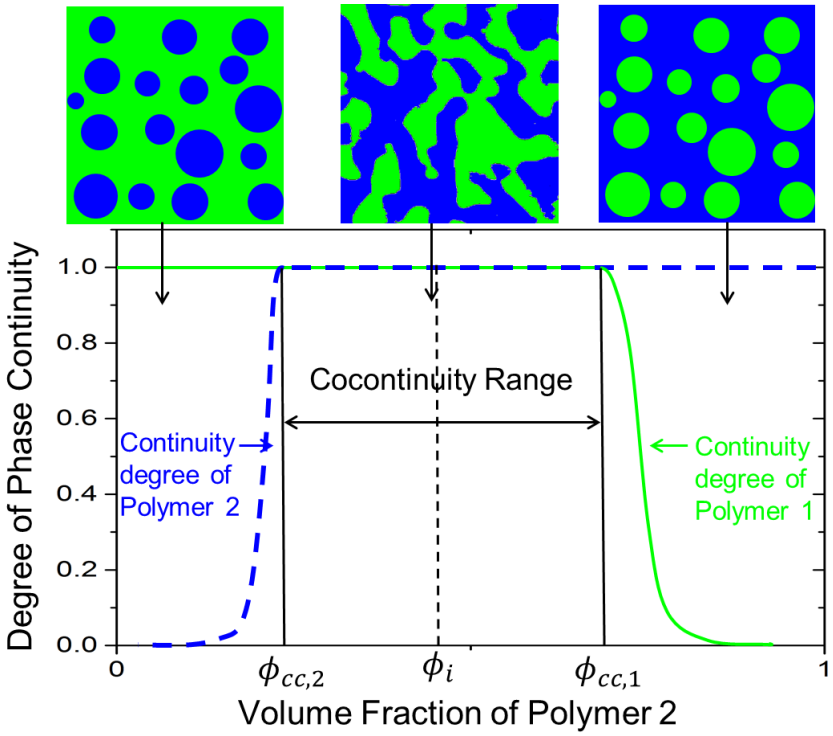

Figure 1-5 Morphology evolution of a typical immiscible binary polymer blend. Degree of phase continuity is the faction of the phase that is continuous through the sample. Dispersed droplets have a continuity degree of 0, while completely continuous phase have a degree of 1. The percolation threshold, $\phi_{d,cc}$, is the minimum volume fraction for a phase to form a single continuous path through the sample. Cocontinuity range is the composition range between $\phi_{d,cc,2}$ and $\phi_{d,cc,1}$.

For a specific immiscible binary polymer blend system (polymer 1 and polymer 2), its morphology is highly dependent on composition. As the volume fraction of polymer 2 is increased

from nearly 0% to almost 100%, in the most common cases, the blends go through a morphology evolution shown in Figure 1-5. When polymer 2 is low in volume fraction, it separates into droplets and its continuity degree is low (nearly 0). With the volume fraction of polymer 2 increasing, the droplets become bigger and gradually coalesce under the mixing flow and the continuity degree increases. At the percolation threshold, $\phi_{d,cc,2}$, a continuous polymer 2 phase (with continuity degree nearly 1) is formed while the polymer 1 phase is also continuous. This morphology (picture in middle of Figure 1-5), with both polymer 1 phase and polymer 2 phase continuous, is the cocontinuous morphology. Further increasing volume fraction of polymer 2, polymer 1 gradually turns into isolated droplets embedded in a polymer 2 matrix.

Most immiscible polymer blends form cocontinuous morphologies over a range of compositions. This range is referred to as the cocontinuity range. In the cocontinuity range, both phases have a continuity degree nearly 1. The phase inversion point, ϕ_i, is the composition at which the disperse phase tends to become continuous and vice- versa. Experimentally, it is treated as the middle point of the cocontinuity range. There are a lot of numerical models predicting ϕ_i, and most of the models use the viscosity ratio between two polymer phases as the principal parameter. The most popular model is the Jordhamo model[31, 32]

$$\frac{\phi_1}{\phi_2} = \frac{\eta_1(\dot{\gamma})}{\eta_2(\dot{\gamma})} \tag{1-1}$$

where ϕ_1 and ϕ_2 are the volume fractions of phase 1 and phase 2 at phase inversion point, while $\eta_1(\dot{\gamma})$ and $\eta_2(\dot{\gamma})$ are the viscosities of phase 1 and phase 2 under shear rate $\dot{\gamma}$. This model was derived from experimental observations.[33] Some later researches were consistent with this model while others refuted it.[34, 35] It was found that Jordhamo model predicted too strong of a dependence on the viscosity ratio. Later models, Ho model[36] and De Roover model[37], reduced its dependence on viscosity ratio. Several attempts were made to develop a theory which can predict the phase

inversion point of binary polymer blends. The Metelkin model[38] and Utracki model[39] are the most commonly used theory-based models.

All the models above only use one parameter, the viscosity ratio, which limits their accuracy. In 1988, Willemse[40 - 42] developed a different model that considered shape requirement for the droplets to percolate. The model can predict the lower percolation limit of cocontinuity range, $\phi_{d,cc}$,

$$\frac{1}{\phi_{d,cc}} = 1.38 + 0.0213\left(\frac{\eta_m \dot{\gamma}}{\Gamma} R_0\right)^{4.2} \tag{1-2}$$

where η_m is the shear viscosity of the major phase, $\dot{\gamma}$ is the shear rate, Γ is the interfacial tension between the blend components, and R_o is the equivalent sphere radius of a droplet that is stretched into a rod-like shape and is dependent on the particulars of the blending process. The upper limit can be given by an analogous formula in which the two components of the blend have changed role. A major drawback of this model is that the phase size R_0 must be measured after blending, so it is not a real predictive model. Anyway, the Willemse model shows some meaningful thinking about the edges of cocontinuity range while other models only deal with phase inversion point and more parameters (e.g. interfacial tension Γ) of the blending system are involved in this model. It is necessary to note that, those models suffered a lot to fit the experimental data.[43]

Another important aspect of immiscible cocontinuous polymer blends is stability, which is usually characterized by coarsening experiment. Immiscible polymer blends are thermodynamically unstable, and their morphology evolves into coarser structures when they are in melt state. The characteristic phase size of the blend is highly dependent on the coarsening rate. The rate of cocontinuous coarsening has been predicted by: [44, 45]

$$d(a)/dt = c\frac{\Gamma}{\eta} \tag{1-3}$$

where a is the characteristic phase size, Γ is the interfacial tension between the two phases, η is the overall blend viscosity, and c is a dimensionless prefactor. High interfacial tension and low blend viscosity result in fast coarsening. In order to prevent or minimize the effects of coarsening, cocontinuous blends are often compatibilized with an interfacial modifier. This can be either premade block copolymers [46], or reactively formed block and graft copolymers (reactive compatibilization) during melt processing [47, 48]. Reactive compatibilization involves adding complementary functional groups to some of the polymer chains in each phase. During blending, these functional groups can react at the interface, forming a block or graft copolymer. Figure 1-6 (a) gives the idea of reactively forming copolymer at interface and Figure 1-6 (b) provides an example that addition of premade block copolymer in a polyethylene (PE) / polystyrene (PS) blend stops the coarsening. Blends may also be stabilized by nanoparticles located at the interface.[49 - 53]

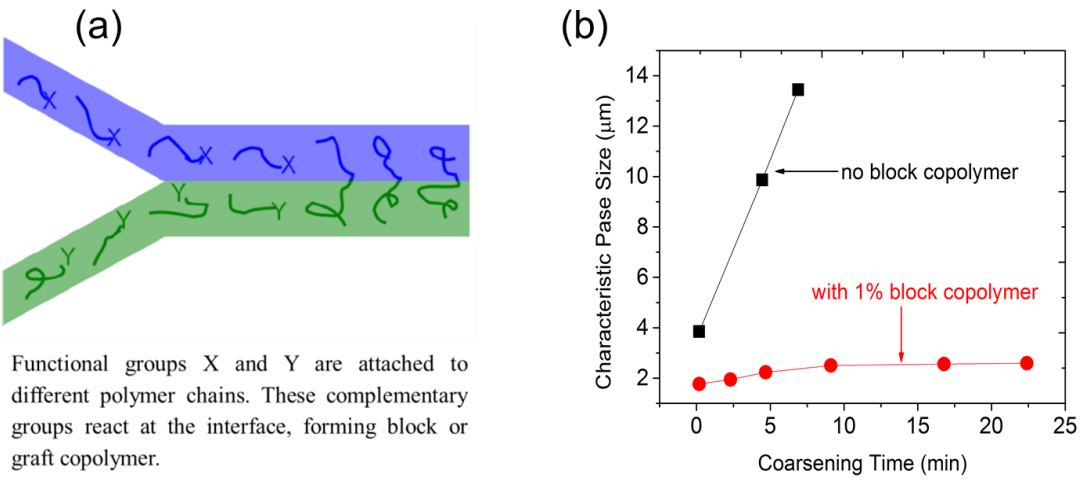

Functional groups X and Y are attached to different polymer chains. These complementary groups react at the interface, forming block or graft copolymer.

Figure 1-6 Compatibilization of immiscible polymer blends. (a) Reactive compatibilization. (b) Premade block copolymer stops coarsening. Reproduced from Lopez-Barron[54]: characteristic phase size vs annealing time at 170 °C for 50/50 PS/PE blends. (■) blends without block copolymer; (●) blends with 1wt% 28-10k PS-b-PE.

1.4 Thesis outline

This thesis presents some new possibilities to modify PLA for better properties and functions. The modification method throughout this thesis is melt blending.

Chapter 2 focused on improving the melt strength of PLA by introducing long chain branches. Industrial practices have used multifunctional epoxides to make branched PLA. But the reaction between epoxide and PLA is slow at the processing temperature for PLA. As a result of the unreacted functional groups, the viscosity of branched PLA will keep increasing in the following processing steps, which may lead to unpredictable difficulties like overloading the equipment. Here we take advantage of the fast reaction between aziridine functional group and PLA to make branched polymer. A commercially available trifunctional aziridine linker was melt blended with linear PLA to make star-shaped PLA. Long chain branched PLA was prepared by successive reactions of PLA with pyromellitic dianhydride (PMDA) and the aziridine linker. Rheological properties of the resulting materials were stable due to the completed reaction. Significant strain hardening in extensional flow was observed for the long chain branched PLA, indicating improved melt strength. A comparison with PLA branched by the commercial linker Joncryl revealed that Joncryl-branched PLA possesses a “comb-star” topology, which is not ideal for processing.

Chapter 3 takes a step further to study the effect of chain structure (mainly spacing between branching points) on PLA’s extensional rheology. Comb-shaped aziridine-functional linkers with different chain length were synthesized and melt blended with linear PLA. Compared to the linker with small spacing between branch points, linker with large spacing increased the extensional hardening at high strain rates and gave less increase in shear viscosity. We propose that a spacing of entanglement molecular weight would be suitable for PLA’s melt processing.

In Chapter 4, commercially available poly(ethylene oxide)-poly(propylene oxide)-poly(ethylene oxide) (PEO-PPO-PEO) block copolymers were blended with PLA to improve toughness for applications that require transparency. The miscibility of PLA with copolymers decreased as the molecular weight and the PPO fraction of the copolymer increase. For the phase-separated blends, the copolymers dispersed in PLA matrix as droplets, and the droplet size increased with immiscibility. The toughness also increased with immiscibility. In the best case, the blends' tensile toughness achieved 17 times of neat PLA at loading of 5 wt.%. In phase separated blends, Pluronic copolymer can migrate to the surface of PLA and serve as lubricant, which significantly reduced the viscosity and surface friction. This is beneficial for reducing processing cost and solving sticking problem of PLA products.

In Chapter 5, new function of PLA is developed by creating hierarchically porous structure. We first demonstrated the generation of submicron pores by reactive compatibilization of cocontinuous polymer blend. Hierarchically structured "tri-continuous" morphology was further obtained in ternary PLA/polystyrene (PS)/polyethylene (PE) blends. Porous PLA was made by selectively removing the PS and PE phases. The underlying thermodynamic mechanism for the formation of hierarchical morphology in PS/PLA/PE blend was studied, and it was found that PLA/PS/PE ternary blends show complete wetting behavior with PS located at PLA/PE interface. This observation confirmed that the PE/PLA interfacial tension is much higher than PS/PLA interfacial tension.

In continuation of Chapter 5, Appendix 1 combines fused deposition modeling and cocontinuous polymer blends to prepare hierarchically porous PLA. The primary pore size can be adjusted by computer aided design (0.5 – 2 mm) and the secondary pores with connected, fibrous morphology can be controlled by compatibilization. Chapter 6 studies the effect of extensional viscosity on cocontinuity formation in immiscible blends. It was found that adding a branched

polymer to the blend allowed the other blend component to percolate into a continuous network with less material.

Chapter 2 PLA branching with tri-functional aziridine: improving melt strength*

2.1 Background

As mentioned in Chapter 1, due to its low melt strength, PLA usually shows unsatisfying performance in melt processes that involve stretching and drawing (i.e. film blowing, sheet/film extrusion, thermoforming, and foaming). In this context, melt strength is an engineering measure of a polymer melt's resistance to extensional deformation [55]. Based on previous studies on polyethylene and polypropylene[56, 57], one of the most effective ways to increase melt strength is to introduce long chain branches (LCB) into the polymer. Polymer melts with LCB structure show "extensional hardening" phenomena in uniaxial extension flow that differs from the behavior of unbranched melts. "Extensional hardening" means that during the start-up of extension, the elongational viscosity rises above the linear viscoelastic response (Figure 2-1).

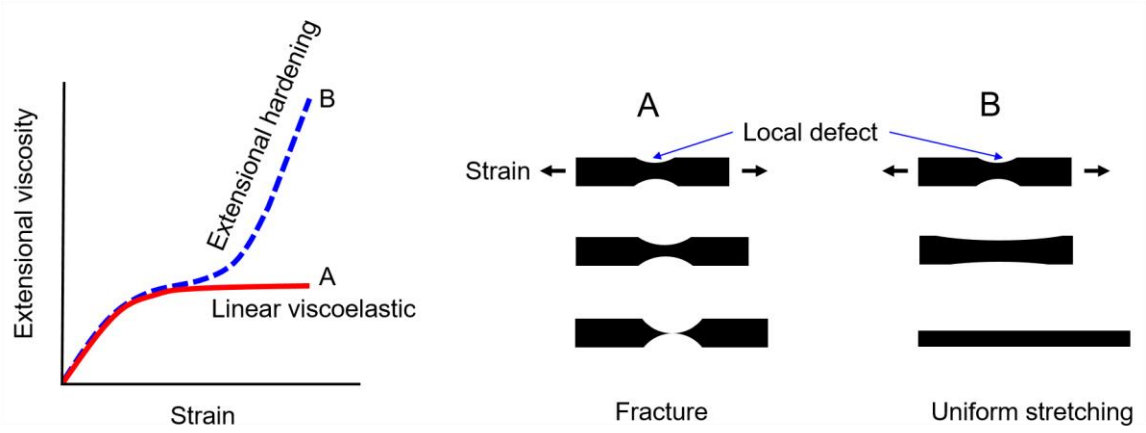

Figure 2-1 Extensional hardening promotes stable elongational flow of polymer melt.

* Reproduced in part from "L. Gu, Y. Xu, G.W. Fahnhorst, C.W. Macosko, J. Rheol. 61 (2017) 785–796". Financial support for this work came from the National Science Foundation through the Center for Sustainable Polymers (CHE-1413862).

Extensional hardening can increase melt strength by the so called “self-healing” mechanism. If any local region became thinner, and therefore more strained than the surrounding regions, its viscosity would be higher and deformation would be more difficult. The thinning would then be passed on to the surrounding low viscosity regions, leading to more uniform deformation of the entire part, without undergoing run-away thinning or “necking”, which results in rupture. Another method to increase melt strength is to add an ultra-high molecular weight component into linear polymer [58], however in ring-opening and condensation polymerization the maximum molecular weight is limited by equilibration and long reaction times.

Several strategies have been developed to create branched PLA. Intuitively, building a branched structure during ring-opening polymerization of lactide is a direct method. Multifunctional initiators and comonomers, including polyols[59], polysaccharides[60, 61], poly(vinyl alcohol) [62], mevalonolactone [63], glycidol [64], 2,2-bis(hydroxyethyl)-butyric acid [65] have been polymerized with lactide to make branched PLA with well-controlled chain topology. However, due to the low price of commercially available linear PLA, post-polymerization chain modification is more economically viable than direct synthesis routes. Recently, linear PLA has been branched by UV radiation [66] or high energy irradiation with electrons or γ-rays in the presence of multifunctional acrylates [67 - 69]. This strategy requires pre-mixing PLA with multifunctional acrylates otherwise PLA degradation dominates.

The most common and convenient method to carry out post-polymerization branching is via reactive melt processing. This approach requires either the use of free radicals[70 - 73] or end group reactions. In the former case, organic peroxides are used as a free radical source. Carlson et. al reported increased molecular weight and melt viscosity after PLA melt extrusion with 2,5-dimethyl-2,5-di(tert-butylperoxy) under certain extrusion conditions[70]. Dean et. al studied the steady and dynamic rheology as well as melt strength of PLA branched with lauroyl peroxide.

Increases in viscosity and melt strength were observed[71]. Other works used multifunctional acrylates as branching agent in addition to organic peroxides. Cernohous et. al prepared branched PLA by melt blending linear PLA with acrylated polyethersiloxane/ethoxylated pentaerythritol tetraacrylate and dicumyl peroxide[73]. LCB structure was confirmed by strong strain hardening behavior in extensional rheology[74]. The multifunctional acrylate is a crucial component for the formation of a LCB structure in free radical branching processes. In terms of topology, free radical reactions occur randomly along the polymer backbone, allowing for each chain to be branched in multiple locations, introducing branch-on-branch architecture.

On the other hand, branching by functional end groups occurs with less randomness. Most commercial linear PLA chains end with one hydroxyl group and one carboxylic acid group. In the melt state, multifunctional epoxides can preferentially react with the carboxyl end group and lead to a branched structure. The most widely used multifunctional epoxide is Joncryl® (Figure 2-2), a styrene-glycidyl acrylate oligomer[75 - 78]. PLA branched with Joncryl has a comb-like chain structure and has shown improved performance in extrusion foaming and film blowing processes. Triglycidyl isocyanurate (TGIC) was also used but did not give enough branching by itself. LCB PLA was obtained only after blending with both pyromellitic dianhydride (PMDA) and TGIC[79]. PMDA can convert some of the PLA hydroxyl end groups to carboxyl groups via ring-opening of the anhydride. In a similar way, Liu et. al reacted linear PLA with 1,4-phenylene-bis-oxazoline (PBOZ) in the presence of PMDA and obtained long chain branched PLA [80]. A drawback of both epoxides and oxazolines is their slow reaction kinetics. The branching reaction may take more than 30 min to complete[79, 81, 82] while residence time in typical melt processing equipment is $\leq$ 5 min. In this work, we strive to use a faster functional group reaction to prepare long chain branched PLA. Linear PLA was reacted with trimethylolpropane tris(2-methyl-1-aziridinepropionate) (TTMAP) in the melt to produce 3-armed or chain-extended PLA in a rapid manner, see Figure 2-3. Furthermore, LCB PLA was obtained by sequentially blending with PMDA and TTMAP. We will

show that the branching architecture of final product is dependent on the order of adding PMDA and TTMAP. Finally, rheological behavior of the resulting branched PLAs will be discussed and compared to other branched PLAs prepared by free radical and epoxy functional oligomer methods.

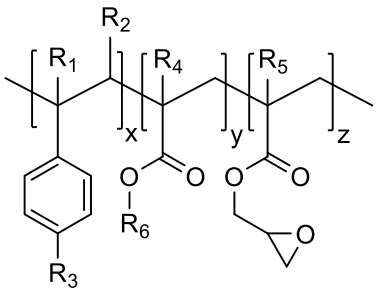

Figure 2-2 General structure of the oligomeric Joncryl® chain extenders. R1–R5 are H, CH3, a higher alkyl group, or combinations of them; R6 is an alkyl group, and x, y and z are each between 1 and 20. [83]

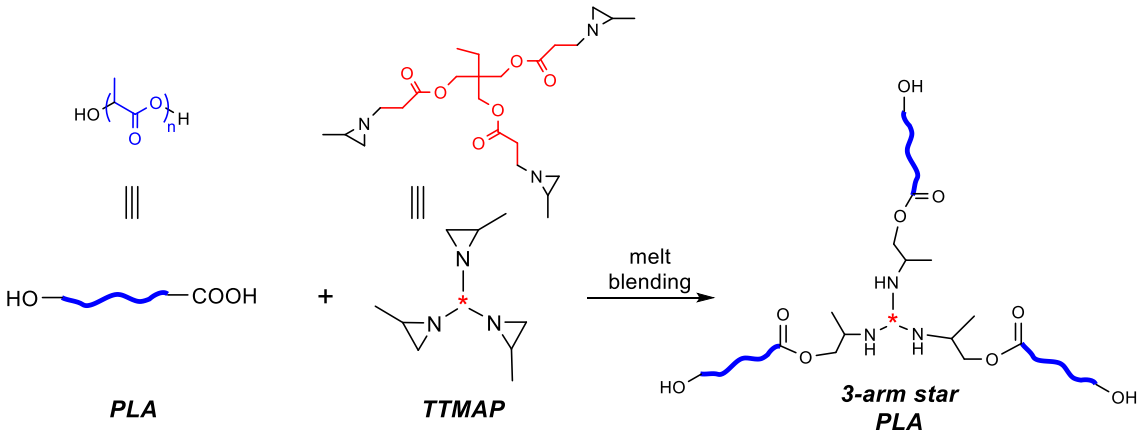

Figure 2-3 Reaction of PLA with the trifunctional aziridine, TTMAP, at equal stoichiometry.

2.2 Experimental

2.2.1 Materials

Semicrystalline PLA was obtained from Natureworks (PLA, Ingeo™ Biopolymer 2003D). Trimethylolpropane tris(2-methyl-1-aziridinepropionate) (TTMAP, 95% purity) was obtained from PolyAziridine LLC and used as received. Pyromellitic dianhydride (PMDA) and triglycidyl isocyanurate (TGIC) were obtained from Sigma-Aldrich and used as received. The styrene-glycidyl

acrylate (SGA, Joncryl® ADR4368) was provided by BASF Corporation. According to BASF product data sheet, M_w is 6800 g/mol and epoxy equivalent weight 285 g/mol. M_n was reported to be 2000 g/mol[83, 84]. See Table 2-1 for molecular weight measured in this study. The average functionality was calculated to be 7 epoxide/chain.

2.2.2 Sample preparation and gel detection

PLA pellets were dried at 40 °C for at least 12 h under vacuum before melt processing. In a typical branching reaction, 40 g PLA was introduced into a Thermo-Haake internal batch mixer (50 mL capacity) equipped with roller blades set at 170 °C and 50 rpm. For star-shaped branching, TTMAP was directly injected into the mixer after PLA pellets melted (T series samples in Table 2-1). For long chain branching, PMDA powder was first added into the melt and after 1 min, TTMAP was injected (PT series samples). In some cases, TTMAP was first blended with PLA for 2 min then PMDA was added (TP series samples). To improve the dispersion, in some other cases TTMAP was diluted 5× by volume acetone before mixing (PT-S series samples). Mixer torque and temperature were recorded. For branched samples, mixing was stopped when the torque reached a plateau. The polymer was then removed from the mixing chamber and quenched in liquid nitrogen. TTMAP concentration was varied, but PMDA concentration was kept constant to keep an equimolar ratio of PLA to anhydride groups. The formulations are listed in Table 2-1.

To detect gelation, PLA samples were dissolved in 20 mL chloroform to make 0.05 g/mL solutions, which were subsequently filtered (Fisherbrand™ Grade P8 filter paper, 1 μm pore size). Most samples completely passed through the filter paper within 3 minutes, while for others only a few drops of liquid (0.1-0.2 mL) went through within >2 hours. Samples that did not pass through the filter paper were regarded as having gelled during the branching reaction.

Table 2-1 Formulation and molecular weight of reactively processed PLA.

Sample code	PMDA (wt. %)	TTMAP (wt. %)	r [e]	M_n (kg/mol) [f]	M_w (kg/mol) [f]	PDI [f]
L[a]	-	-	-	75	150	2.0
L'[a]	-	-	-	59	119	2.0
P	0.16	-	-	68	131	1.9
T1	-	0.1	0.48	95	188	2.0
T2	-	0.25	1.20	109	213	2.0
T3	-	0.5	2.41	92	173	1.9
PT1	0.16	0.1	0.48	79	218	2.8
PT2	0.16	0.25	1.20	gel	-	-
PT3	0.16	0.5	2.41	gel	-	-
TP0 [b]	0.16	0.06	0.28	73	170	2.3
TP1 [b]	0.16	0.1	0.48	82	196	2.4
TP2 [b]	0.16	0.25	1.20	gel	-	-
TP3 [b]	0.16	0.5	2.41	gel	-	-
PT1-S [c]	0.16	0.1	0.48	77	193	2.5
PT2-S [c]	0.16	0.25	1.20	gel	-	-
J[d]	-	-	-	88	261	3.0
0.15 wt.% TGIC 7 min mixing	-	-	-	61	129	2.1
PMDA 2 min mixing	0.16	-	-	73	141	1.9
PMDA 7 min mixing	0.16	-	-	68	131	1.9
PMDA 15 min mixing	0.16	-	-	64	128	2.0
Pure Joncryl ADR4368	-	-	-	3.6	6.4	1.8

[a] L PLA pellets as received from manufacturer; L' PLA mixed for 15 min in the mixer at 180 °C. [b]PMDA was introduced into blend after TTMAP. [c] TTMAP was dissolved in 5× acetone. [d] Sample J was blended with 0.5 wt% SGA for 12 min. [e] r is molar ratio of aziridine group to PLA. [f] The molecular weights were calculated based on universal calibration using K_{PS}=8.63 mL/kg, K_{PLA}=17.4 mL/kg, and $\alpha_{PS}=\alpha_{PLA}=0.736$.[85, 86] The typical uncertainty of molecular weight measurement in term of standard deviation of 3 runs was ± 4.8 kg/mol.

2.2.3 Molecular Characterization

Molecular weight of PLA samples was characterized by gel permeation chromatography (GPC) with THF as carrier solvent at room temperature using a Thermo Separation Products Spectra Systems equipped with three 5 mm Phenomenex Phenogel columns, a Waters 515 pump, and a Waters 2410 differential refractive index detector. Calculation of molecular weight was carried out by universal calibration relative to 10 polystyrene standards (580−377,400 g/mol, Polymer Laboratories). Relative hydroxyl end group concentration of PLA samples was determined

using ^{1}H nuclear magnetic resonance (^{1}H NMR) spectroscopy. The samples were dissolved in deuterated chloroform ($CDCl_3$), measured with a Bruker Avance 500 spectrometer, and reference to TMS at 0.00 ppm. The end group concentration was estimated by integration of the end group methine proton -CH(CH_3)OH at ca. 4.35 ppm vs. the methane in the repeat unit -C*H*CH_3-O(C=O)- at ca. 5.17 ppm.

2.2.4 Small Amplitude Oscillatory Shear (SAOS)

The linear viscoelastic properties were measured via SAOS on an ARES rheometer (TA Instruments) at 180 °C, using 25 mm parallel plates. Strain sweep tests were conducted on all materials at a frequency of 1 rad/s to determine the critical strain where materials start non-linear behavior, which was approximately 20% strain for all investigated materials. Frequency sweeps over a range of 100 – 0.03 rad/s were then conducted using strains below the measured critical strain. The stability of PLAs was determined by dynamic time sweep tests at a frequency of 1 rad/s and 1% strain.

2.2.5 Extensional Viscosity

Extensional viscosity of the PLA materials was measured on an ARES-G2 rheometer using the extensional viscosity fixture (EVF, TA Instruments). Rectangular samples with dimensions 25×5×1 mm were prepared via compression molding (Carver, Inc., Wabash, Indiana) at 180 °C and 2 tons of force. The sample was annealed on the EVF fixture in the ARES forced convection oven at 180 °C for 20 seconds to allow the temperature to equilibrate. The sample was then stretched at strain rates between 0.1 and 10 s^{-1} to a total Hencky strain of 5.

To compare the extensional response to the linear viscoelastic limit, the PLAs, except sample J, were tested in start-up of steady shear at a shear rate of 0.1 s^{-1} on ARES-G2 rheometer using a 25 mm cone and plate with an angle of 0.04. To minimize degradation, start-up of steady shear for sample J was carried out using 25 mm parallel plates. The measured shear viscosity from

these tests was multiplied by 3, based on Trouton's ratio of linear polymers, to predict the linear viscoelastic limit of the materials under extensional flow.

2.3 Results and Discussion

2.3.1 Reactivity

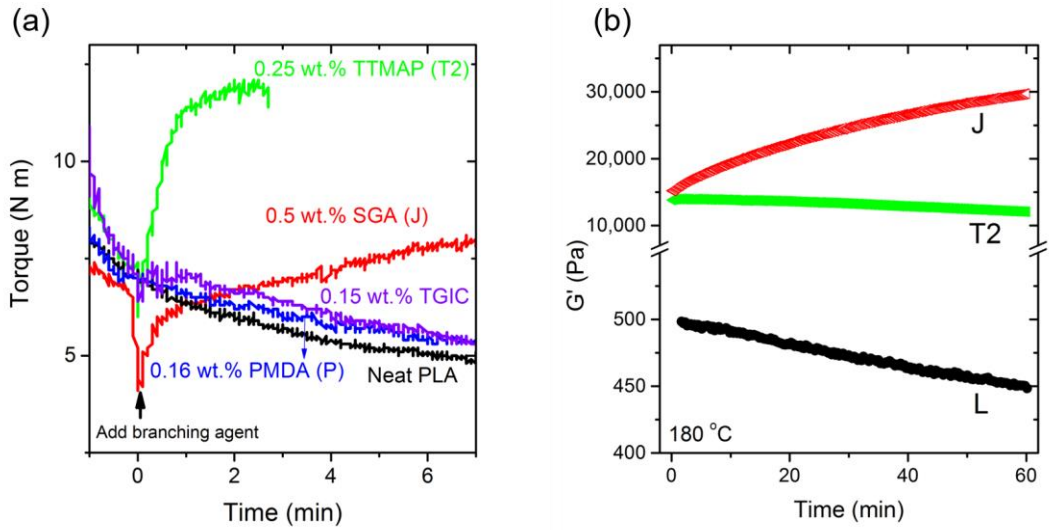

Figure 2-4 Reactivity and stability of PLA with different branching agents. (a) Representative torque profiles during reactive processing for sample T2, J, P, neat PLA and PLA blended with TGIC. None of those samples contains antioxidant. Time scale was shifted to make the moment of adding branching agent time zero. (b) SAOS time sweep at 1 rad/s of sample L, T2, and J. Sample loading took ~ 15 min at 180 °C. G' of linear PLA decreased ~10% in one hour due to degradation.

Aziridine groups are known to react with carboxylic acids to afford their corresponding amino esters (Figure 2-3) even at room temperature without catalyst[87]. However, reactions between epoxides and carboxylic acids require elevated temperatures (typically >100 °C) presumably due to lack of basicity relative to their aziridine counterparts[88, 89]. Even at 180 °C, a common processing temperature for PLA, the reaction rate is low, but certain catalysts can increase this rate[82]. The difference in the reaction rates for aziridine compared to epoxides was confirmed using mixer torque. Figure 2-4 shows torque evolution for the PLA reaction with approximately equal molar

functional groups of TTMAP, TGIC, PMDA and SGA. The temperature in the mixer increased slowly due to shear heating but stayed below 190 °C. Mixing torque is proportional to the viscosity of the PLA melt, which depends on molecular weight and temperature. The torque of neat PLA decreased monotonically because of the temperature increase and thermal degradation. When PLA was blended with TGIC, the torque decreased similarly to neat PLA. If the reaction went to completion, TGIC should triple the molecule weight and mixing torque should increase. Hence, we can conclude the TGIC branching reaction was too slow to compensate for the degradation and temperature increase. It has been reported that melt blending with TGIC can significantly increase the molecular weight of PET [90, 91], a polyester that also goes through chain scission in melt state. This is contradictory to what was found with PLA; however, the processing temperature for PET is much higher than PLA (typically > 260 °C), which speeds up the epoxide-carboxylic acid reaction. Apparently, the branching reaction in the PET melt and can override degradation and increase the viscosity. The results with PMDA will be discussed later.

As shown in Figure 2-4, completely different trends were observed for TTMAP and SGA. Upon addition of TTMAP, the torque had a sharp drop due to lubrication, then it increased in a spike-like manner and reached maximum within 2 minutes. This very fast reaction at 180 °C is reasonable considering the high reactivity of aziridine with carboxylic acid at room temperature. SGA blending showed a much slower torque increase. The torque was still increasing after 10 minutes of blending despite a temperature increase and possible PLA chain scission. Dynamic time sweep in Figure 2-4b revealed that a reaction in sample J was still occurring after sitting in the rheometer at 180 °C for 1 hour. This demonstrates that the multifunctional aziridine branching reaction is much faster than the multifunctional epoxides and more suitable for extrusion processes where residence time is short.

2.3.2 Star-shaped branching with TTMAP

Because the reaction between linear PLA and TTMAP can come to completion quickly, the key factor that determines molecular weight of the final product is the stoichiometric ratio of the aziridine group to the carboxylic acid, defined as $r = \frac{[AZ]}{[COOH]} = [AZ]/[PLA]$, where $[AZ]$ and $[COOH]$ are concentrations of aziridine group and carboxylic acid end group. NMR end group analysis revealed that the number-average molecular weight (M_n) of the starting linear PLA is 70-75 kg/mol, in reasonable agreement with M_n by GPC shown in Table 2-1. To keep the carboxylic acid concentration in slight excess to the aziridine, 75 kg/mol was used to estimate $[COOH]$ in the PLA melt. $[AZ]$ was calculated based on TTMAP weight fraction and the assumption that all TTMAP molecules have an aziridine functionality of 3.

The effect of the stoichiometric ratio on the molecular weight was first studied. Figure 2-5a shows representative GPC traces of linear and branched PLA. Table 2-1 gives M_n and polydispersity. Sample L', which was blended in the mixer for 15 min at 180 ºC, showed lower molecular weight than L, the PLA as received, due to degradation. For r = 1.2 (T2) and r = 2.4 (T3) samples shifted to higher molecular weight. Polydispersities of all samples remained the same. Assuming a complete reaction M_n as a function of r can be calculated:

$$M_n = \begin{cases} \frac{3}{3-2r} M_0 & (0 < r \leq 1) \\ \frac{3r^2}{3r^2-3r+1} M_0 & (1 < r < 3) \end{cases} \quad (2\text{-}1)$$

where M_0 is the number average molecular weight of the starting linear PLA. For 0 < r < 1, the final product should be a mixture of linear chains and 3-arm stars while for 1 < r < 3 the final product should be a mixture of linear chains, 2-arm chains and 3-arm stars. Figure 2-5b compares M_n from GPC and Equation 2-1. The experimental values are lower than theory but do show a maximum M_n around r = 1. There are several possible causes for the discrepancy. First, small changes in r can make big differences in M_n. There was ~7% error in r calculation due to the uncertainty in molecular

weight measurement. Secondly, GPC used in this study underestimates the molecular weight of 3-arm stars since star polymers have a smaller hydrodynamic volume compared to linear chains of the same molecular weight[92]. Thirdly, Equation 2-1 doesn't account for PLA degradation during melt processing. Lastly, the aziridine functionality of TTMAP may be less than three due to the reversibility of the aza-Michael addition of the aziridine[93].

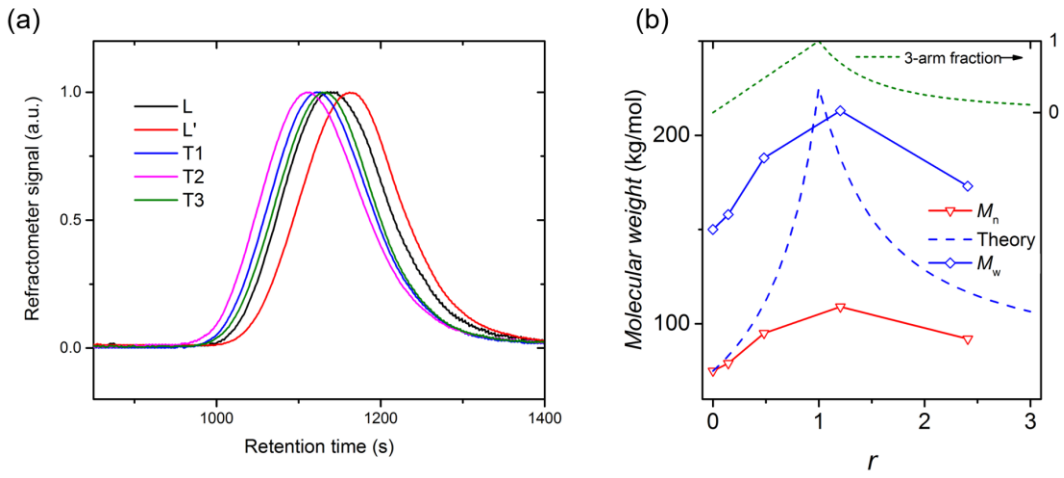

Figure 2-5 Molecular weight of TTMAP-branched PLA. (a) Representative GPC traces of linear and branched PLA (IR signal is normalized by highest signal level of each trace). (b) M_n, M_w and theoretical weight fraction of 3-arm PLA as a function of *r*, stoichiometric ratio.

Figure 2-6 shows the linear viscoelastic properties of TTMAP branched PLA as well as the linear PLA (sample L). The branched PLAs have higher viscosity and more pronounced shear thinning behavior than linear PLA. In the high frequency region, the viscosity of star-branched PLA is close to that of linear PLA. This behavior was also found in LCB PLA produced by free radical branching[74]. Similar to molecular weight, the viscosity around $r = 1$ (sample T2) is highest because it contains more 3-arm stars. In Figure 2-6b, at high frequency G' of branched PLAs converge towards linear PLA (L) whose plateau modulus is 10^6 Pa [94, 95]. Sample L enters terminal scaling, $G' \propto \omega^2$, quickly after the plateau. But the branched PLAs show a much broader transition to terminal region and a longer terminal relaxation time. In sample T3, which has the least amount

of 3-arm stars, terminal relaxation starts earlier than T1 and T2, around 10^{-1} s^{-1}. Although branched PLAs in this work are polydisperse, their linear viscoelastic behavior described above is consistent with model monodispersed 3-arm star polyisoprene [96, 97]. The van Gurp-Palmen plot, which plots phase angle δ versus complex modulus |G*|, is sensitive to polydispersity and long chain branching [98 - 100]. As shown in Figure 2-6c, van Gurp-Palmen curves of branched PLAs deviate from linear PLA and the deviation becomes more evident as the amount of 3-arm species increases. Since the branched samples have similar molecular weight distribution (Table 2-1, Figure 2-5a) as linear PLA, deviation in Figure 2-6c is mainly a result of the branched topology.

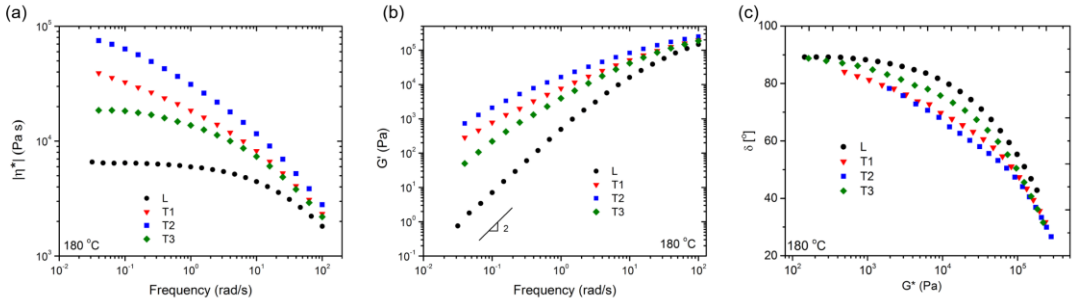

Figure 2-6 Rheological properties of TTMAP-branched PLA. (a) Complex viscosity and (b) storage modulus as a function of angular frequency, (c) van Gurp-Palmen plot for linear and star-branched PLA.

It is well documented in the literature that transient extensional viscosity at constant strain rate responds sensitively to branched chain structure[56, 74, 79, 100]. Specifically, branched polymers show strain hardening, an increase in extensional viscosity beyond a certain strain. Figure 2-7 shows the transient extensional viscosity of sample L, T1, and T2, together with the linear viscoelastic (LVE) limit of their transient responses under extension measured by start-up of steady shear, $3\eta^{+}(t)$. The extensional viscosity of T1 and T2 is higher compared to L, and it takes longer time for the shear viscosity to achieve steady state due to longer terminal relaxation time. But just like linear PLA, the star-branched PLAs follow the LVE limit over a strain rate range of 0.1 s^{-1} to

10 s^{-1}. Similar behavior was also found in symmetric 3-arm star polyethylene, which has entangled branches[101].

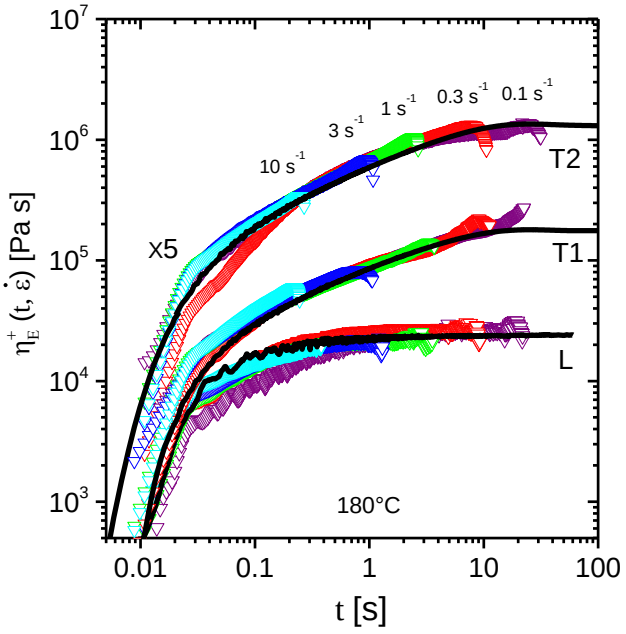

Figure 2-7 Transient extensional viscosity as a function of step time at different strain rates for linear PLA, L, together with star-branched PLAs, T1 and T2. The black lines are LVE limits measured by startup of steady shear. Viscosity of T2 was shifted vertically by 5×.

2.3.3 Long chain branching with PMDA and TTMAP

2.3.3.1 Carboxylation

It has been shown that multiple long chain branches along the polymer backbone are needed for a polymer to demonstrate strain hardening behavior[100, 102, 103]. In order to achieve a LCB structure, PMDA was blended with PLA to convert the hydroxyl end group into a carboxyl group, as shown in Figure 2-8. Literature reported very mild coupling between anhydride and hydroxyl group when they were used for polymer blend compatibilization in the melt state[104 - 106]. This low reactivity was affirmed in the present study. As shown in Figure 2-4, the torque kept decreasing after PLA was blended with PMDA. The three possible products after reaction are shown in Figure

2-8. If the reaction were as rapid as TTMAP, the torque should have increased because the formation of species 3 would increase the overall molecular weight.

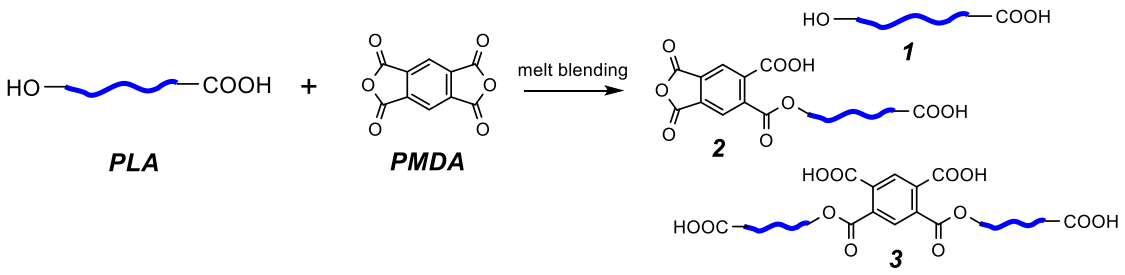

Figure 2-8 Carboxylation reaction with PMDA.

Assuming that the anhydride group in species 2 has the same reactivity as PMDA, the average carboxylic acid group functionality per polymer chain can be calculated as follows based on the anhydride group conversion, p_{ah},[107]:

$$f_e = \frac{1+3p_{ah}+4p_{ah}^2}{1+p_{ah}} \quad (2\text{-}2)$$

p_{ah} will be estimated in the following section.

2.3.3.2 Multiple long chain branching

Due to the presence of multi-carboxyl species 2 and 3, further reaction of PLA with the trifunctional TTMAP is like an $A_n + B_3$ crosslinking reaction, with $1 < n = f_e < 4$. LCB structure can be generated if the reaction is below gel point. PMDA modified PLA was blended with different amounts of TTMAP to repeat the branching reaction in Section 2.3.2. The formulations are listed in Table 2-1, sample PT1, PT2, and PT3. As shown in Figure 2-9c, there was no change in mixing torque after addition of PMDA, but a substantial increase occurred after the addition of TTMAP. Crosslinked PLA was detected in PT2 and PT3. Figure 2-9a shows the GPC trace of sample PT1. Unlike the 3 arm stars, PT1 showed a secondary peak at a shorter retention time. The distorted peak shape indicates a higher molecular weight portion, which must be the LCB chains.

Alternatively, LCB structure can also be generated by melt blending PMDA with T1, T2 and T3. Figure 2-9(b) shows the mixing torque of sample TP1, TP2 and TP3. There is no evident change in torque upon addition of PMDA into T1 because the aziridine group in T1 was depleted. In contrast, sample TP3 showed a second sharp increase in torque. This was likely caused by the reaction of residual aziridine in T3 with the newly formed carboxyl group, which led to gelation, indicated by the increased noise level seen in the torque profile.

In an $A_f + B_g$ reaction, gel point occurs when the following equation is fulfilled,[107]

$$p_A p_B = \frac{1}{(f_e-1)(g_e-1)} \tag{2-3}$$

where p_A is the conversion of A type group, p_B is the conversion of B type group, f_e is the average functionality of the A_f molecules, and g_e is the average functionality of the B_g molecules. In the case of branching after carboxylation, A is the carboxylic acid group and B the aziridine group, so f_e is given by Equation 2-2 and $g_e = 3$. To further simplify the problem, we can focus on sample PT1 where aziridine groups are completely converted due to excess carboxylic acid groups. Then conversions of A and B are given by: $p_A = 1$, $p_B = r'p_A = rp_A/(1+p_{ah})$ and $r = 0.48$ for sample PT1. Combining Equation 2-2 and 3, gelation of PT1 requires $p_{ah} \geq 0.62$. The fact that PT1 is not crosslinked supports a value of p_{ah} well below 0.62. The above analysis requires two more assumptions. First, chain scission during mixing is negligible. Second, TTMAP is uniformly dispersed in PLA melt. This is most likely not fulfilled because it is difficult to mix the low viscosity TTMAP into molten PLA uniformly before the fast reaction begins. TTMAP localization could cause formation of gel particles, which is supported by sample PT2-S in the following discussion.

The linear viscoelastic properties of some LCB PLA samples are shown in Figure 2-10. Sample PT1 and PT2 behaved similarly to the star-branched T1 and T2 in SAOS, but sample PT3 is quite different from T3. Compared with linear PLA, it has lower viscosity and lower elasticity at high frequency. This can be explained by gelation of PT3 during mixing. Mechanical mixing was

intense enough to break the crosslinked PLA into small gel particles. The final product is more like gel particles suspended in non-crosslinked PLA chains. The broken gel portion does not contribute significantly in linear viscoelastic regime (SAOS) but can be significant at large deformations. PT2 is less crosslinked than PT3 thus it still has higher viscosity and elasticity than linear PLA.

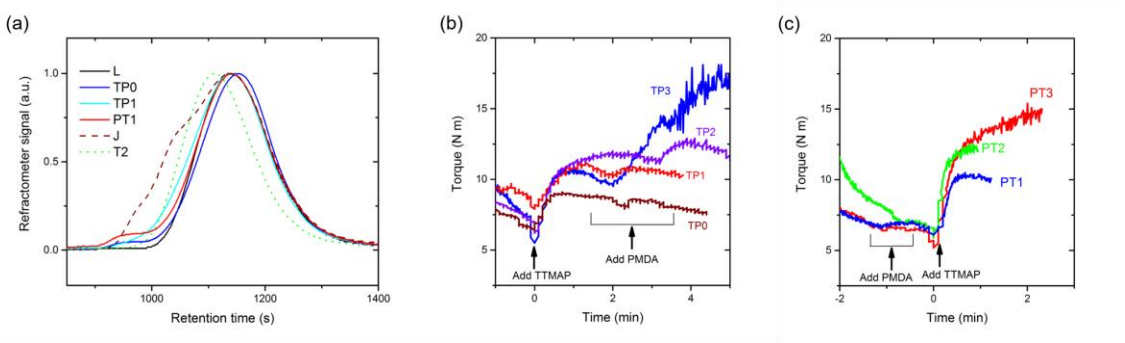

Figure 2-9 Molecular weight and mixing torque of PLAs branched with both PMDA and TTMAP. (a) Representative GPC traces of linear and LCB PLA. (b) Representative torque profiles of samples TP0, TP1, TP2 and TP3. Time scale is shifted to make the moment of adding TTMAP time zero. (c) Representative torque profiles of samples PT1, PT2 and PT3.

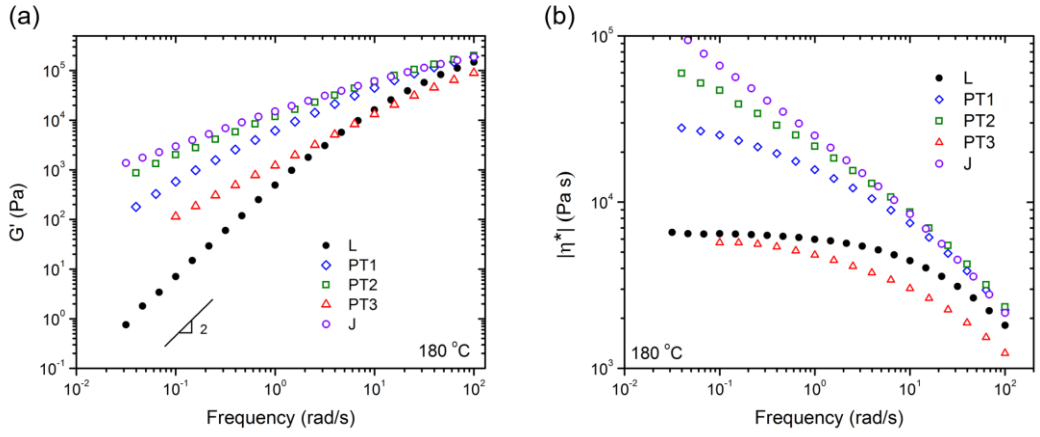

Figure 2-10 Storage modulus and complex viscosity as a function of angular frequency for LCB PLA.

2.3.3.3 Extensional viscosity

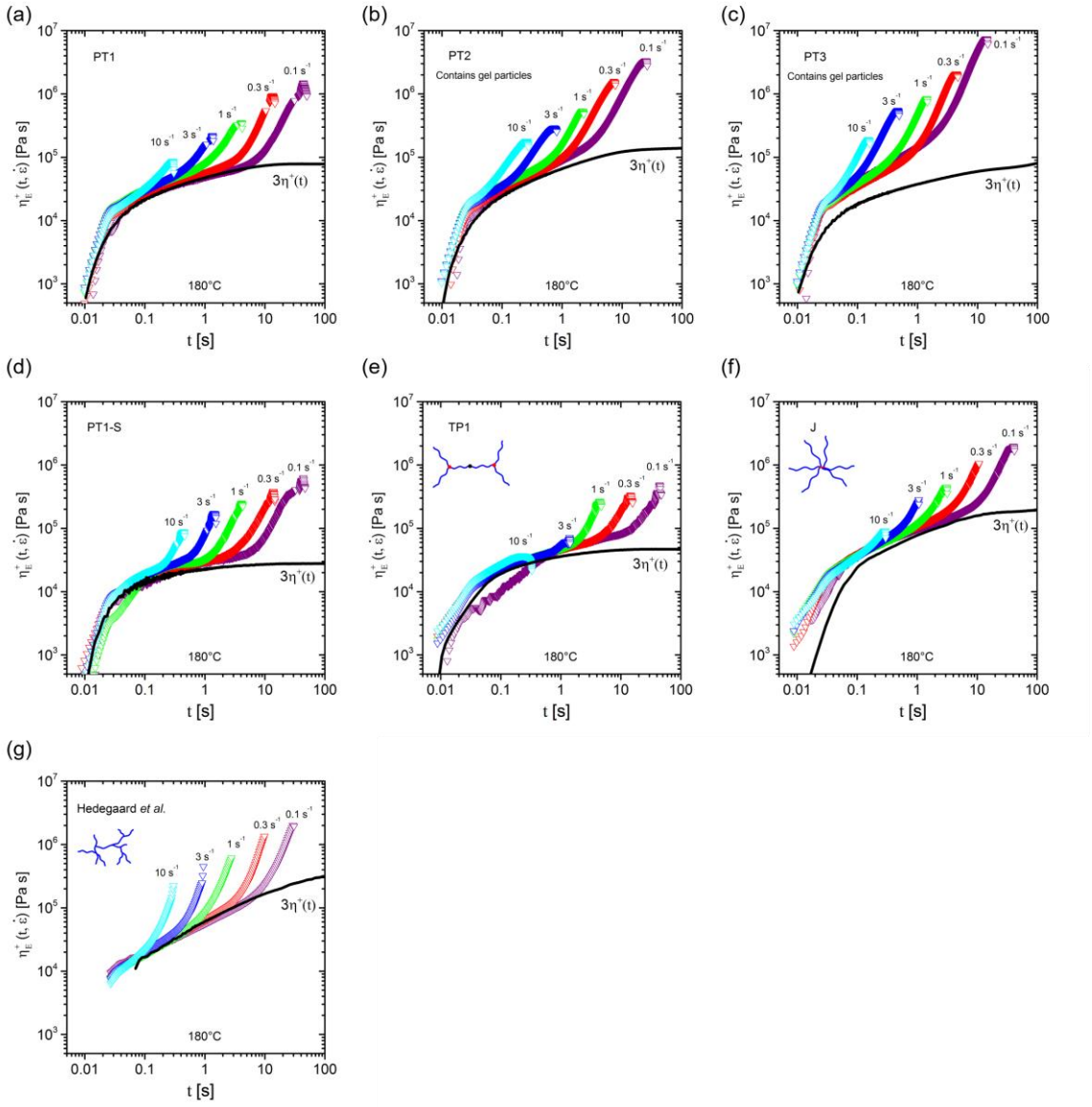

Figure 2-11Transient extensional viscosity as a function of step time at different strain rates for different LCB PLAs. (a) PT1, (b) PT2, (c) PT3, (d) PT1-S, (e) TP1, (f) J, (g) Free radical branched PLA by Hedegaard et al.[74].

Figure 2-11 shows the transient extensional viscosity of LCB PLA at different strain rates. Though PT1 and PT2 behave like star shaped T1 and T2 in SAOS, they show strain hardening in extension. The strain hardening in PT3 is strongest among all the samples while its complex shear

viscosity in SAOS is lowest. Considering the nonlinear nature of extensional rheology, it can be envisioned that the gel particles in PT3 are contributing to extensional viscosity through particle stretching. This is further supported by its abnormal behavior in start-up shear. In samples without gel (PT1, PT1-S, TP1), the LVE response $3\eta^{+}(t)$ corresponds well with the extensional viscosity before the critical strain where strain hardening begins. However, in PT3, $3\eta^{+}(t)$ is much lower than the extensional viscosity, regardless of strain, and doesn't reach a plateau like others within a shear strain of 10. We postulate that the gel particles are less responsive to shear due to particle rotation.

Crosslinked PLA parts have a more evident effect on the failure behavior of PLA in uniaxial extensional flow. Figure 2-13a shows the maximum Hencky strain achieved before sample failure, $\varepsilon_{H,max}$. Experimentally we designate $\varepsilon_{H,max}$ as the strain where extensional viscosity smoothly reaches a maximum. Sample PT1 stretched to $\varepsilon_{H,max}$ >4 without failure at high strain rates. In contrast for samples PT2 and PT3, $\varepsilon_{H,max}$ decreases with the increase in crosslinked particles, which act as inhomogeneities. On the other hand, diluting TTMAP in solvent improved $\varepsilon_{H,max}$ as seen in sample PT2-S because the better dispersion of TTMAP suppressed gel formation.

A comparison between PT1 and TP1 shows the effect of mixing sequence of PMDA and TTMAP. TP1 has less strain hardening than PT1 at all strain rates studied, and the absolute value of extensional viscosity is also lower. At low strain rates, TP1 starts strain hardening at a larger strain than PT1 and the hardening almost disappeared at high strain rates (Figure 2-11e). From the standpoint of functional group reactions, the newly formed carboxylic acid in the carboxylation step of sample TP1 would not participate in branching. Therefore, it is reasonable that there is less branching in TP1 than PT1, consequently less strain hardening and lower viscosity. The fact that TP1 shows strain hardening confirms the presence of species 3 in Figure 2-8 after PLA reacts with PMDA, otherwise there would be no molecules with more than 1 branch and no strain hardening. Thus, an H-shaped branching structure (Figure 2-12) is the basic building block for any branched

chains that can lead to extension hardening in TP1.

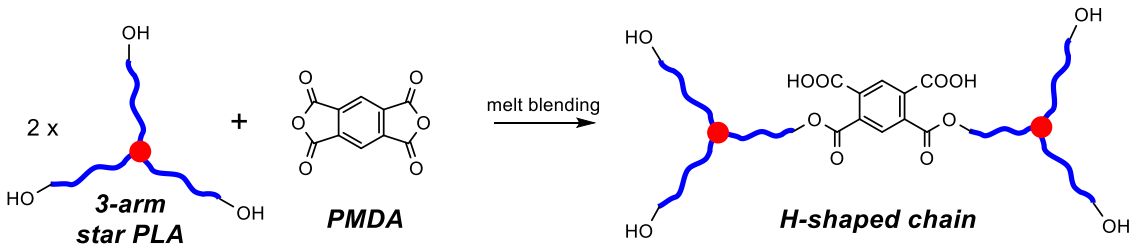

Figure 2-12 Possible topology of the extensional hardening chains in TP1.

The strain hardening factor, X_E, is usually used as a quantitative measure of the degree of strain hardening,

$$X_E = \frac{\eta_E^+(t,\dot{\varepsilon})}{3\eta^+(t,\dot{\gamma},)} \quad when\ \dot{\varepsilon} = \dot{\gamma}$$

For fluids that show no strain hardening, $X_E = 1$. X_E of the PLA samples are presented in Figure 2-13b. All the samples branched with PMDA and TTMAP show a decreasing strain hardening factor with increasing strain rate. This is in opposition to the behavior of classical highly branched LDPE and PP melts, for which the strain hardening becomes more significant at higher strain rates[56, 108]. Decreasing X_E with strain rate has been observed in polypropylene irradiated with low dose electron beam or γ-rays[109] and also metallocene-catalyzed polyethylene[110]. This behavior was attributed to very low amount of branching combined with high molecular weight branches. Sample PT1, PT1-S and TP1 fall into this category. First, the branches are very long because each of them is an entire original linear PLA chain, M_w = 160 kg/mol, nearly 20 times the entanglement molecular weight. Second, due to the tri-functionality of TTMAP, at least two linear chains are needed to generate one branch, so there would not be many branches before the branched molecules gel. The topology of branched chains here is closer to H-shaped structure with sparse branches, rather than a highly branched treelike structure. Third, GPC traces indicate that there is a considerable amount of linear and 3-arm chains in the samples. Stange et. al observed decrease of X_E with strain rate in blends of

linear and LCB polypropylene[108]. Their conclusion can be applied here: long chain branched chains have a stronger effect on long relaxation times, i.e. low strain rates, whereas the non-strain-hardening PLA chains dominate at high strain rates. For sample PT2 and PT3, the effect of crosslinked PLA particles should be taken into account besides what is discussed above. Elastic deformation of crosslinked particles is only strain dependent; therefore it contributes less to extensional viscosity at high strain rates, resulting in less strain hardening. Similar phenomena was observed in blends of linear and crosslinked HDPE in which only 3 wt.% was crosslinked[111].

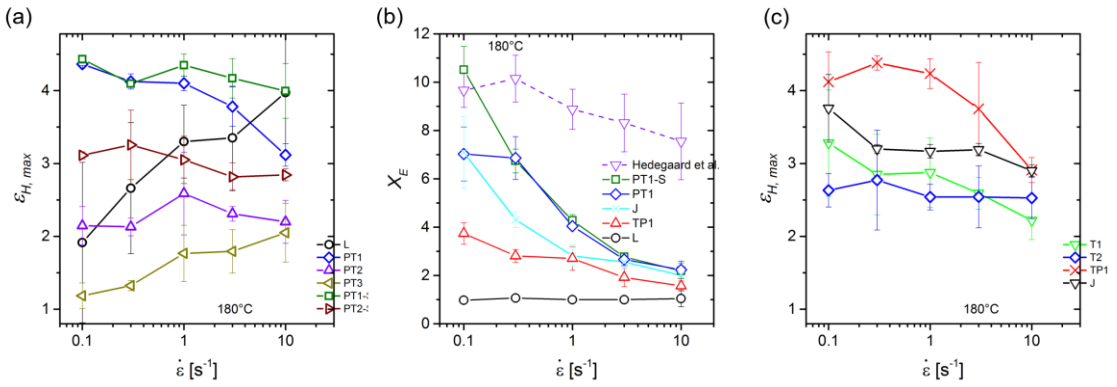

Figure 2-13 Hencky strain at sample failure and strain hardening coefficient (X_E) for linear and LCB PLA. For samples broken before $\varepsilon_H = 2.7$, X_E was calculated at $\varepsilon_{H,max}$.

2.3.3.4 Comparison to other PLA branching strategies

To compare our results with current industrial practice, it is worth discussing the rheology of sample J. In Figure 2-11f, the strain hardening in sample J becomes less pronounced as strain rate increases, consequently, X_E decreased with increasing strain rate (Figure 2-13b). GPC trace in Figure 2-10a indicates sample J is also a mixture of branched chains and linear chains, and the amount of branched chains is higher than sample PT1. However, sample J has slightly lower X_E than PT1. This is related to their branched structures. SGA is a linear multifunctional epoxide oligomer with molecular weight of 2k while the linear PLA used in this study is 75k, over ten times the molecular weight of SGA. Though PLA and SGA have different statistical segment length and

monomer molecular weight, this will not affect the chain length ratio much. The resulting topology of J is like a "comb-star" (Figure 2-15), with a very short backbone and long arms. Strain hardening of branched polymers comes from the stretching of the chain segments contained between two branching points[103] and is stronger with longer chain segments[112]. We postulate that the weaker strain hardening of sample J compared to PT1 has its origin in shorter chain segment length between branch points. Though J may have a larger number of branches if all the epoxide groups reacted, not all the branches are effective for strain hardening because the segments between two neighboring branches are only ~3 repeat units. Moreover, sample PT1 has lower shear viscosity and viscoelastic moduli than J in Figure 2-10, yet similar extensional viscosity at large strain in Figure 2-14. Note that, like the gelled sample PT3, the shear viscosity, $3\eta^{+}(t)$, of J does not reach steady state up to strain 10 (compare Figures 7c and 7f). This shines some light on how to design a polymer with low shear viscosity, which reduces pressure drop in extrusion, combined with strong extensional hardening.

It is valuable to also compare our results to the free radically-branched PLA in reference 74 by Hedegaard et al. (also Chapter 6). As mentioned in the background, PLA branched by free radical process may have branch-on branch structure. The extensional viscosity of this PLA is presented in Figure 2-11g and X_E in Figure 2-13b. In contrast to the sharp decrease of X_E with strain rate of sample PT1 and J, its X_E remained roughly constant and the strain hardening at 10 s^{-1} is still strong, which may be due to a large number of branches and sufficiently long chain segments between branch points. However, it is again worth noting that the shear viscosity is much higher than PT1 or PT2.

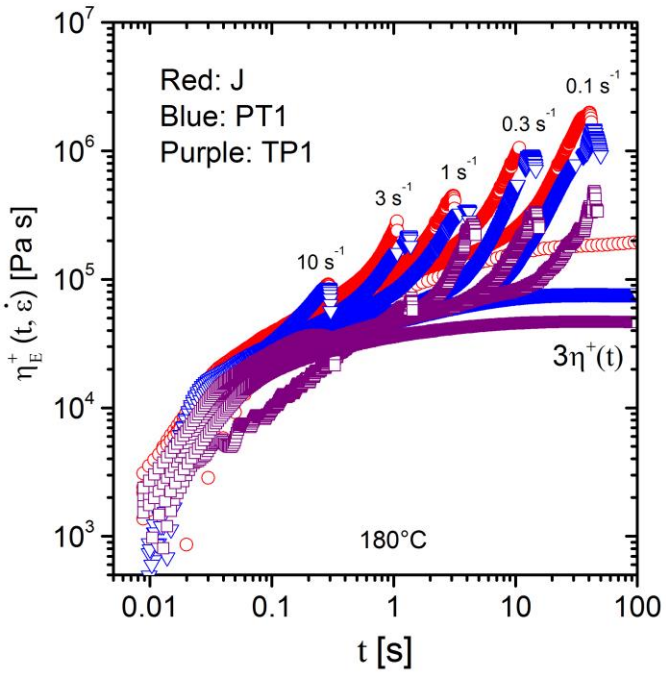

Figure 2-14 Directly comparing the viscosity of sample J, PT1 and TP1.

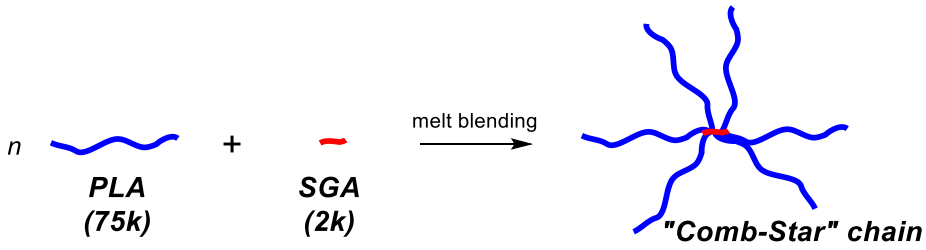

Figure 2-15 "Comb-Star" topology of PLA branched with SGA. The backbone is much shorter than the branches.

2.4 Conclusions

A strategy using highly reactive trifunctional aziridine was developed to branch PLA via simple melt processing. Melt blending linear PLA with TTMAP resulted in 3-arm star-shaped PLA, which exhibits higher viscosity but no strain hardening in extensional flow. Long chain branched PLA was formed via sequential reactions of PMDA followed by TTMAP with PLA. Some of the

hydroxyl end groups on PLA chains were converted into carboxyl groups by PMDA, but, compared to TTMAP, the reaction between PMDA and PLA is mild and incomplete. Gelation occurred when excess amount of TTMAP was used. A simplified gel point calculation was conducted to estimate PMDA conversion in the carboxylation step. The LCB PLA also showed higher shear viscosity and elasticity than linear PLA. Moreover, strain hardening behavior and a decreasing strain hardening factor with increasing strain rate were observed in extensional flow. For LCB PLA without gelation, the rate dependence of strain hardening factor, together with the chain end linking nature of the functional group branching method, suggested a low branching level, i.e. H-shaped topology, with very long branches. It is found that the strain at sample break in uniaxial extension can be qualitatively used to detect gelation in a branching reaction. LCB PLA with higher amount of gel showed lower strain at break.

The strategy described here leads to lower shear viscosity with similar extensional behavior compared to current methods used to branch PLA like free radical chemistry and reacting chain ends with an epoxy functional oligomer. This study provides guidelines for designing polymers with low shear viscosity, which reduces pressure drop in extrusion, combined with strong extensional hardening, which enhances performance in processes like film blowing, sheet forming and foaming that involve melt stretching.

Chapter 3 Comb-shaped branching of PLA with aziridine-functionalized polymer*

3.1 Motivation

As introduced in Chapter 2, Joncryl®, a commercial multi-epoxide oligomer by BASF, is by far the most widely used branching agent for PLA and PLA-based polymer blends. More than half of the research articles on PLA branching adopted this strategy. In Chapter 2 we postulated that Joncryl leads to "comb-star" chains with short spacing between branch points (Figure 3-1). The extensional hardening of "comb-star" chains comes at the cost of significantly increased shear viscosity and elasticity especially at low shear rate, which adds to the processing difficulties in extrusion. Figure 3-2 shows the mixing forces of a linear PLA and a branched PLA during compounding in an Xplore microcompounder. The force for branched PLA is higher than linear PLA at low screw speed. Another drawback of Joncryl is the slow rate of epoxide–carboxylic acid reaction, which makes the resin's rheological properties not stable during melt processing (see Chapter 2).

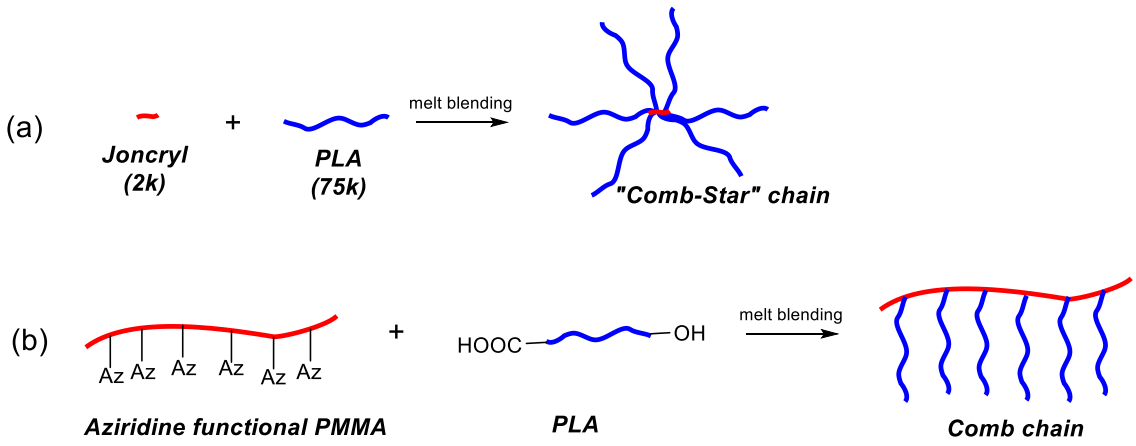

Figure 3-1 Branching PLA with commercial Joncryl and aziridine-functional PMMA.

* Portions of this work was done in collaboration with Joseph Schaefer. Financial support for this work came from the National Science Foundation through the Center for Sustainable Polymers (CHE-1413862).

Here we take advantage of the aziridine group's fast reaction with PLA to make stable branched PLA and test our postulations about the "comb-star" topology. Poly(methyl methacrylate) (PMMA) was chosen as the backbone of the new branching agent because it is miscible with PLA[113]. Copolymerization of 2-hydroxyethyl methacrylate (HEMA) with MMA allowed attachment of aziridine functional group to the PMMA backbone. Figure 3-1b shows the proposed branching reaction and Figure 3-3 shows the synthesis of aziridine functionalized PMMA.

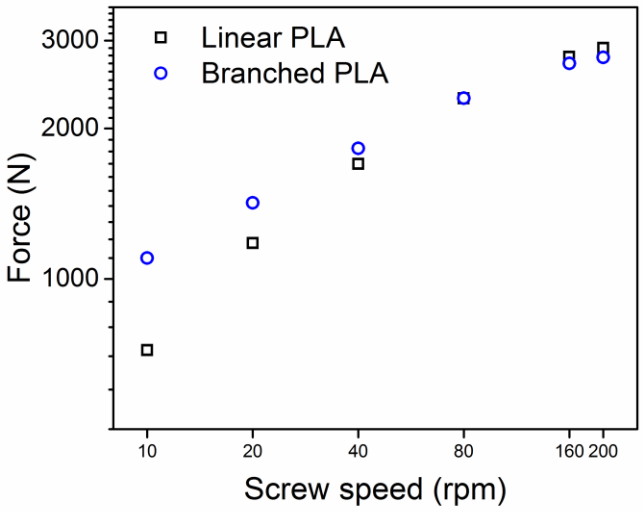

Figure 3-2 Mixing force (equivalent torque) of linear and branched PLA as a function of screw speed. Branched PLA is deTerra® IP 1406-1, see Chapter 6 for details.

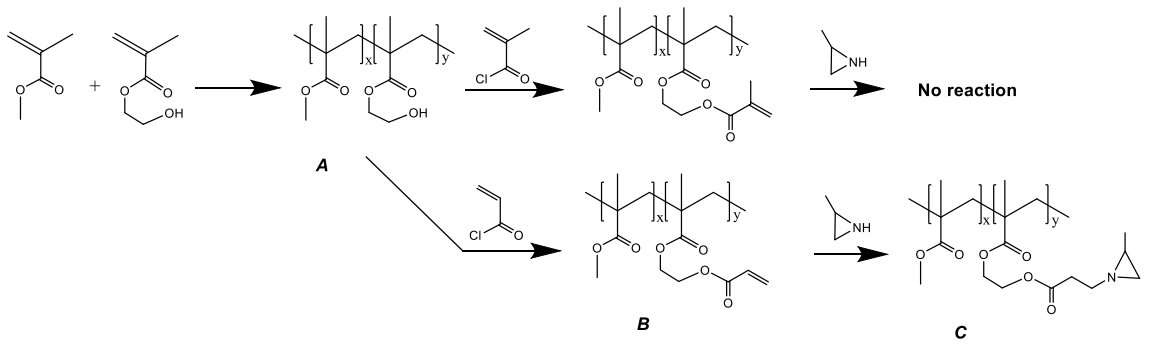

Figure 3-3 Synthetic route to aziridine-functionalized PMMA.

3.2 Experimental

As shown in Figure 3-3, an aziridine functionalized comb-type polymer was synthesized in a three-step procedure: 1) free radical polymerization, 2) nucleophilic addition/elimination of acyl chloride and alcohol, and 3) Aza-Michael Addition of an aziridine molecule.

3.2.1 Reagents

Methyl methacrylate (99%, Sigma-Aldrich) and 2-hydroxyethyl methacrylate (97%, Sigma-Aldrich) were passed through a column of activated basic alumina to remove the inhibitor. 2,2′-azobis(2-methylpropionitrile) (AIBN) (98%, Sigma-Aldrich) was recrystallized in methanol. The acryloyl chloride (Sigma-Aldrich) and 2-methylaziridine (Sigma-Aldrich) were used as obtained.

3.2.2 Synthesis

3.2.2.1 poly(MMA-co-HEMA)

A random copolymer of methyl methacrylate and 2-hydroxyethyl methacrylate was synthesized by free radical polymerization using AIBN as initiator. The reaction was carried out in 1 L toluene at a temperature of 65°C under a flow of nitrogen. All materials were added to the reaction flask before purging with nitrogen for 5 minutes at room temperature (See Table 3-1 for details). To prevent monomer drift, the reaction flask was quenched in a bath of cold water after 90 minutes to limit AIBN decay to 10%. Then the solution was concentrated using a rotational

evaporator, and methanol (10 ×) was used to precipitate and wash the polymer. The polymer was dried overnight in a fume hood before drying in a vacuum oven.

3.2.2.2 Nucleophilic addition of acryloyl chloride

The dried polymer (~ 1 g) and triethylamine (~ 1 mL) were dissolved in dichloromethane (~ 50 mL). The reaction flask was sealed with a rubber septum and connected to an oil bubbler. A nitrogen purge was used for 15 minutes before an excess of acryloyl chloride was added. The reaction mixture was stirred with a magnetic stir bar for ~16 hours at room temperature and then washed with distilled water, sodium bicarbonate, and sodium chloride. The organic layer was precipitated into methanol. The polymer precipitation was dried overnight in a fume hood before drying in a vacuum oven.

3.2.2.3 Aza-Michael addition of 2-methylaziridine

The reaction was prepared in the same fashion as the acryloyl chloride step except for addition of the 2-methylaziridine in excess rather than acryloyl chloride. After ~16 hours, the reaction was precipitated into and washed by methanol. The polymer was dried overnight in a fume hood before drying in a vacuum oven.

3.2.3 Melt Blending with PLA

The PLA (NatureWorks 2003D) and Az-PMMA were dried before melt blending. The blending were carried out in an Xplore MC5 twin screw microcompounder. The compounding conditions were 180 °C, 200 rpm, with nitrogen purge. A normal force readout was used to monitor the reaction progress.

3.2.4 Characterization

^{1}H NMR spectra were obtained with a Bruker Avance III HD nanobay AX-400 spectrometer operating at 400 MHz and 25 °C using a 25s relaxation time and 16 transients. Samples were prepared by dissolving ~ 30 mg of polymer sample in ~ 0.7 mL of $CDCl_3$. Analysis

of functional group's signature protons allowed for determination of mole percent composition, which allowed for calculation of functional unit content, and determination of reaction completion.

Molecular weight was characterized by gel permeation chromatography (GPC) with THF as carrier solvent at room temperature using a Thermo Separation Products Spectra Systems equipped with three 5 mm Phenomenex Phenogel columns, a Waters 515 pump, and a Waters 2410 differential refractive index detector. The reported MWs are based on polystyrene standards.

3.2.5 Extensional rheology

Extensional rheology tests were conducted in the same manner as 2.2.5.

3.3 Results and discussion

3.3.1 Synthesis

Table 3-1 shows the molecular characteristics of aziridine functional PMMA. The molar mass of the poly(MMA-co-HEMA) was controlled by changing initiator concentration and, as expected, was inversely proportional to initiator concentration. The HEMA content in the polymer (calculated from NMR) was roughly half of the HEMA content in the monomer mixer. For polymer C1, NMR (Figure 3-4) showed that the double bond signals at 5.95, 6.2, and 6.5 ppm disappeared after the Michael Addition reaction. Complete conversion of double bond was also observed in polymer C2. But polymer C1' was a version of C1 with incomplete double bond conversion due to insufficient 2-methylaziridine loading during the Michael Addition reaction. The average aziridine functionality of C1' was calculated to be 2.

It is worth mentioning that, when we first tried methacryloyl chloride instead of acryloyl chloride to functionalized the PMMA backbone, the following Aza-Michael Addition didn't proceed (Figure 3-3). Possibly the methyl group reduced the reactivity of the double bond.

Table 3-1 Synthesis and molecular characteristics of aziridine-functional PMMA.

Functional polymer code	Initiator/Monomer weight ratio	HEMA content in monomer (%)	HEMA content in polymer (%)	M_n (kg/mol)	PDI	Average aziridine functionality per chain
C1	0.042	6.3	10	11	1.9	10
C1’	0.042	6.3	10	11	1.9	2
C2	0.003	0.45	1	148	1.8	15

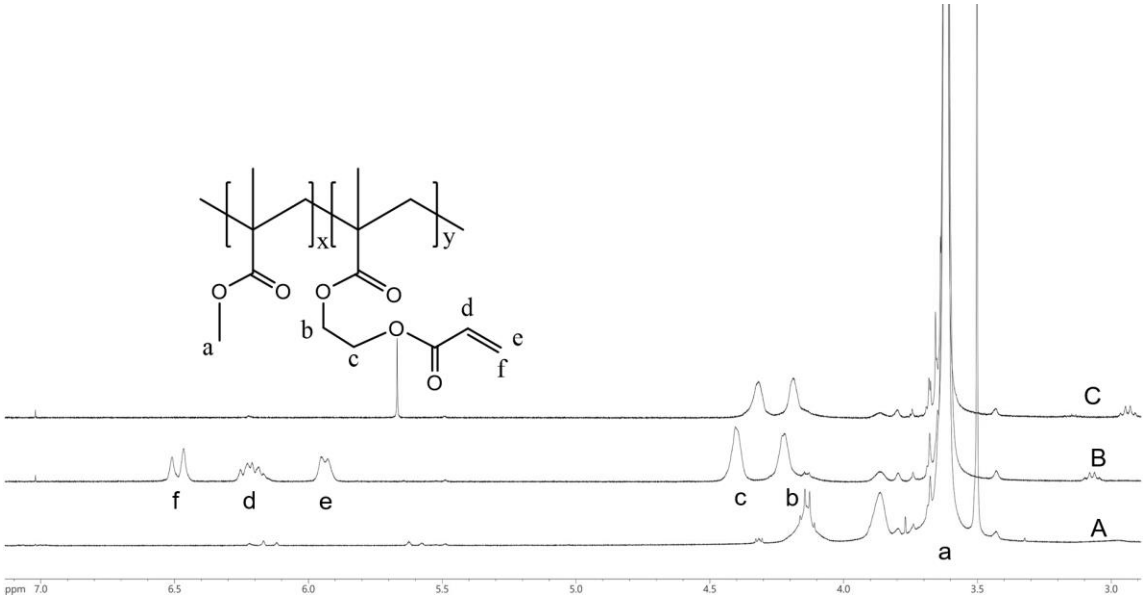

Figure 3-4 ^{1}H NMR spectrum of polymers A, B, and C as illustrated in Figure 3-3 during the synthesis of polymer C1.

3.3.2 Melt blending

Neat PLA was blended with C1 at different concentrations, 1 wt.%, 1.5 wt.% and 3 wt.%. The theoretical molar ratio of aziridine to carboxylic acid groups in those blends, [AZ]/[COOH], is presented in Table 3-2. The molecular weight and polydispersity of PLA blends increased with [AZ]/[COOH], which is a direct result of the branching reaction. In theory, molecular weight of PLA should find its maximum at [AZ]/[COOH] = 1, where all the linear chains are transformed into comb molecules. When [AZ]/[COOH] < 1, molecular weight of branched PLA should increase

with [AZ]/[COOH], and when [AZ]/[COOH] > 1, molecular weight should decrease with increasing [AZ]/[COOH]. However, our results show that C1_3% ([AZ]/[COOH] = 2.4) has a higher molar mass than C1_1.5% ([AZ]/[COOH] = 1.2). At this point we are not able to identify the cause for this contradiction. Although C2_5% and C1'_5% used different branching agents, they fit into the trend that molecular weight of PLA increase with [AZ]/[COOH]. C2_5% has the lowest [AZ]/[COOH] and thus lowest molecular weight.

Table 3-2 Molecular weights of neat PLA and PLA branched with functional PMMA.

Sample code	Weight fraction of functional PMMA	[Az]/[COOH]	M_n (kg/mol)	M_w (kg/mol)	PDI
Neat	-	-	114	214	1.9
C1_1%	1%	0.8	123	321	2.6
C1_1.5%	1.5%	1.2	141	376	2.7
C1_3%	3%	2.4	155	433	2.8
C2_5%	5%	0.4	117	268	2.3
C1'_5%	5%	0.8	117	305	2.6

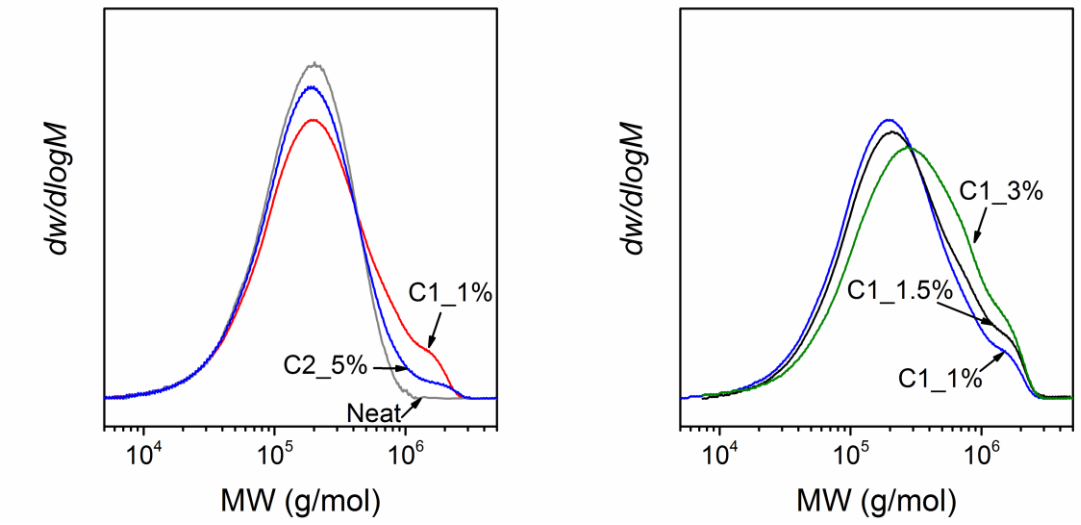

Figure 3-5 Molecular weight distribution of neat PLA and branched samples.

Figure 3-5 presents the GPC traces of the PLA samples listed in Table 3-2. It is evident that there is a higher molar mass fraction (> 1000 kg/mol) in all the branched PLA, and the samples

are actually mixtures of linear chains and branched chains. Based on the synthesis of functional PMMA, we think the high molar mass molecules are comb-shaped.

3.3.3 Extensional rheology

Figure 3-6 compares the extensional viscosity of C1_1% and C2_5%, which have an average spacing between branching points of 1,000 g/mol and 10,000 g/mol, respectively. For all the measured strain rates, C2_5% shows a deep increase in extensional viscosity after a certain strain while strain hardening in C1_1% is more gradual. They can achieve similar extensional viscosity in absolute magnitude before sample rupture but the shear viscosity of C2_5% is much lower than C1_1% (estimated based on extensional viscosity at 0.1 s^{-1}; Table 3-2 shows the molecular weight of C2_5% is lower.). At 10 s^{-1} extension rate, C1_1% does not show any strain hardening but C2_5% does. The magnitude of extensional viscosity of C2_5% even exceeds C1_1% at large strains. The number of branches for C2_5% is slightly higher than C1_1%, 15 vs 10. But it is not huge difference. The effect of this difference should be small. Figure 3-3 shows that the amount of comb chains in C2_5% is lower than C1_1%. Thus we conclude (i) the long backbone and (ii) the large spacing between branch points of C2_5% are responsible for its superior rheological properties. The entanglement molecular weight (M_e) of PMMA is 10,000 g/mol.[114] Spacing in C2_5% is just at the M_e of PMMA. It is widely accepted that strain hardening of branched polymers derives from the stretching of chain segments between branch points, which are not free to relax its stress until the branches have fully retracted.[103] (The branch points will withdraw eventually since it becomes more entropically favorable to withdraw the branches than to continue to stretch the backbone.) Lentzakis et. al[112] showed that when segment length between branch points is below M_e, strain hardening is weak. The backbone total length of C1_1% is only 10,000 g/mol and average spacing between branch points is 1,000 g/mol. Its structure is similar to Joncryl-branched PLA, one short backbone with multiple long arms. And their rheological features are

similar: diminishing extensional hardening at high strain rates (> 3 s^{-1}) in extensional flow and high shear viscosity at low strain rates in shear flow.

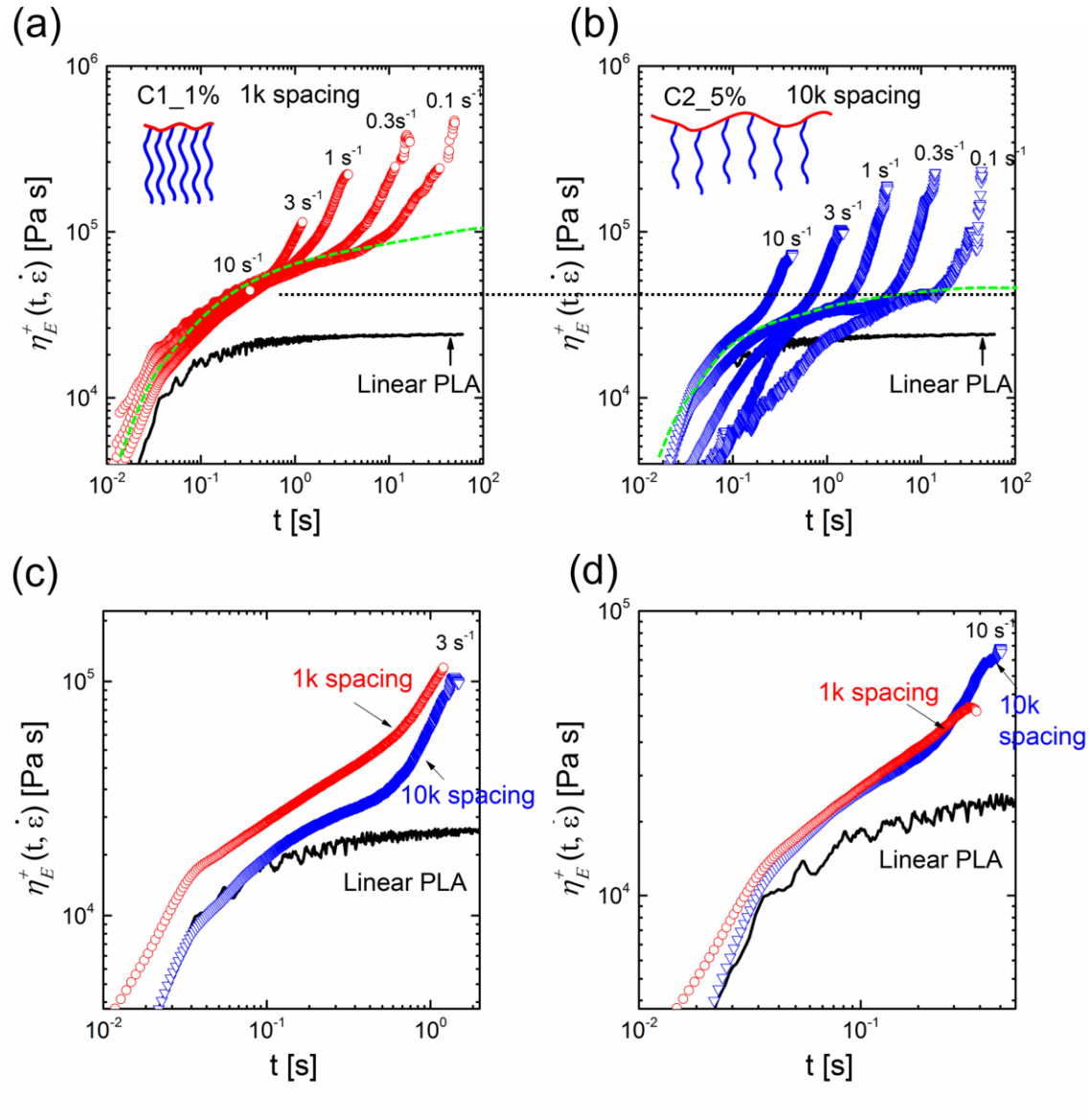

Figure 3-6 Extensional viscosity as a function of step time for C1_1% and C2_5%. The extension rates are 10, 3, 1, 0.3, 0.1 s^{-1}. The dashed lines estimate the linear viscoelastic responses (3×shear viscosity). The dot line helps compare the shear viscosities. (c) and (d) directly compare the extensional viscosities at high strain rates, 3 s^{-1} and 10 s^{-1}, where extensional viscosity of C2_5% exceeds that of C1_1%.

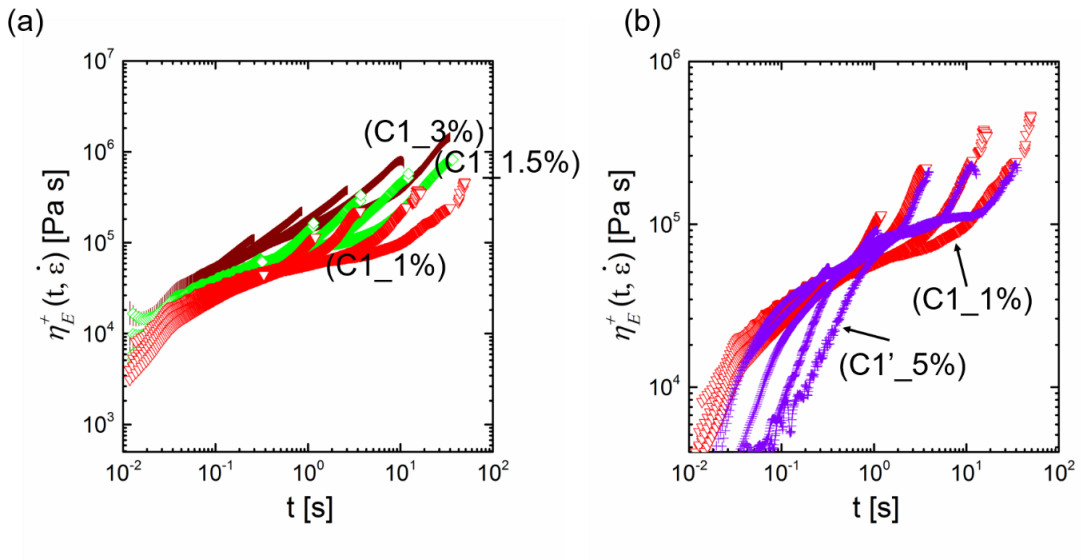

Figure 3-7 Extensional viscosity as a function of step time for C1_1%, C1_1.5%, C1_3%, and C1'_5%. The extension rates are 10, 3, 1, 0.3, 0.1 s^{-1}.

The effect of C1 loading on PLA's extensional viscosity is presented in Figure 3-7a. Increasing C1 loading resulted in higher extensional viscosity. But the extent of strain hardening is not improved. The strain hardening of C1_3% is still gradual after the onset of strain hardening and the shear viscosity is significantly increased.

Based on work by Kempf et. al[100], in comb-shaped polymers, criterions for strain hardening include: (i) number of branches, $n > 2$. They showed that for comb polymers, when $n < 14$, the extent of strain hardening increased linearly with n. After a certain value of n between 14 and 29 was reached, increasing n had then only a low influence on the strain hardening. (ii) molecular weight of branches (or arms), $M_a > M_e$. The extent of strain hardening increases with the molecular weight of the branches.

From a processing point of view, high n means high MW, high viscosity. A moderate n can give enough strain hardening and relatively low viscosity. A super-rough estimation based on Kempf et. al gives $2 < n < 30$. For the special case of branching commercial PLA using

multifunctional aziridine or epoxide, there is no need to worry about M_a because MW of commercial PLA is well above M_e.

Our work suggests that long backbone and large spacing between branching points (M_{seg}) lead to strong extension hardening. For processing, one wouldn't want super-large spacing either because given the same *n*, large spacing means high MW and high shear viscosity. We don't have much data, but one of our cases showed that $M_{seg} = M_e$ would be enough for good strain hardening.

3.4 Conclusions

A model branching agent for PLA was synthesized to study the effect of branching structure on extensional viscosity. The branching agent is comb-shaped with aziridine functional groups. For a comb-shaped PLA, long backbone and large spacing between branching points gave rise to stronger strain hardening and lower shear viscosity (at low strain rates) than short backbone. Our results indicate that, in a mixture of linear PLA and comb-shaped PLA with short backbone, increasing the content of comb PLA would increase the absolute value of extensional viscosity, but not the extent of strain hardening. An ideal branched structure for PLA's melt processing should have (i) multiple entangled branches, (ii) long backbone, and (iii) large spacing between branching points. Here "long" and "large" refer to a commercial product which has a molecular weight of 4 kg/mol.

Chapter 4 PLA/Pluronic blends: correlation between blend properties and Pluronic copolymer structure*

4.1 Background

With a glass transition temperature around 60 °C, PLA is inherently brittle at ambient conditions. Various strategies have been developed to toughen PLA, including copolymerization, plasticization, blending with flexible polymers and addition of rigid fillers.[30] Immiscible blends of PLA with other rubbery polymers are most studied and widely used because of convenient fabrication and low cost. Unlike plasticization which compromises the elastic modulus and tensile strength of PLA, immiscible blends of PLA can retain high modulus and strength. One drawback of immiscible blends is the loss of transparency because the secondary phase is dispersed as micron-sized domains. There are two ways to increase the transparency of PLA blends: use a secondary phase with refractive index close to PLA, or disperse the secondary phase into small enough domains that won't scatter light. This chapter uses a series of commercial poly(ethylene oxide)-poly(propylene oxide)-poly(ethylene oxide) (PEO-PPO-PEO) triblock copolymers, Pluronic® (BASF), which have a matched refractive index with PLA, to prepare tough and transparent PLA blends.

Polyethylene oxide (PEO) is a crystalline polyether and is partially miscible with PLA. The miscibility increases with lower PEO molecular weight.[115 - 120] In PLA/PEO blend, phase separation develops when PEO content exceeds a certain threshold depending on molecular weight and temperature. Miscible PLA/PEO blends typically exhibit good ductility because of the plasticization effect of PEO. However, phase separation of PEO from host polymer PLA during

*Portions of this work was done in collaboration with Elizabeth E. Nessim and Dr. Tuoqi Li. Financial support for this work came from the National Science Foundation through the Center for Sustainable Polymers (CHE-1413862).

crystallization often reduces the ductility. Moreover, because PEO is water-soluble, leaching of PEO from the blend during contact with water limits the applications.[121]

Unlike PEO, polypropylene oxide (PPO) is amorphous and hydrophobic. With a glass transition temperature ~ -70 °C, PPO appears as viscous liquid at ambient conditions. The miscibility of PPO with PLA is worse than PEO. The refractive index of PPO, 1.45 – 1.46 [122, 123], is very close to that of PLA, 1.45 – 1.50[124]. Immiscible blends of PPO with PLA can be transparent. Piorkowska et. al studied the blends of PLA and PPOs with molecular weights of 425 g/mol and 1000 g/mol. Both PPOs are reported to be miscible with PLA below 10 wt.%. Phase separation was detected in the blend containing 12.5 wt. % 1000g/mol PPO, which indicated decreased miscibility with increase of PPO molecular weight. The drawability of PLA/PPO blend increased with PPO content. At 12.5 wt.% loading in PLA, the elongation at break reached 65% and 105% for 425 g/mol PPO and 1000g/mol PPO respectively, while neat PLA broke at 8% elongation. The authors attributed the improved toughness to the phase separated PPO droplets in PLA matrix, which can facilitate local plasticization of PLA during plastic deformation.

A recent work by Li et. al[125] showed that a PEO-based diblock copolymer, poly(ethylene oxide)-poly(butylene oxide) (PEO−PBO), can effectively increase the toughness of PLA at low loadings. The diblock copolymer formed micelles in PLA matrix, which toughened PLA through similar mechanism operative with micelle-modified epoxy materials.[126 - 128] Inspired by this work, we expand the search for PLA toughers to PEO-PPO-PEO triblock copolymers. The refractive index of Pluronic copolymers is 1.45 – 1.47[129], which closely matches that of PLA. An additional advantage of toughening PLA with Pluronic lies in the fact that both components are FDA approved for clinical use so the blend has potential in medical applications.[130, 131] In the present study, we will examine the solubility and toughening effect of different Pluronics with PLA by searching through the so called “Pluronic grid”[132, 133] (Figure 4-2). In the “Pluronic grid”, the notations L, P,

and F indicate whether the copolymer is liquid, paste and flakes (solid) at room temperature. Following the letters, the first one or two numbers multiplied by 300 g/mol are the molecular weight of the PPO block, and the last number signifies the weight fraction of the PEO blocks. Our results showed that some Pluronic grades dramatically increased PLA toughness at low loading (<10 wt.%), without compromising transparency. Simultaneously, the melt viscosity of PLA was reduced by the addition of block copolymer. However, none of the Pluronic copolymers formed micelles in PLA.

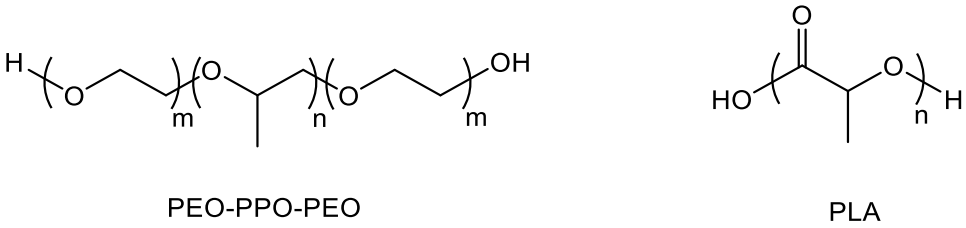

Figure 4-1 Structure of PEO-PPO-PEO triblock copolymer and PLA.

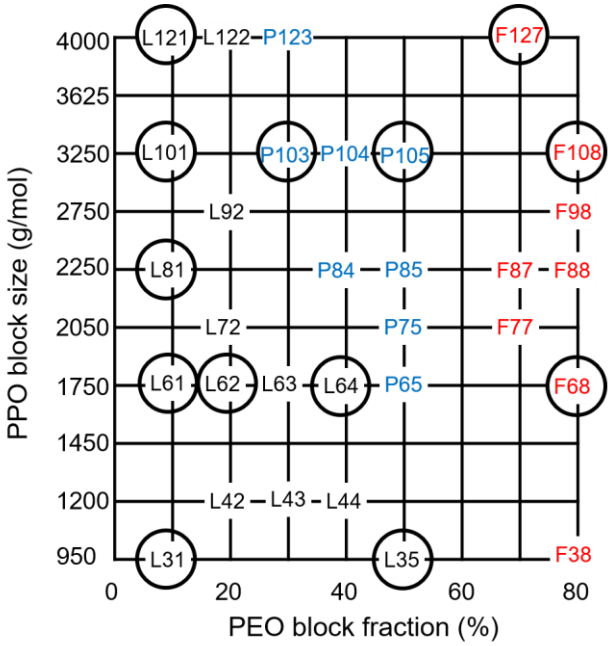

Figure 4-2 Molecular information of Pluronic copolymers displayed in the "Pluronic grid". The circled Pluronic grades were used in this study. The notations L, P, and F indicate whether the copolymer is liquid,

paste and flakes (solid) at room temperature. Following the letters, the first one or two numbers multiplied by 300 g/mol are the molecular weight of the PPO block, and the last number signifies the weight fraction of the PEO blocks.

4.2 Experimental

4.2.1 Materials and blending

Commercial semicrystalline PLA (Ingeo 2003D) is from NatureWorks. Pluronic copolymers are supplied by BASF. PPO homopolymer with a molecular weight of 3, 000 g/mol was obtained from Sigma-Aldrich.

Small batches (20g) of PLA blends with 5 wt.% copolymer (for some Pluronic grades, also 10 wt.%) were first prepared by solvent blending in chloroform to ensure composition accuracy. After chloroform removal, the blends were then melt processed using a twin screw microcompounder (Xplore MC5) to mimic extrusion processing. The compounding conditions were 180 °C, 200 rpm, with nitrogen purge, mixing for 5 min and polymer loading of 4.8g. The mixer normal force, which is proportional to pressure build-up in the twin screw mixer, was recorded to monitor viscosities of the blends during melt processing.

Large batches (300–500 g) of PLA blends with 5 wt.% L121, 5 wt.% L105 and 10 wt.% L121, were prepared for impact test using a 16 mm twin screw extruder (PRISM, L:D 24:1, four heating zones at 180 °C and a feed zone at 160 °C)[134]. The screw speed was set at 20 rpm with a flow rate of 12 g/min. After steady state was achieved, a syringe pump was used to dispense copolymers (P105 was dissolved in acetone to reduce viscosity, roughly 50 wt.% solution) into the feed hopper at a controlled rate. Outlet pressures dropped after copolymers were added (for instance, from 2.8 MPa to 1.4 MPa in the 5 wt.% L121 blend case). Extrudate was chilled in a water bath, dried by air blower, pelletized, and stored in a 40 °C vacuum oven for at least 24h before further processing.

4.2.2 Sample preparation

Tensile test specimens (ASTM D1708, 0.5 mm thick) were prepared on a compression press (Carver Inc.) at 180 °C, followed by rapid cooling (~ 80 °C/min). The large batch blends from twin screw extruder were fed into an injection molder (Morgan Press, barrel temperature = 180 °C, nozzle temperature = 220 ° C, mold temperature = 50 ° C, ram pressure = 4.5 kpsi, pilot valve pressure = 100 psi, clamp force = 13 tons, cycle time = 60 s) to make impact test specimens. Notches were created using an impact specimen notcher (Tinus Olsen 899) according to ASTM D256. All tensile and impact test specimens were aged for 48 h at room temperature prior to testing.

4.2.3 Mechanical property measurements

Uniaxial tensile tests were performed on a tensile tester (Schimadzu Autograph AGSS17 X) with a cross-head moving rate of 5 mm/min. Impact strength tests were conducted using a CEAST instrumented impact strength tester (model 6545) according to ASTM D256. The reported value for each mechanical property represented an average of five specimens.

4.2.4 Rheological measurements

The rheological measurements are conducted in the same way as section 2.2.4.

4.2.5 Thermal Analysis

DSC was employed to determine glass transition (T_g), crystallization (T_c) and melting (T_m) temperatures of the PLA phase in polymer blends containing different block copolymer modifiers. Samples (5 – 9 mg) were placed in hermetically sealed aluminum pans and analyzed with a Q1000 differential scanning calorimeter (TA Instruments). Specimens were first heated at a rate of 10 °C/min to 180 °C and held for 5 min to erase any thermal history, and then cooled to -100 ° C and heated once more to 180 °C at 10 °C/min. All values reported in Table 4-1 were determined during the second heating run.

4.2.6 Microscopy

Scanning electron microscopy (SEM) and transmission electron microscopy (TEM) were employed to study microstructure of the blends. Prior to SEM imaging, smooth cross sections of the un-deformed tensile specimen were prepared by microtome at room temperature using a glass knife. The specimens were then immersed in ethanol to dissolve the block copolymers on the surface. The smooth cross sections were sputter-coated with 50 Å of platinum and imaged with scanning electron microscope (SEM, JEOL 6500) in secondary electron mode at an accelerating voltage of 5 kV and a working distance of 10 mm. Fracture surfaces of tensile specimen were also imaged (without microtome and copolymer dissolution). For TEM, specimens were cryo-sectioned at -100 °C fitted with a diamond knife, producing ultrathin sections (ca. 70 – 90 nm). Thin sections were then vapor stained for 20 min with 0.5 wt.% RuO4 aqueous solution and imaged using transmission electron microscope (FEI Tecnai T12) with a 120 kV accelerating voltage.

4.3 Results and discussion

The thermal properties, tensile properties and mixing force during melt process in the microcompounder of neat PLA and PLA/Pluronic blends are presented in Table 4-1.

4.3.1 DSC

Figure 4-3 shows representative DSC traces of neat PLA and blends with 5 wt.% copolymer during the second heating run, with glass transition temperature (T_g), melting temperature (T_m) and cold crystallization temperature (T_c) presented in Table 4-1. Neat PLA exhibited T_g around 60 °C, T_c around 120 °C, and T_m around 150 °C. All the triblock copolymers reduced T_g of PLA to some extent. When PEO content in the copolymer is fixed, T_g of the bends increased with copolymer molecular weight (Figure 4-3d). For instance, T_g of 5 wt.% L121 blend is 57 °C compared to 49 °C of 5 wt.% L31 blend. None of the blends showed a PEO melting peak (-10 to 66 °C[135]). However, as shown in Figure 4-3b, weak deflection on the DSC traces around -

70 °C was discernible for blend with L121, which corresponds to PPO glass transition[135]. The deflection indicates phase separation of PPO block from the PLA matrix.

Table 4-1 Characterization of neat PLA and PLA/Pluronic blends.

Sample code	f_{PEO} (%)[a]	T_g (°C)	T_c (°C)	T_m (°C)	ε_b (%)	σ_y (MPa)	E (GPa)	Toughness (MJ/m^3)	Mixing force (N)
PLA	-	60	125	151	5 ± 1	50 ± 5	2.2 ± 0.1	1.8 ± 0.4	3400
5 wt.% L31	10	49	105	144, 149	7 ± 1	49 ± 2	1.5 ± 0.1	2.2 ± 0.5	2500
5 wt.% L61	10	51	118	147	26 ± 13	41 ± 3	1.3 ± 0.1	7.1 ± 4.4	2100
5 wt.% L81	10	52	119	147	62 ± 8	38 ± 3	1.7 ± 0.1	11.6 ± 3.0	1040
5 wt.% L101	10	54	129	149	94 ± 23	32 ± 4	1.2 ± 0.1	19.4 ± 3.3	500
5 wt.% L121	10	57	131	149	128 ± 15	40 ± 3	1.5 ± 0.2	35.2 ± 5.7	800
5 wt.% L35	50	50	105	144, 150	4 ± 1	45 ± 2	1.7 ± 0.1	1.3 ± 0.4	2600
5 wt.% L62	20	51	108	142, 149	6 ± 1	48 ± 2	1.8 ± 0.2	1.8 ± 0.6	2200
5 wt.% L64	40	49	102	143, 150	4 ± 0.4	46 ± 3	1.8 ± 0.1	1.0 ± 0.2	2350
5 wt.% F68	80	51	111	146	5 ± 2	40 ± 1	2.0 ± 0.1	1.3 ± 0.5	2200
5 wt.% P103	30	55	124	148	77 ± 15	29 ± 4	1.9 ± 0.1	10.6 ± 1.3	1000
5 wt.% P105	50	53	130	150	73 ± 25	33 ± 4	1.7 ± 0.1	14 ± 6.0	1550
5 wt.% F108	80	51	127	148	4 ± 1	39 ± 2	2.0 ± 0.1	1.0 ± 0.2	2000
5 wt.% F127	70	49	100	143, 150	8 ± 4	35 ± 2	1.8 ± 0.1	1.9 ± 1.2	1900
5 wt.% PPO	0	58	135	152	86 ± 12	31 ± 2	1.8 ± 0.1	11.6 ± 2.5	650
10 wt.% L121	10	55	131	150	166 ± 34	31 ± 2	1.6 ± 0.1	34.2 ± 6.8	430
10wt% L31	10	47	102	142, 150	4 ± 1	39 ± 2	1.1 ± 0.1	1.7 ± 0.4	1770

[a] f_{PEO} is the weight fraction of PEO in the Pluronic block copolymer, provided by manufacturer.

PLA cold crystallization peak was shifted from 120 °C to 100 °C in 5 wt.% L31 blend. Similar trend was reported for PLA plasticized with low molecular weight poly(ethylene oxide)[120, 136] and it was argued that the plasticizer increased segmental mobility and decreased crystal lamellae surface energy of PLA, thus promoted the ability of PLA to crystalize. On the contrary, the diminished crystallization peak and melting peak in in 5 wt.% L101 and 5 wt.% L121 blends suggests that cold crystallization rate was largely reduced. Those two blends showed phase separation of PPO. We suspect that the nucleation agents (impurities, trace catalyst) in the PLA migrated to the PPO phase thus the crystal nucleation became more difficult in those blends.

In Figure 4-3a, the L31 blend showed two melting peaks at 144 °C and 150 °C. Previous work explained this as the reorganization of PLA crystal structure in the presence of plasticizer[118,

[137]. The effect of copolymer concentration on blend thermal property was studied for L121, as shown in Figure 4-3c. T_g reduction and crystallinity reduction were enhanced when concentration of L121 increased from 1 wt.% to 10 wt.%.

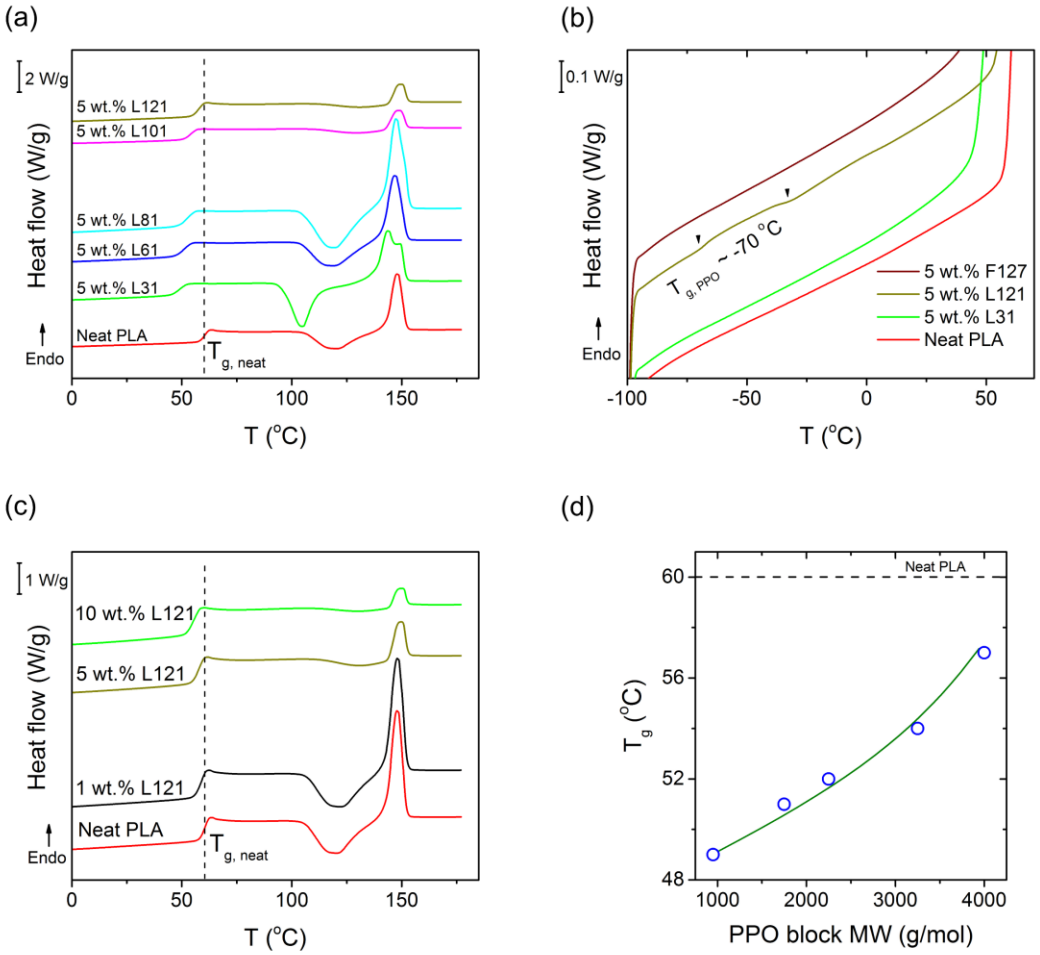

Figure 4-3 Thermal properties of PLA and blends containing 5 wt.% copolymers. (a) DSC thermograms during the second heating cycle. (b) Low temperature region in DSC thermograms. PPO glass transition can be identified around -70 °C in the L121 blend, but not for the L31 or F127 blends. (c) Effect of copolymer concentration on thermal properties of L121 blends. (d) Correlation between PPO block size and glass transition temperature of PLA blends with 5 wt.% copolymers which contain 10% PEO (L31, L61, L81, L101, and L121).

4.3.2 Microscopy

Figure 4-4 shows the transmission electron microscopy (TEM) images of representative PLA blends. In L31 blend there is almost no phase separation. This is consistent with the DSC results which show that L31 is miscible with PLA. Figure 4-4b shows that L121 phase separates from the PLA matrix. The SEM morphology in Figure 4-5 suggests that the large holes in Figure 4-4b were originally large L121 liquid droplets which disintegrated from the thin section during microtoming. There is much less holes in blend with 5 wt.% F127 because the droplets are small and they didn't disintegrate form the thin section. We think the mixing entropy contribution in 5 wt.% L31 blend is more significant due to low molecular weight, while in 5 wt.% L121 blend the unfavorable interaction between PLA and long PPO block dominates the phase separation.

Li et. al[125] showed that poly(ethylene oxide)-poly(butylene oxide) (PEO-PBO, 2k-5k) di-block copolymer can form micelles in PLA. The PEO corona is miscible with PLA due to a negative Flory-Huggins interaction parameter between PLA and PEO. The micelle core is composed of PBO block whose interaction with PLA is unfavorable. Pluronic L121 has a short PEO block and a long PPO block that is less miscible with PLA. But it did not form micelles, possibly due to the weaker hydrophobicity of PPO than PBO.

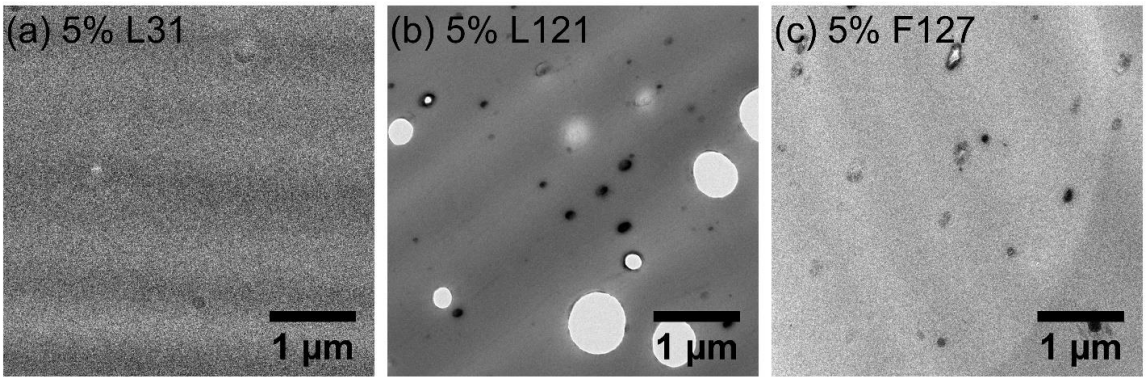

Figure 4-4 TEM images of PLA/Pluronic blends. Blends contain 5 wt.% of (a) L31, (b) L121, (c) F127. The contrast agent RuO4 preferentially stains the PPO phase.

The SEM images in Figure 4-5 further elucidate the development of immiscibility with increasing PPO block size at fixed PEO block fraction (10%). The number-average droplet diameter increased from 0.2 μm in L61 blend to 0.8 μm in L121 blend. Figure 4-6 shows the effect of PEO block fraction on the blend morphology. The droplet size decreased with increasing PEO fraction, until at 80% PEO, the block copolymer fully dissolved in PLA matrix. In blends with L121, the droplet size increased with L121 loading, as presented in Figure 4-7. The droplets in 1 wt.% L121 blend were all submicron while blend with 5 wt.% L121 had lots of large droplets (1-2 μm diameter).

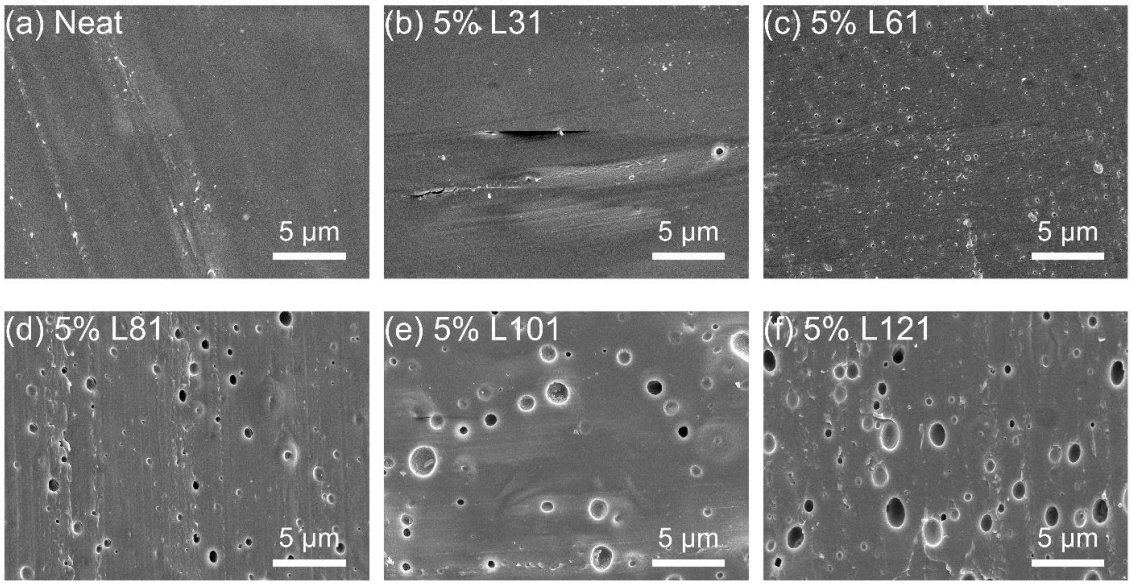

Figure 4-5 SEM images showing the effect of PPO block size of Pluronics on blend morphology. (a) Neat PLA, (b) 5 wt.% L31 blend, (c) 5 wt.% L61 blend, (d) 5 wt.% L81 blend, (e) 5 wt.% L101 blend, (f) 5 wt.% L121 blend. The block copolymers were removed by ethanol.

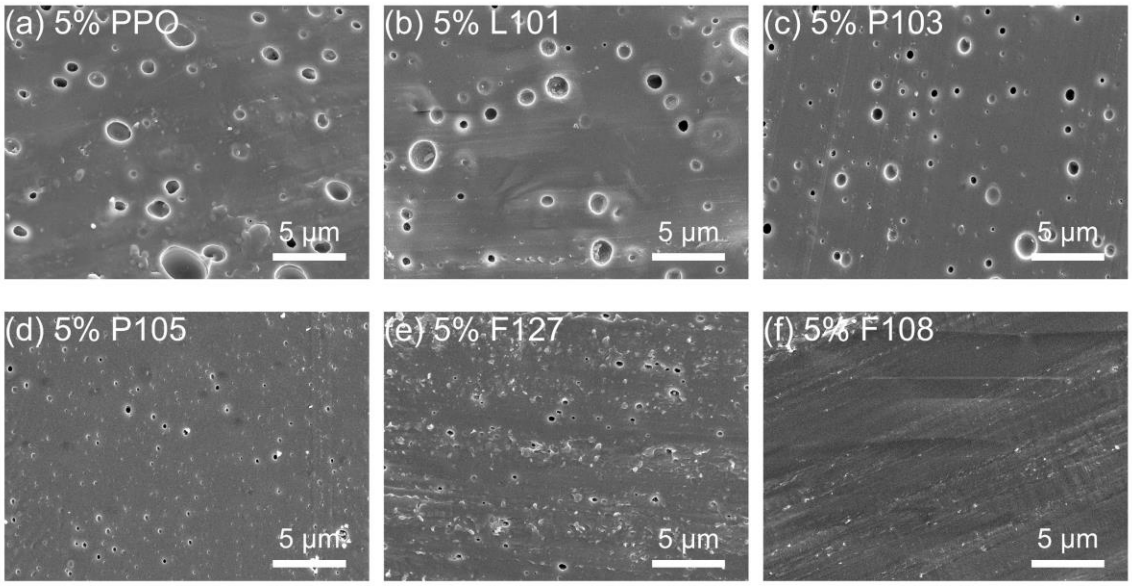

Figure 4-6 Effect of PEO block fraction of Pluronics on blend morphology. (a) 5 wt.% PPO blend, (b) 5 wt.% L101 blend, (c) 5 wt.% P103 blend, (d) 5 wt.% P105 blend, (e) 5 wt.% F127 blend, (f) 5 wt.% F108 blend.

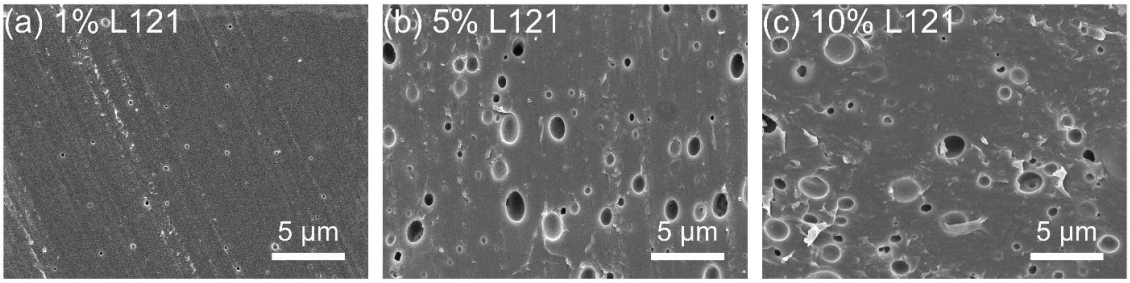

Figure 4-7 Effect of L121 concentration on blend morphology.

Both the DSC and morphology analysis suggest that the miscibility of Pluronic copolymers with PLA decreases with increase of PPO block size and decrease of PEO block content. At 5 wt.% loading, L31, L35, F68, and F108 are fully miscible with PLA. Although not explored in this study, F98, F88, and F38 should also be miscible with PLA because their molecular weights are lower than F108. In semi-immiscible blends (i.e. L121, P105), as the miscibility increases, T_g of PLA decreases because the amount of dissolved copolymer gets higher. The non-dissolved copolymers appear as droplets in PLA matrix and the droplet size decreases with increasing miscibility.

4.3.3 Mechanical properties

Figure 4-8 shows the tensile test stress-strain curves for some representative PLA blends with 5 wt.% block copolymers. Neat PLA broke at a strain of 5%. Some Pluronic grades (L101, L121) can increase the elongation a lot while others have no toughening effect at all (L31, F108). In toughened blends, the engineering stress dropped suddenly upon passing the yield point ($\varepsilon \sim 2.4\%$), to around 50% of the yield stress (σ_y), and then increased slowly as deformation continued. Stress in the plastic deformation region was proportional to yield stress. Some other properties from tensile test are presented in Table 4-1. Young's modulus (E) and yield stress was reduced by the addition of copolymers. In blends showing no toughening effect, the yield stress reduction was not significant, < 20%. It is worth mention that blend with 5 wt.% L121 exhibited the highest elongation (127%), but relatively small decrease in σ_y (20%). As a result, its tensile toughness is 17 times higher than neat PLA. To better correlate the toughening performance with the block copolymer structure, strain at sample break (ε_b) was plotted onto "Pluronic grid" in Figure 4-9. Two general trends can be extracted. First, at low PEO content side, ε_b increases with the molecular weight of PPO block. Second, ε_b decreases with increasing PEO block fraction in the copolymer. Considering the miscibility discussed in 4.1 and 4.2, we conclude that the tensile toughness of PLA/Pluronic blends increases as the miscibility of Pluronic with PLA decreases.

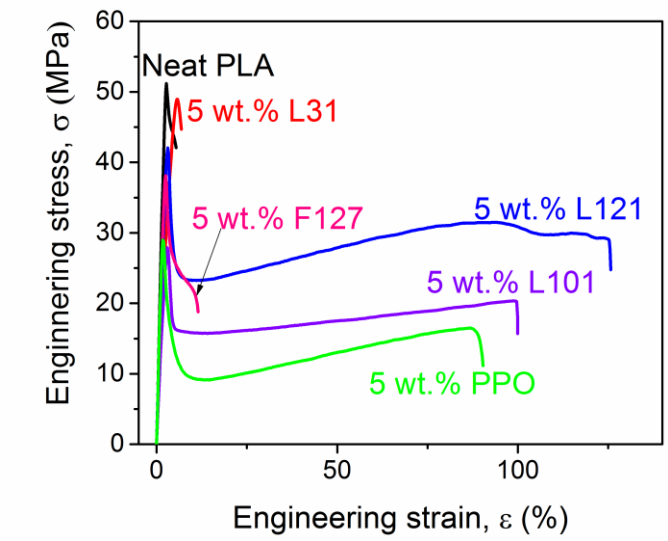

Figure 4-8 Engineering stress-strain curves of neat PLA and blends with Pluronic (5 wt.%).

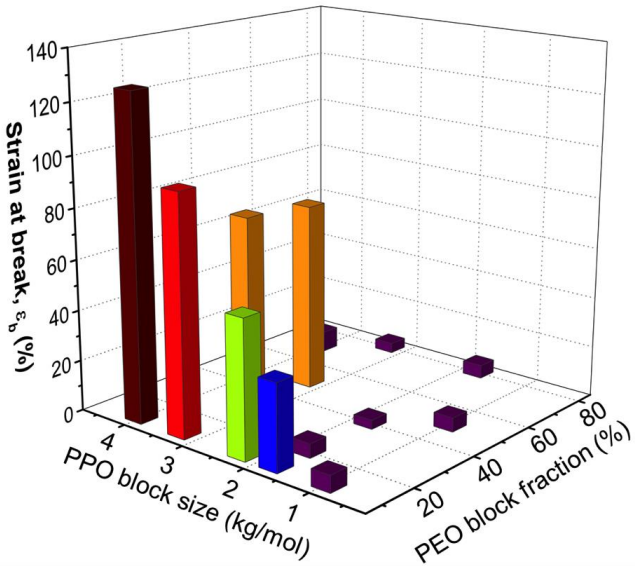

Figure 4-9 Engineering strain at sample break of PLA/Pluronic blends as a function of PPO block size and PEO block fraction. Pluronic loading is 5 wt.% for all.

Figure 4-10 presents the failure behaviors of representative blends. All the specimens were transparent before deformation. Upon applying tensile stress, 5 wt.% L121 blend showed uniform

whitening in the gauge region while 5 wt.% L31 blend broke at low strain without any notable change in appearance (same as neat PLA). Strain whitening was also observed in 5 wt.% L61, L81, L101, P103, P105, and PPO blends. Figure 4-11c shows that the fracture surface of 5% L121 blend is rough, with micron-sized voids. 5 wt.% L31 blend has smooth fracture surface like neat PLA. Interestingly, F127 blend showed slight whitening after stretch, but the fracture surface is smooth, with very shallow indentations. Piorkowska et. al[138 - 141]have studied the toughening mechanism of PLA blends with PEO and PPO-based polymers. They argued that the liquid droplets in PLA matrix can promote initiation and propagation of crazes, which significantly enhanced the plastic deformation of PLA. We think the L121 blends share the same toughening mechanism. The whitening of gauge region is possibly caused by intensive crazing. Although F127 is solid at room temperature, it slightly increases the ability of PLA to craze, which can be visibly identified in Figure 4-10.

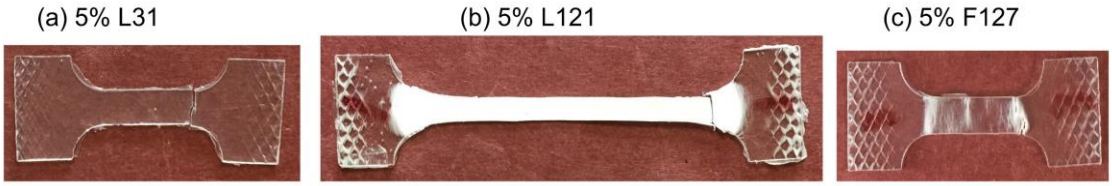

Figure 4-10 Typical failure behaviors in tensile test for PLA/Pluronic blends.

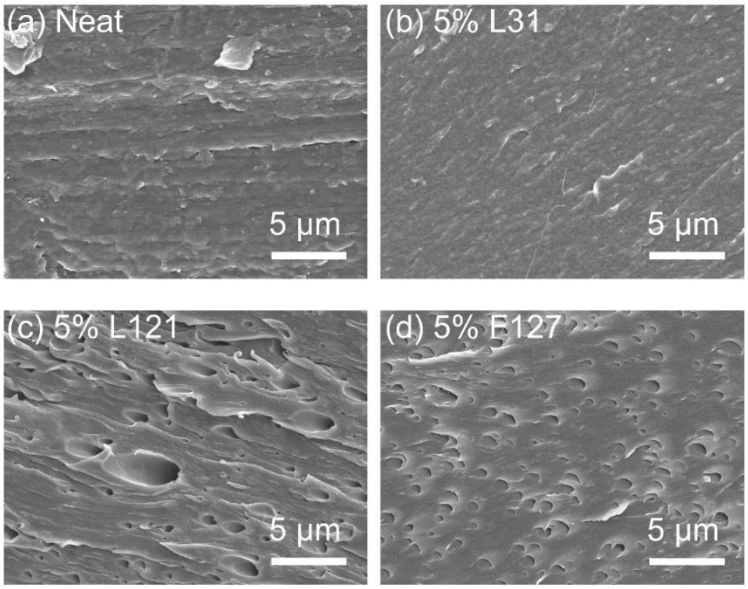

Figure 4-11 Fracture surface of tensile test specimen. (a) Neat PLA, (b) 5 wt.% L31 blend, (c) 5 wt.% L121 blend, (d) 5 wt.% F127 blend. No selective solvent was applied to any sample.

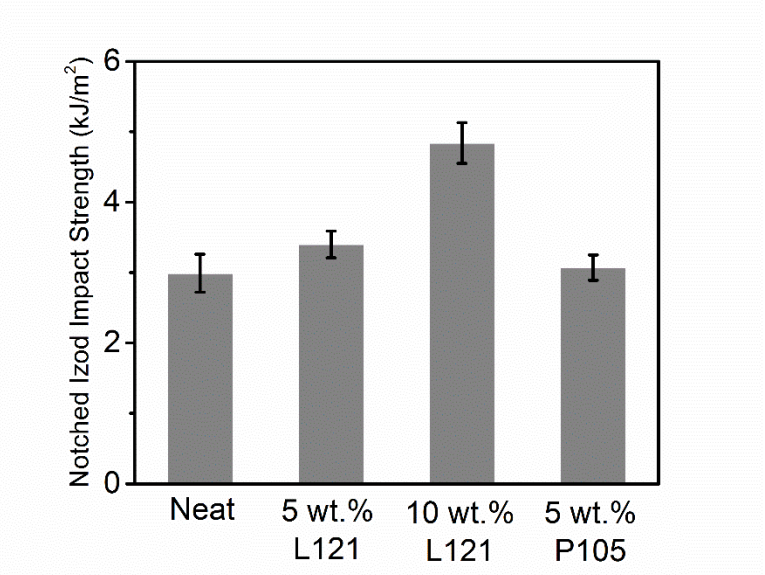

Figure 4-12 Notched Izod impact strength of neat PLA and blends with L121 and P105.

Figure 4-12 shows the notched Izod impact strength of PLA blends with L121 and P105. At L121 loading of 10 wt.%, only 1.5 fold increase in the impact toughness was achieved with respect to neat PLA. 5% P105 blend showed no improvement in impact toughness though its tensile

toughness was 7 times higher than neat PLA (Table 4-1). We think the discrepancy between tensile toughness and impact toughness has its origin in the high strain rate of impact test. [142, 143]

4.3.4 Rheological properties

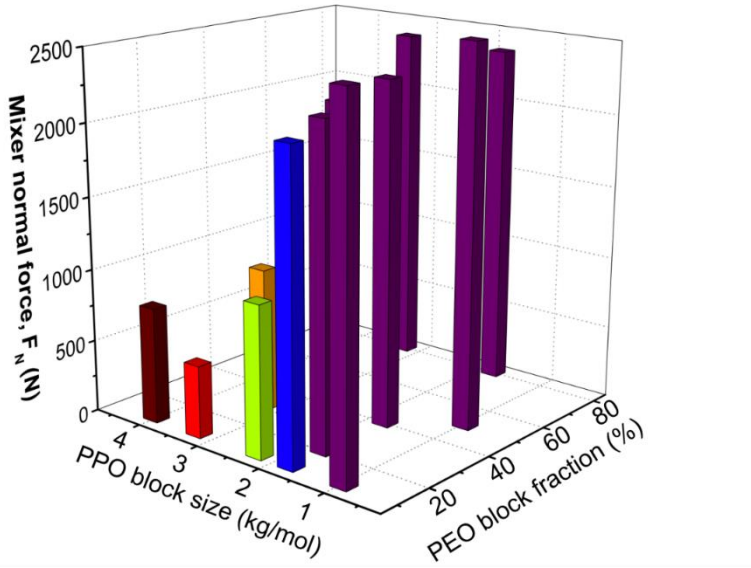

Figure 4-13 Mixing force of different blends as a function of PPO block size and PEO block fraction.

Melt blending was carried out in an Xplore® MC5 batch mixer. The mixer can record mixing normal force, F_N (Figure 4-13, Table 4-1), which is proportional to blend viscosity.[144] At polymer loading of 4.8g, neat PLA had a mixing force of 3400 N. Comparing Figure 4-13 with Figure 4-9 reveals that blends with low ε_b maintain high F_N but blends with high ε_b show low F_N. In an extreme case (L101), F_N of the blend is only 15% of neat PLA. In other words, toughening PLA with Pluronic brings an additional advantage of lowered blend viscosity which reduces energy cost and equipment requirement in extrusion processes.

L31 and L121 are two extreme cases with high and low mixing forces. Their viscoelastic properties were further probed by small amplitude oscillatory shear (SAOS) test (Figure 4-14). The storage modulus of L31 blend is ~ 40% of neat PLA over a wide frequency range of 0.1 – 100 s^{-1}. However, L121 blend shows higher storage modulus than neat PLA at low frequency. This

behavior is typical of immiscible polymer blends with minor phase dispersed as droplets.[145] So the rheological properties agree with the morphology analysis in Figure 4-5. Unlike the mixing force in Figure 4-13, complex viscosity of L31 is almost the same as L121. During melt extrusion of 10 wt.% L121 blend, small amount of L121 liquid dripped out of the compounder. The unincorporated liquid can serve as lubricant between PLA and screws. As shown in Figure 4-15, the inner-surface layer of 5 wt.% L121 blend is depleted of droplets, which presumably migrated to the outer-surface and formed a thin layer of liquid lubricant. This also accounts for some PLA/Pluronic blends' low adhesion with the mixing chamber. Neat PLA is sticky to metal surfaces due to its high surface coefficient of friction. But PLA blends with 5 wt.% L61, L81, L101, L121, P103 and P105 can easily release from metal molds. These Pluronic grades are potential candidates for reducing the sticking problem during PLA processing.

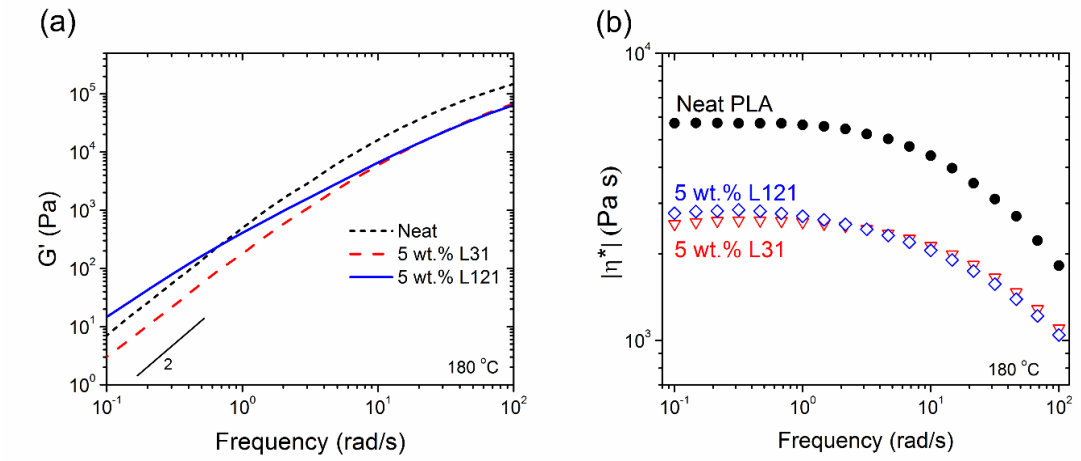

Figure 4-14 Storage modulus and complex viscosity of neat PLA, 5 wt.% L121 blend, and 5 wt.% L31 blend.

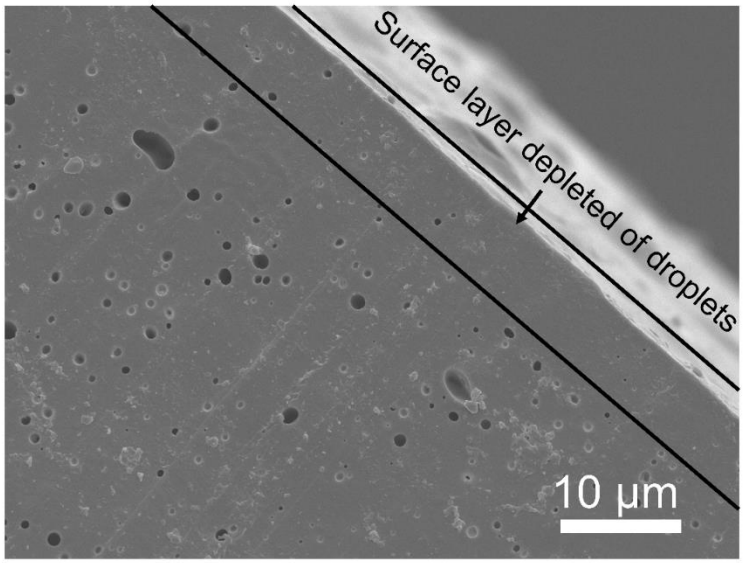

Figure 4-15 Surface morphology of 5 wt.% L121 blend showing depletion of L121 droplets from the inner-surface layer.

4.4 Conclusions

Toughened PLA blends were prepared by melt mixing with commercially available PEO-PPO-PEO copolymers (Pluronic). The blends were examined in terms of morphological, thermal, mechanical and rheological properties. The miscibility of Pluronic with PLA increased with decreasing PPO block molecular weight and increasing PEO block content. The blends with low miscibility are phase-separated and Pluronic liquids dispersed in PLA matrix as droplets. Increasing miscibility resulted in several property changes, namely decreased droplet size, decreased T_g, decreased toughness and increased mixing force. In the best case (L121, least miscible with PLA), the blend's tensile toughness achieved 17 times of neat PLA at copolymer loading of 5 wt.%. However, miscible PLA/Pluronic blends showed no improvement in toughness at all. In phase separated blends, Pluronic copolymer can migrate to the surface of PLA and serve as lubricant, which significantly reduced the melt mixing torque and adhesion to metal surface. This can be

beneficial for reducing processing energy cost and solving sticking problem of PLA products. All the PLA/Pluronic blends are transparent due to matched refractive index.

Chapter 5 Cocontinuous PLA/PS blends: reactive compatibilization and its application to preparation of hierarchically porous PLA*

5.1 Background

Porous PLA has drawn considerable attention in biomedical engineering applications (e.g., drug release, biomedical scaffolding) due to the renewable, biocompatible and biodegradable nature of PLA[146, 147]. Various strategies including foaming, solvent casting, electrospinning, injection molding, cocontinuous polymer blends, and block copolymer microphase separation have been developed to make porous PLAs that possess different morphologies induced by their specific preparation routes[148 - 151]. Among those methods, cocontinuous polymer blends generate porous structures featuring connected, open-channel pores and high mechanical strength. Moreover, recent research showed that dually cocontinuous ternary polymer blends can be used to make hierarchically porous polymer material.[152, 153] In applications like tissue scaffolding, hierarchically porous structures have advantages of providing both high pore accessibility and high specific surface area[154 - 156]. Large pores at the micrometer scale can allow cell penetration and tissue ingrowth, while submicron small pores are designed to favor the expression of extra-cellular matrix components and store growth factors for cell differentiation[154, 157] . In this chapter we used reactively compatibilized ternary polymer blends to prepare hierarchically porous PLA.

As introduced in Chapter 1, cocontinuous blends are often compatibilized to stabilize the morphology. In the literature, cocontinuous PLA/polystyrene (PS) blends has been used as a model system to produce porous PLA[158 - 160], but few studies can be found for the compatibilization of PLA/PS blend. Sarazin and coworkers[157] made porous PLA from 50/50 vol.% PLA/PS blend by

* Reproduced in part from "L. Gu, E. E. Nessim, C.W. Macosko, Polymer 134 (2018) 104–116.". Financial support for this work came from the IPRIME program of the University of Minnesota (80%) and the National Science Foundation through the Center for Sustainable Polymers (CHE-1413862) (20%).

extracting the PS phase with cyclohexane. They further demonstrated that adding 6 wt.% premade PLA-PS diblock copolymer can stabilize the morphology and significantly reduce pore size. Compared to premade copolymers, which must diffuse to the interface, reactively formed interfacial copolymers are more effective at stabilizing immiscible polymer blends.[161, 162] PLA-based blends are suitable for reactive compatibilization because PLA is self-functionalized with -OH and -COOH at the chain ends. Some common interfacial reactions for PLA blends include hydroxy/anhydride, hydroxy/isocyanate, carboxylic acid/epoxy. Oxazoline group can also react with carboxylic acid, resulting in an amido-ester unit.[163] Although the carboxylic acid/oxazoline reaction has been applied to compatibilization of PS/PE blends[164, 165], PS/polyamide blends[166], and others[167 - 170], compatibilization of PLA blends with oxazoline-functionalized polymer is rarely reported[171].

This chapter aims to study the compatibilization effect of the carboxylic acid/oxazoline reaction on PLA/PS blends and use it to make hierarchically porous PLA. Oxazoline functionalized polystyrene (PS-OX) was blended with PLA and the effect of reactive compatibilization on blend morphology and stability is discussed. Hierarchically porous PLA was prepared from ternary PLA/PS-OX/LLDPE blends. Thermodynamic interactions of the three components are examined in terms of wetting behavior.

5.2 Experimental

5.2.1 Materials

Two polystyrene (PS) resins from the Dow Chemical Company were used: nonreactive polystyrene (PS, Styron™ 666D, now supplied by Americas Styrenics LLC) and reactive polystyrene containing 1% of vinyl oxazoline as a comonomer (PS-OX, RPS XUS140056.01). Poly(lactic acid) resin was obtained from Natureworks LLC (PLA, Ingeo™ 2003D). Figure 5-1 shows the reaction of PS-OX with PLA. Linear low density polyethylene (LLDPE, Engage™ 8180),

high density polyethylene (J-rex HD KF 251A) and styrene-b-ethylene/butadiene-b-styrene tri-block copolymer (SEBS, Kraton 1657) were obtained from Dow Chemical Company, Japan Polyolefins, and Kraton Corporation, respectively.

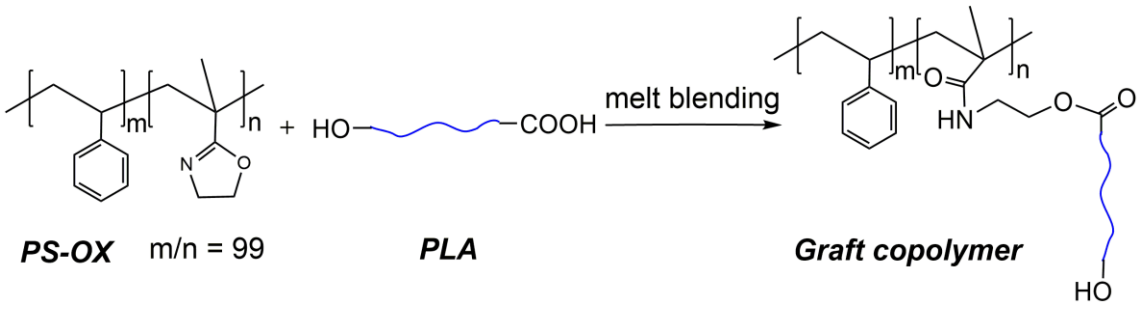

Figure 5-1 Chemical structure of random copolymer PS-OX and its reaction with PLA.

The relevant material properties are shown in Table 5-1. The molecular weight of PS and PLA samples was characterized on a GPC with THF as the carrier solvent at room temperature (Thermo Separation Products Spectra Systems, Waters 2410 RI detector). PE resins were analyzed using high temperature GPC (PLA-GPC 220, Agilent systems, 135 °C, 1,2,4-tri-chlorobenzene eluent, RI detector). Molecular weights reported are based upon polystyrene standards.

Table 5-1 Resin information.

Material	M_n (kg/mol)	PDI	ρ (g/cm^3) @ RT	ρ (g/cm^3) @ 180 °C	η_0 (kPa s)@ 180 °C	MFI[a] (g/10 min)
PS	88	2.5	1.04[a]	0.983[b]	23.2	8 (200 °C, 5 kg)
PS-OX	104	2.5	1.04[c]	0.983[c]	26.4	-
PLA	120	1.9	1.24[a]	1.12[a]	6.6	6 (210°C, 2.16kg)
LLDPE	56	2.4	0.865[a]	-	33.2	0.50 (190ºC, 2.16 kg)
HDPE	6.6	22	0.945[a]	-	30.0	-

[a] Data provided by suppliers. [b] PS density at 180℃ is calculated based on Wulf et. al[172]. [c] PS-OX density is assumed to be the same as PS.

5.2.2 Rheology

Rheological properties of pure materials and blends were measured via small amplitude oscillatory shear (SAOS) on an ARES rheometer (TA Instruments) at 180 °C, using 25-mm parallel

plates. Strain sweep tests were performed at a frequency of 1 rad/s to define the region of linear viscoelasticity. Frequency sweeps over a range of 100 – 0.02 rad/s were then conducted at strains within the linear viscoelastic range. Disk-shaped specimens were prepared by compression molding at 180 °C for 3 minutes and vacuum dried at 40 °C for 12 h prior to rheological measurements. At least two measurements for each material were conducted. Results are shown in Figures 1 and S1.

5.2.3 Blending and quiescent annealing

Blends were prepared using a recirculating, conical twin-screw batch microcompounder (Xplore Instruments, Xplore MC5) with a mixing capacity of 5 cm^3, at 180 ℃ and a rotation speed of 200 RPM. For binary PLA/PS and PLA/PS-OX blends, the total amount of polymers put into the microcompounder was 4 cm^3 at 180 ℃. The mixing time was 6 min or 30 min. For ternary blends, PLA, PS, and LLDPE pellets (4 cm^3 in total) were loaded into chamber at the same time and mixed for 30 min. The blends were extruded into liquid nitrogen to freeze the morphology. After vacuum drying the blends at 40 ℃ for 12 h, quiescent annealing was performed at 180 ℃ for various times on a compression press (Carver, Inc., Wabash, Indiana). Samples were placed into 3 mm thick molds sealed by two metal plates under 5000 lbs press force. Upon completion of annealing, the plates were immediately transferred to a separate chilled compression press for rapid cooling (temperature dropped down to room temperature within 1 min) to freeze the morphology.

5.2.4 Solvent extraction and determination of cocontinuity

The binary PLA/PS blends were soaked in cyclohexane at 50 °C to extract all continuously connected regions of PS. After the extraction, the specimens were then vacuum dried at 40 °C for 24 h. The PS continuity, Φ_{PS}, was measured gravimetrically[173]:

$$\Phi_{PS} = \frac{m_i - m_f}{m_{PS,i}} \quad (5\text{-}1)$$

where m_i is the initial mass of the blend, m_f is the final mass following extraction in cyclohexane, and $m_{PS,i}$ is the initial mass of the PS in the blend. 3 specimens for each blend composition were

measured. A fully continuous PS phase can be considered as one demonstrating a PS continuity of 1, whereas a PS continuity approaching zero was indicative of a discontinuous PS phase. In this study, $\Phi_{PS} \geq 0.9$ was treated as a continuous PS phase. PLA continuity was determined by the ability of the blend to remain self-supporting after PS extraction. A blend that disintegrated after the cyclohexane wash indicated a discontinuous PLA phase. Therefore, a cocontinuous blend was defined as one with $\Phi_{PS} \geq 0.9$ and with structural integrity after extraction in cyclohexane. The range of cocontinuity for a blend system was defined as the range of compositions that displayed these properties.

5.2.5 Laser scanning confocal microscopy

Cocontinuous blends were imaged in 3D using laser scanning confocal microscopy (LSCM, Olympus Fluo View 1000). LSCM imaging requires the samples to be optically transparent for laser to penetrate and have fluorescent contrast between the phases. The PLA/PS and PLA/PS/LLDPE blends were not optically transparent, due to refractive index mismatch, and were not fluorescent. In order to generate optically clear samples, blends were cut into thin slices (~100 μm thick) with a razor blade and subsequently the slices were soaked in cyclohexane at 50℃ overnight to extract the continuous PS and LLDPE phases. The extracted slices were placed between a glass slide and coverslip. This space was then filled by pipette with 13/87 wt.% ethanol/dimethyl sulfoxide (DMSO) mixture containing 0.01wt.% Rhodamine B fluorescent dye. The mixture filled the pores of the thin slice. The cover slides were then sealed with epoxy resin to avoid mixture evaporation. The refractive index of the ethanol/DMSO mixture matched that of PLA and the specimen became optically transparent and fluorescent.

For imaging, an incident laser beam of wavelength of 543 nm excited fluorescence from the Rhodamine B dye dissolved in ethanol/DMSO. Images are acquired at 560 – 660 nm. The ethanol/DMSO fluorescent mixture was identified as the bright regions under LCSM. An oil-immersed, 60× objective lens was used with LSCM to obtain a stack of 2D optical micrographs.

The focal depth increment, Δz, was 0.4 μm. Using Avizo (v. 6.3, http://www.vsg3d.com/avizo), these images were binarized so that black represented non-fluorescent PLA and white the fluorescent mixture. 3D reconstruction of the blend structure was then generated from a stack of 2D images at different focal depth. A triangular mesh was applied along the black-white interface using a marching cubes algorithm included in the Avizo software package. From these 3D reconstructions, a characteristic size of the blends, *a*, could be calculated [174]:

$$a = V/\sum_{i=1}^{N} A_i \quad (5\text{-}2)$$

where V is the total volume of the image stack, and A_i is the area of a single triangle of the interfacial triangular mesh. The reported characteristic size represents an average over 3 stacks of images for each sample.

5.2.6 Scanning electron microscope (SEM)

Some blend structures were examined by scanning electron microscopy (SEM, JEOL 6500). Prior to imaging, smooth cross sections of the blends were prepared by cryo-microtome (Reichert UltraCut S Ultramicrotome) at -140°C using a glass knife. Blends were then immersed in cyclohexane at 50 °C overnight to dissolve the PS. Extracted blends were dried in a vacuum oven and sputter coated with 5 nm of platinum to create a conductive surface, and were then imaged at an accelerating voltage of 5 kV and a working distance of 10 mm. In image analysis, the blend interface was manually traced using ImageJ. The total length of the interface in a specific SEM image, L, was then measured by MATLAB. The characteristic polymer phase size, a', can be determined as

$$a' = L/A \quad (5\text{-}3)$$

where A is the total area of the SEM image. 3-5 SEM images were measured for each sample to get the average characteristic size.

5.3 Results and discussion

Sections 5.3.1, 5.3.2 and 5.3.3 present results of binary PLA/PS blends, in terms of rheology, melt reaction, cocontinuity, and morphology. The effect of reactive compatibilization will be emphasized. Sections 5.3.4 and 5.3.5 present the results of ternary PLA/PS/PE blend, which is hierarchically structured. The discussions of the ternary blends rely on the findings from the binary PLA/PS blends.

5.3.1 Rheology and melt reaction of binary blends

Complex viscosity (η^*) and storage moduli (G') of PS, PLA and cocontinuous blends at 180℃ are plotted in Figure 5-2. The functional polystyrene (PS-OX) was found to have very similar rheological properties as the nonfunctional polystyrene (PS). Complex viscosity of PS-OX was slightly higher (~ 10%) than PS and storage modulus was almost the same over a frequency range of 0.1 – 100 rad/s. For analysis in melt blending, this difference is small enough that PS and PS-OX can be treated as rheologically identical. Compared to the polystyrenes, PLA had a much lower viscosity at frequency below 1 s^{-1} and showed less shear thinning. The PLA/PS-OX blend showed much higher elasticity and viscosity than the PLA/PS blend at low frequency, but their rheological properties were close at high frequency.

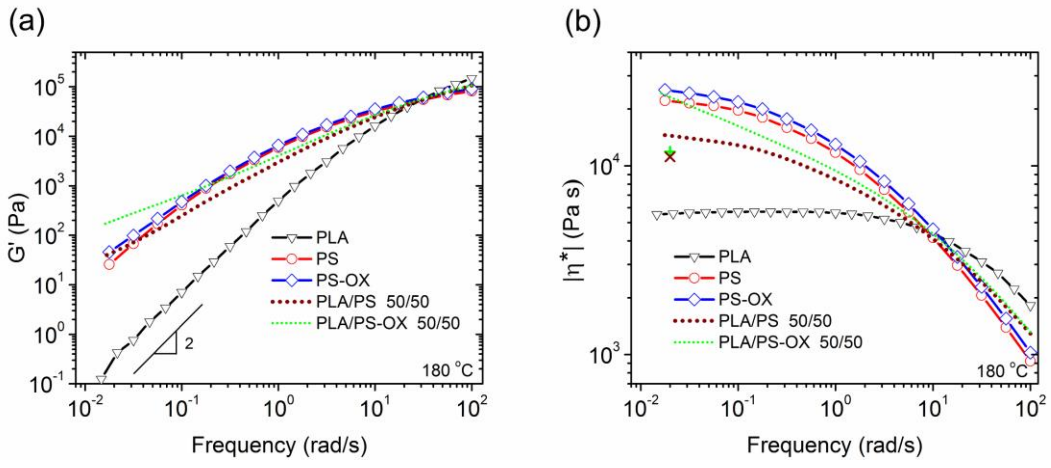

Figure 5-2 Elastic modulus and complex viscosity and of pure components and 50/50 vol.% blends. The

blends were mixed for 30 min. The two symbols at 0.2 s^{-1} are log-additive viscosity of PLA/PS (×) and PLA/PS-OX (+) blend. At low frequency, the log-additivity estimation is reasonable for the PLA/PS blend but not the compatibilized PLA/PS-OX blend. At high frequency, the log averages are in good agreement with the measured blend viscosities, see Figure A2-2 in Appendix A2.

The axial force (*F*) on the mixing chamber during blending, which is proportional to the melt pressure, was used to monitor the blend viscosity change.[144] Figure 5-3 shows the evolution of axial force of pure components and 50/50 vol.% blends. For the pure components, the axial force leveled off after the initial loading spike, indicating steady state. A slight decrease was observed for the PLA case, due to the degradation of PLA at high temperature. The mixing force of PLA (~3000 N) is higher than PS (~2000 N) at 200 rpm (estimated shear rate 85 s^{-1}). This corresponds well with Figure 5-2b which shows that above 10 s^{-1} shear rate, PLA is more viscous than PS. See Figure A2-3 for detailed correlation between mixing force *F* and viscosity.

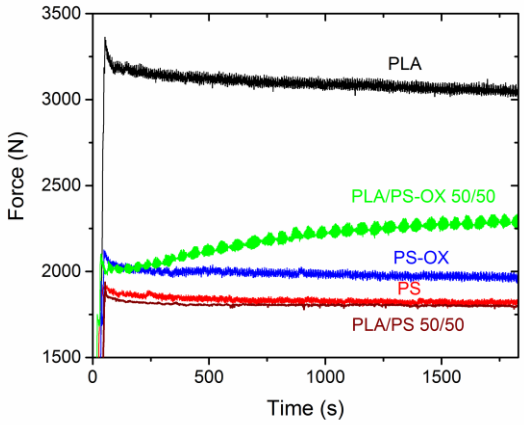

Figure 5-3 Mixing force as a function of mixing time for pure components and 50/50 vol.% blends. Mixing force is sensitive to polymer loading. Polymer loading was 4.0 mL based on melt density for all five.

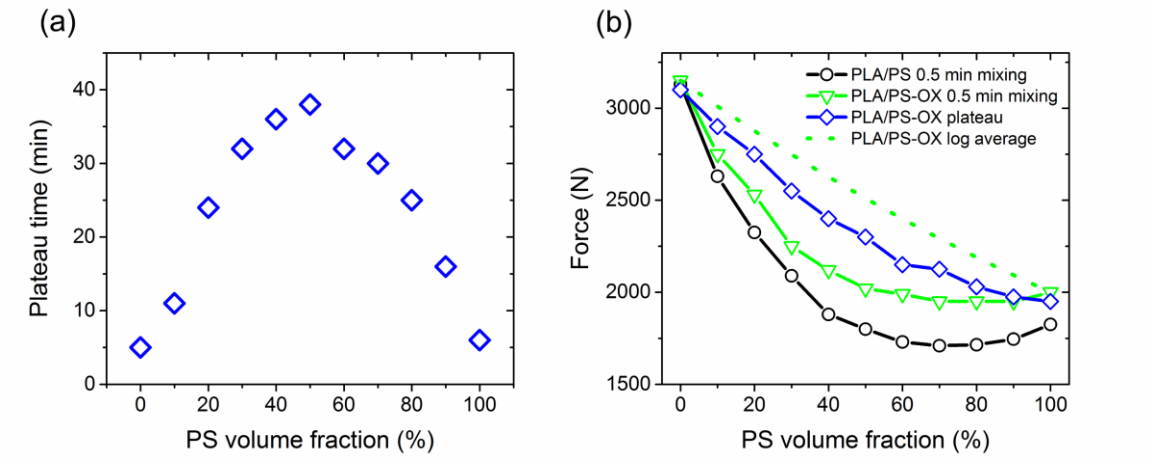

Figure 5-4 Mixing force and its plateau time. (a) Mixing time for mixing force to achieve plateau in PLA/PS-OX blends. See details in Figure A2-4. (b) Mixing force as a function of blend composition for PLA/PS and PLA/PS-OX blends. The dashed line represents the log-additive force of the two components.

For 50/50 vol.% PLA/PS blend, the plateau force was close to that of pure PS, regardless of PLA's higher mixing force. At the initial stage, 50/50 vol.% PLA/PS-OX had a mixing force close to PS-OX component. This indicated that the continuous low-viscosity PS phase was controlling the pressure in the mixing chamber. However, the normal force of PLA/PS-OX increased as mixing went on. This was due to the interfacial reaction between PLA and PS-OX. The reactively formed graft copolymer reduced interfacial slip which is related to the loss of entanglements at the interface[175, 176]. After ~38 min, a plateau force was reached, indicating equilibrium of the interfacial reaction. The mixing time to achieve normal force plateau is dependent on blend composition (Figure A2-4). A maximum was observed at 50/50 vol.% (Figure 5-4a).

Figure 5-4b shows mixing force as a function of blend composition. These values are compared to the log-additive force of PS and PLA. The log-additive mixing rule is a widely used semi-empirical rules for predicting blend viscosity[39, 177]. Both PLA/PS and PLA/PS-OX blends showed negative deviation from log-additivity. PLA/PS blends at > 40 vol.% PS even exhibited

lower mixing forces than the low-force component PS. From the gravimetric cocontinuity analysis discussed in the next section, we know that these compositions correspond to a continuous PS phase. This is strong evidence for interfacial slip at the interfaces between PS and PLA[175]. Before graft copolymer formation, the composition dependence of PLA/PS-OX mixing force was similar to the PLA/PS blends. However, at maximum copolymer conversion, deviation from log-additivity was much less because graft copolymer largely suppressed interfacial slip.

5.3.2 Effect of interfacial reaction on cocontinuity

Degree of PS continuity as a function of PS volume fraction, calculated by Equation 1, is shown in Figure 5-5. All blends were mixed for 6 minutes. PS continuity increased dramatically after a certain volume fraction, which marks the transition from droplet-matrix to cocontinuous morphology (Figure 5-6). At 80 vol.% PS, PLA/PS-OX blend disintegrated while PLA/PS retained its structure. The cocontinuity range was experimentally determined to be 40 – 80 vol.% PS for PLA/PS blend and 50 – 70 vol.% PS for PLA/PS-OX blend. In binary blends without any compatibilization, interfacial tension and viscosity are the main factors determining cocontinuity range. Low interfacial tension and high viscosity of both phases promote cocontinuity[40 - 43]. On the other hand, a number of studies[158, 178] have shown that premade di- or tri-block copolymers tend to narrow the cocontinuity range of immiscible polymer blends, which is attributed to its ability of suppressing droplet coalescence. In this work, reactively formed graft copolymer played a role comparable to premade block copolymers. Although PLA/PS-OX blends showed slightly higher viscosity (Figure 5-2b) they have a narrower cocontinuity range than PLA/PS blends.

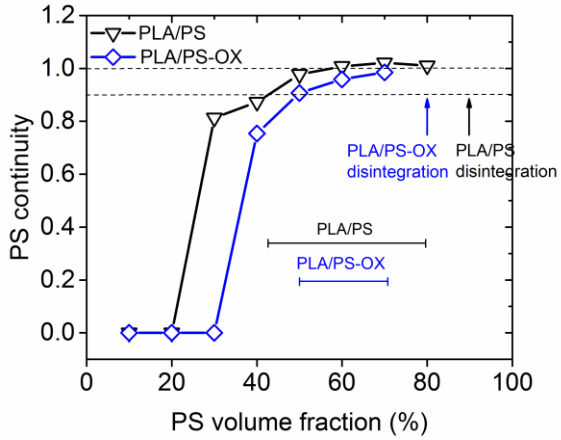

Figure 5-5 PS continuity as a function of PS volume fraction for PLA/PS and PLA/PS-OX blends. Blends were mixed for 6 min. All negative continuity points were set to zero. The horizontal bars mark the range of cocontinuous compositions. The arrows mark the volume fraction at sample disintegration.

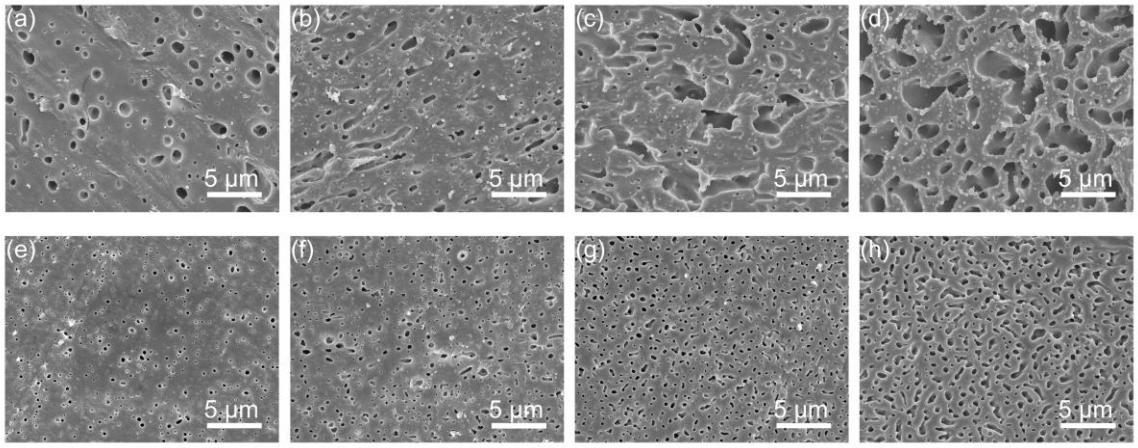

Figure 5-6 Continuity development of PS phase in PLA after 6 min mixing. Top: PLA/PS blends; bottom: PLA/PS-OX blends. From left to right: 90/10 vol.%, 80/20 vol.%, 70/30 vol.%, 60/40 vol.%. Cocontinuity formation is evident in (c) 30 vol.% PS for PLA/PS blends and (h) 40 vol.% PS-OX for PLA/PS-OX blends.

5.3.3 Effect of interfacial reaction on blend morphology and stability

To further study the effect of mixing time on blend morphology, blends of 50/50 vol.% PLA/PS and PLA/PS-OX were mixed for 6 min and 30 min respectively. Figures 6a and 6b show the morphology of PLA/PS blends (PS phase extracted). Characteristic pore size of 6 and 30 min

mixed blends are similar (a ~ 1.2 μm). This correlated with the mixing force evolution in Figure 5-3. After 6 min mixing, the blend reached steady state and further mixing did not change the morphology. However, for the PLA/PS-OX system (Figure 5-7c, d), phase size of 6 min mixed blend (a = 0.8 μm) is larger than that of 30 min mixed blend (a ~ 0.5 μm, see Figure A2-5 for higher magnification). As stated in Section 5.3.1, the interfacial reaction did not come to equilibrium until ~ 38 min mixing, so there was less graft copolymer in the 6 min mixed blend. Previous study on cocontinuous blends compatibilized by premade block copolymers also showed that lower copolymer loading resulted in larger characteristic phase size due to low interfacial copolymer coverage[179, 180].

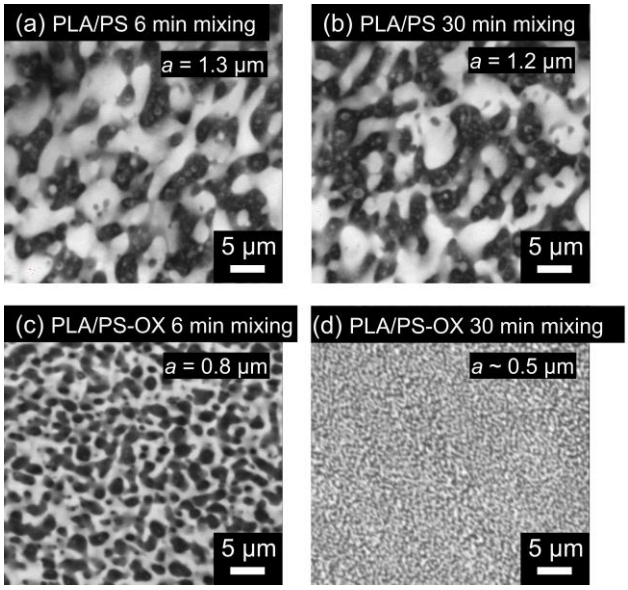

Figure 5-7 LSCM 2D images of porous PLA from blends quenched after extrusion. (a) PLA/PS 6 min mixing, (b) PLA/PS 30 min mixing, (c) PLA/PS-OX 6 min mixing, (d) PLA/PS-OX 30 min mixing. The dark regions are PLA and the bright regions are pores after removing PS. "a" is the characteristic pore size measured by Equation 5-2. See Figure A2-6 for 3D reconstructions.

In order to investigate stability, blends were subjected to static annealing at 180°C for up to 30 minutes. The 2D LSCM images in Figure 5-8 show morphology change during annealing.

Figure 5-9 summarizes the evolution of characteristic pore size as a function of annealing time. The coarsening rate was measured as slope of the linear fitting of characteristic size from 3 – 30 minutes. The size at 3 minutes of coarsening was used as the initial size to eliminate the effect of anisotropy induced by extrusion alignment. In an earlier work[74] (also Chapter 6) we pointed out that when viscosity ratio of two blend components is between 0.05 - 1, the coarsening rate of 50/50 vol.% cocontinuous blends can be estimated by Equation 5-4:

$$\frac{da}{dt} = c\frac{\Gamma}{\eta_{blend}} \tag{5-4}$$

where a is the characteristic phase size, Γ is the interfacial tension between the two phases ($\Gamma_{PS/PLA,\ 180\ °C}$ = 5.4 mN/m[181, 182]), and $log(\eta_{blend}) = \phi_1 log(\eta_1) + \phi_2 log(\eta_2)$, the log volume average of the zero shear viscosities of the blend components. The coefficient c is a universal coefficient around 0.03 (averaged from literature studies over a range of different blend pairs). The coarsening rate of PLA/PS blends (0.87 μm/min for 6 min mixed blend and 1.01 μm/min for 30 min mixed blend) here followed Equation 5-4 and gave a coarsening coefficient of 0.04, which is close to the universal value. Mixing time did not change the coarsening behavior of nonreactive blends. On the other hand, coarsening of PLA/PS-OX blends (0.12 μm/min for 6min mixed blend and 0.05 μm/min for 30 min mixed blend) is dependent on the mixing history. Longer mixing time resulted in lower coarsening rate. In an ideal case of cocontinuous blend compatibilized by symmetric diblock copolymer with high molecular weight, coarsening tends to increase the concentration of adsorbed copolymer at the interface, and thus reduce the interfacial tension[179]. In theory, this process can eventually drive the interfacial to zero and cease coarsening. However, the graft copolymer formed in this work is far from symmetric. It can reduce the interfacial tension but not to zero. So we don't expect the coarsening to stop even at longer annealing time.

The interfacial coverage in number of block copolymer molecules per interfacial area, Σ, is typically used to evaluate the compatibilization efficiency of block copolymers[161], and it is estimated by

$$\Sigma = \frac{w_{bcp}\rho_{bcp}N_{av}}{M_n}a \tag{5-5}$$

where w_{bcp} is the weight fraction of block copolymer in the blend, ρ_{bcp} is the density of block copolymer, N_{av} is Avogadro's number, and M_n is the number average molecular weight of the block copolymer. Considering a symmetric diblock PS-PLA copolymer, the maximum interfacial coverage Σ_{max} can be estimated by assuming the interface is a saturated lamellar monolayer of block copolymers. Based on work by Zalusky et. al and the scaling relation $\Sigma_{max} \sim M_n^{-1/3}$ [183], Σ_{max} = 0.14 chains/nm^2 for a 104k-115k (note the molecular weights in Table 5-1) PS-PLA diblock copolymer. The exact structure of graft copolymer in this study is unknown, but we can roughly estimate the conversion of the interfacial reaction based on the diblock case. Using a = 2 μm of PLA/PS-OX 30 min mixing blend at 30 min annealing, which has a more close-packed interface, and assuming $\Sigma = \Sigma_{max}$ = 0.14 chains/nm^2, Equation 5-5 gives w_{bcp} = 2.5%. This means conversion of the interfacial reaction is 2.5%. Literature reported adding 6 wt.% premade diblock PLA-PS into cocontinuous PLA/PS blend suppressed the coarsening[158]. It is reasonable that less reactively formed graft copolymer can achieve similar effect on reducing the coarsening rate since the graft copolymer is created at the interface, whereas some of the premade diblock is likely to remain in micelles in one of the phases.

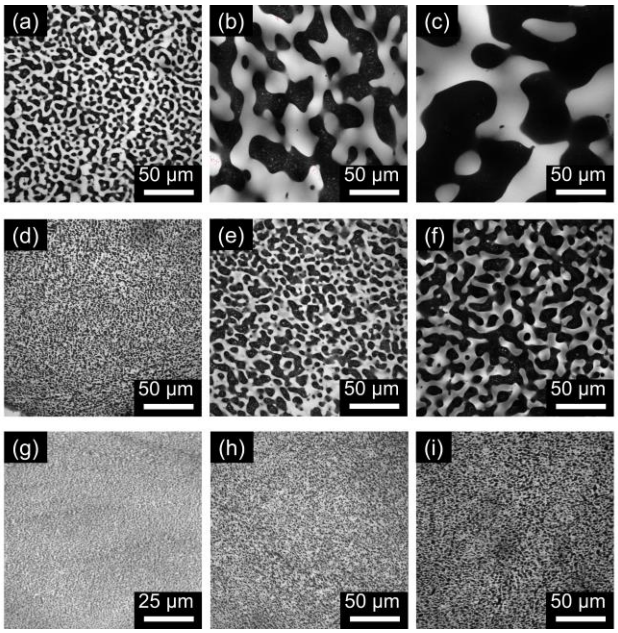

Figure 5-8 2D LSCM micrographs showing the morphology change of blends during annealing. (a) – (c): 6 min mixed PLA/PS, (d) – (f): 6 min mixed PLA/PS-OX, (g) – (i) 30 min mixed PLA/PS-OX. Micrographs on the left, middle, and right represent blends annealed for 3 min, 10 min, and 30 min, respectively.

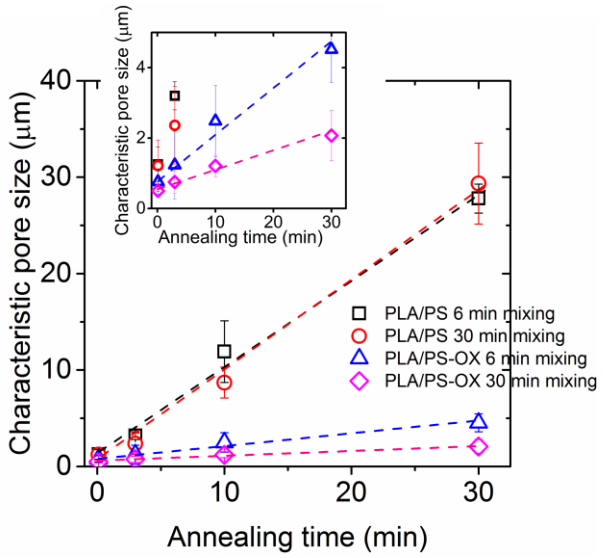

Figure 5-9 Characteristic pore size of PLA/PS and PLA/PS-OX blends as a function of annealing time at 180 °C. Lines are for eye guidance. The insert shows the small size region.

5.3.4 Hierarchically porous PLA from PLA/PS-OX/LLDPE blends

The fact that highly compatibilized PLA/PS-OX has submicron pore size made it possible to obtain hierarchically porous PLA by melt blending PLA/PS-OX with a third component that can generate larger pores. Figure 5-10c, d and Figure 5-12 show the morphology of porous PLA from a 30/30/40 vol.% PLA/PS-OX/LLDPE blend (mixed for 30 min) after extracting PS-OX and LLDPE phases by cyclohexane. The pores are clearly bimodally structured. In Figure 5-10c, the secondary pores formed by extraction of PS-OX are at least **one order of magnitude smaller** than the primary pores formed by extraction of LLDPE, ~ 0.5 μm (Figure 5-7d) vs ~ 5 μm (Figure 5-16).

It is worth mentioning that the nonreactive PLA/PS/LLDPE blend at 30/30/40 vol.% was also hierarchically structured (Figure 5-10a), with the secondary pores similar to Figure 5-7a. But this structure was not stable against annealing. The hierarchical feature disappeared after 10 min coarsening (Figure 5-10b). The SEM images in Figure 5-11 further confirmed the phase identification of Figure 5-10a. Here LLDPE was replaced by HDPE for easier imaging because HDPE is not soluble in cyclohexane at 50 °C. In the quenched blend, PE phase formed large domains while PLA/PS formed smaller size cocontinuous domains. Annealing drove all the PS to form a layer between PLA and PE and destroyed the secondary cocontinuous PLA/PS structure. In contrast, the PLA/PS-OX/LLDPE system preserved its hierarchical structure during annealing (Figure 5-10d, Figure A2-7).

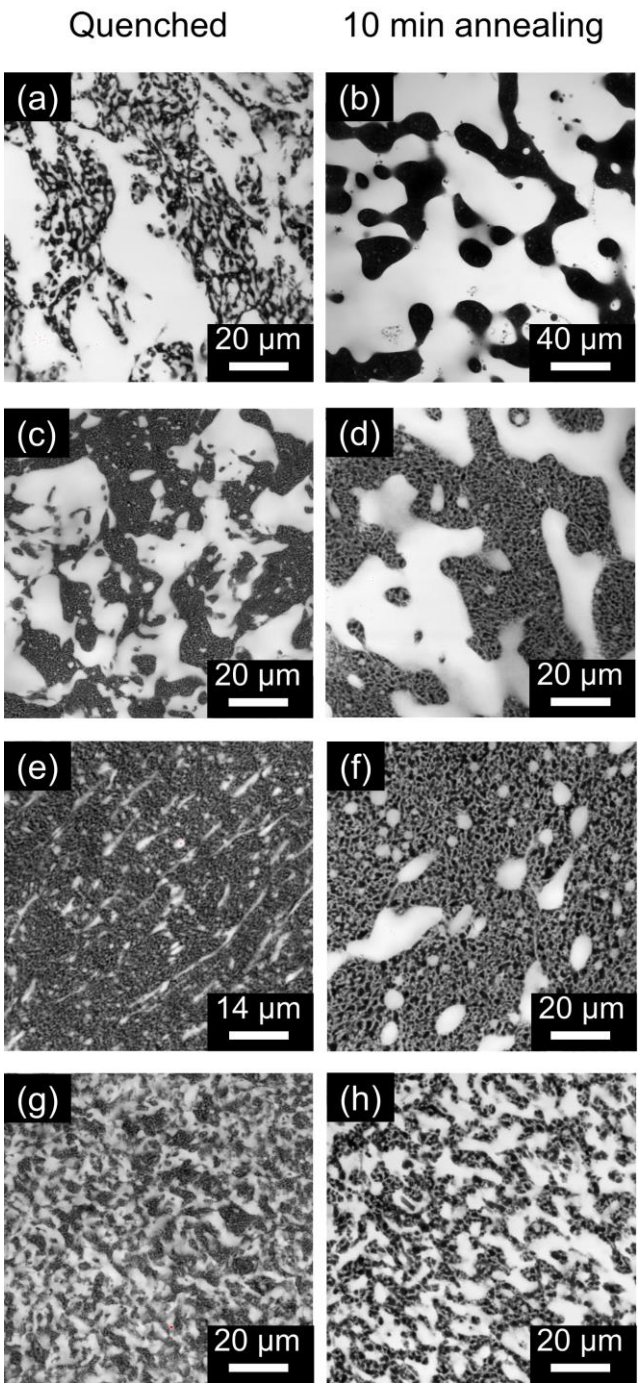

Figure 5-10 Morphology of porous PLA from ternary blends (mixed for 30 min). (a), (b): 30/30/40 vol.% PLA/PS/LLDPE; (c), (d): 30/30/40 vol.% PLA/PS-OX/LLDPE; (e), (f): 42.5/42.5/15 vol.% PLA/PS-OX/LLDPE; (g), (h): 30/30/40 vol.% PLA/PS-OX/LLDPE compatibilized with 3 wt.% SEBS. All micrographs on the left are quenched morphologies, on the right are morphologies after 10 min annealing.

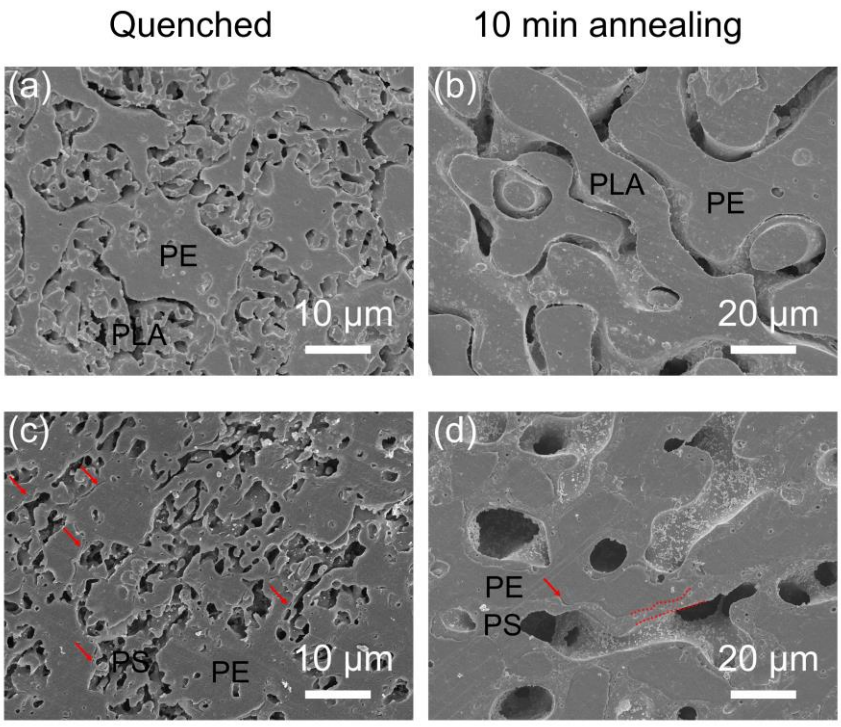

Figure 5-11 Phase identification in 30/30/40 vol.% PLA/PS/HDPE blends. In (a) and (b), PS was extracted with cyclohexane. In (c) and (d) PLA was removed with NaOH solution. The arrows in (c) and (d) mark the interfaces between PE and PS. The boundary between PE domain and (PLA/PS) domain in (c) is not as clear as (a) because, as discussed in the text, PE prefer PS to PLA.

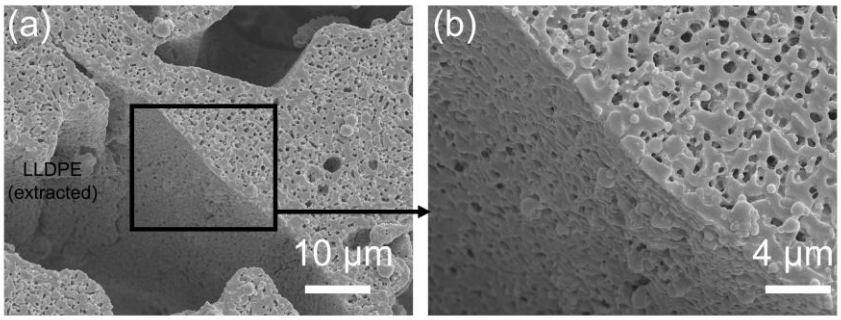

Figure 5-12 Porous PLA from a 30/30/40 vol.% PLA/PS-OX/LLDPE blend mixed for 30 min and then annealed for 3 min.

To better understand the formation of the hierarchical structures in Figure 5-10, thermodynamic interactions of PLA, PS, and PE were studied by examining their wetting behavior. Again for ease of SEM imaging, HDPE was used to replace LLDPE. The morphology of 45/10/45 vol.% HDPE/PS/PLA blend is presented in Figure 5-13. HDPE and PLA (two major phases) formed cocontinuous morphology with a PS (minor phase) layer separating them at the interface. This is a complete wetting morphology. The wetting behavior of ternary PE/PLA/PS blends can be described by the three spreading coefficients[184, 185], which were modified from Harkins equation[186, 187]:

$$\lambda_{PE-PS-PLA} = \Gamma_{PE-PLA} - \Gamma_{PE-PS} - \Gamma_{PLA-PS}$$

$$\lambda_{PLA-PE-PS} = \Gamma_{PLA-PS} - \Gamma_{PE-PS} - \Gamma_{PLA-PE}$$

$$\lambda_{PS-PLA-PE} = \Gamma_{PS-PE} - \Gamma_{PLA-PS} - \Gamma_{PLA-PE}$$

where the *Γ's* are the three interfacial tensions between any two of the three blend components. *λ's* describe the tendency of one component to separate the other two phases. For instance, $\lambda_{PE\text{-}PS\text{-}PLA}$ is a measure of the driving force for PS phase to spread at the interface of PE and PLA phase. The "complete wetting" of PS at PE/PLA interface requires $\lambda_{PE\text{-}PS\text{-}PLA} > 0$, $\lambda_{PLA\text{-}PE\text{-}PS} < 0$ and $\lambda_{PS\text{-}PLA\text{-}PE} < 0$. In other words, $\Gamma_{PE\text{-}PLA}$ is so high compared to $\Gamma_{PE\text{-}PS}$ and $\Gamma_{PLA\text{-}PS}$, that a PS layer separating PE/PLA is always thermodynamically favored to reduce the total interfacial energy of the system. Table 5-2 gives the literature-reported interfacial tensions. The calculated spreading coefficients agrees well with the statements above. In a ternary PLA/PS-OX/PE blend, the content of oxazoline functional group (1%) is very low so its effect on $\Gamma_{PS\text{-}PLA}$ *and* $\Gamma_{PS\text{-}PE}$ is negligible. After reaction of PS-OX with PLA, of course $\Gamma_{PS\text{-}PLA}$ drops due to copolymer formation, but it will not change the signs of the spreading coefficients. Thus the thermodynamic predictions for PLA/PS/PE blend still hold in PLA/PS-OX/PE blends. Figure 5-14 depicts the actual structure of a 30/30/40 vol.% PLA/PS-OX/LLDPE blend where the PLA/PS-OX cocontinuous structure is covered by a thin PS-

OX layer, rather than directly by the LLDPE phase. The primary cocontinuous structure resembles a 60/40 vol.% PS-OX/LLDPE blend, while the secondary cocontinuous structure is a 50/50 vol.% PLA/PS-OX blend. Figure 5-15 further confirmed the illustration in Figure 5-14.

Table 5-2 Interfacial tensions and spreading coefficients for PLA/PS/PE blend at 180 °C.

Polymer pair	Interfacial tension (mN/m)	Polymer sequence	Spreading coefficient (mN/m)
Γ_{PE-PLA}	11.0[74]	$\lambda_{PE-PS-PLA}$	0.5
Γ_{PE-PS}	5.1 [188 - 190]	$\lambda_{PLA-PE-PS}$	-10.7
Γ_{PLA-PS}	5.4[181]	$\lambda_{PS-PLA-PE}$	-11.3

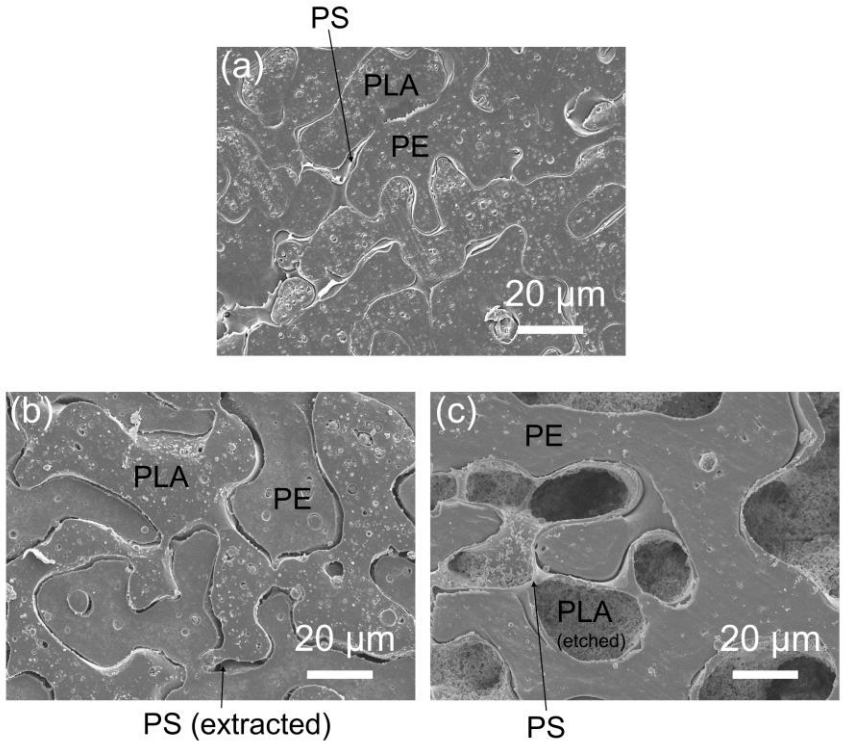

Figure 5-13 Morphology of 45/10/45 vol.% HDPE/PS/PLA blend after 10 min annealing at 180 °C. In (b) PS was removed by cyclohexane at 50 °C. In (c) PLA was etched out with NaOH solution. See Figure A2-8 for morphology of 45/10/45 vol.% HDPE/PS/PLA blends after 0, 3, 10 and 30 min annealing.

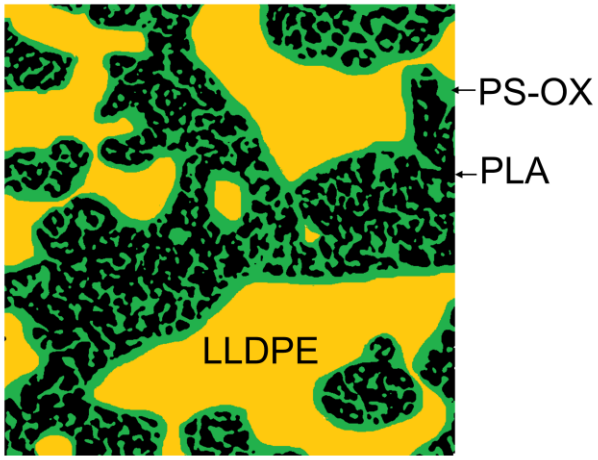

Figure 5-14 Illustration of the morphology of a "tri-continuous" blend, 30/30/40 vol.% PLA/PS-OX/LLDPE. The cocontinuous (PLA/PS-OX) domain is encapsulated by a layer of PS-OX.

Figure 5-10 also suggests some variation of the hierarchically porous morphology. The primary pore volume can be tuned by changing volume fraction of the LLDPE phase. In Figure 5-10e, f, when volume fraction was reduced to 15%, the LLDPE phase adopts dispersed droplet (or fiber) morphology. In the quenched sample, the LLDPE phase was elongated due to the flow field in the mixer. After annealing it became more like rounded droplets to minimize interfacial area with the PLA/PS-OX domain. Moreover, the primary pore size can be further adjusted by compatibilization of the LLDPE/PS-OX interface. Styrene-b-ethylene/butylene-b-styrene) tri-block copolymer (SEBS) is known to reduce PE/PS interfacial tension, leading to smaller characteristic phase size in cocontinuous PE/PS blend[191]. Figure 5-10g shows morphology of PLA/PS-OX/LLDPE 30/30/40 vol.% blend modified with 3 wt.% SEBS (Kraton1657). As expected, the primary pore size is smaller than Figure 5-10c, and the secondary pore size is close to Figure 5-10c. The above observations demonstrated reactive formed / premade copolymers as powerful tools to control pore structure of hierarchically porous PLA.

5.3.5 Coarsening behavior of "tri-continuous" ternary polymer blend

During quiescent annealing the 30/30/40 vol.% PLA/PS-OX/LLDPE blend (mixed for 30

min) retains the bimodal morphology evolution. Figure A2-7 showed that the coarsening of secondary pores is similar to that in binary PLA/PS-OX blend (mixed for 30 min).

The other significant feature is the coarsening of the LLDPE domain, which defines the primary pores. For the sake of easier image analysis, LLDPE was replaced by HDPE to study its coarsening. Since their zero shear rate viscosities (Table 5-1) and interfacial tensions are very similar coarsening behavior should be the same. Figure 5-15 compares the morphology of 30/30/40 vol.% PLA/PS-OX/HDPE and 60/40 vol.% PS-OX/HDPE during annealing. SEM image analysis results in Figure 5-16 shows HDPE domain sizes are similar in the ternary and binary blends. This is not surprising considering Equation 5-4. First, 30/30/40 vol.% PLA/PS-OX/HDPE and 60/40 vol.% PS-OX/HDPE has the same HDPE/PS-OX interface. They share the same driving force, $\Gamma_{PE\text{-}PS}$, for the coarsening of HDPE domains. Second, Figure 5-2b showed that the zero viscosities of PS-OX and 50/50 vol.% PLA/PS-OX blend were close, ~ 30 kPa s. Thus 30/30/40 vol.% PLA/PS-OX/HDPE and 60/40 vol.% PS-OX/HDPE blends have similar η_{blend} 's. The secondary cocontinuous (PLA/PS-OX) structure of the ternary blend had no extra effect on the initial domain size or coarsening behavior of the HDPE phase.

In contrast to these results, Wang et. al[153] reported reduced primary phase size and coarsening rate in a 25/25/50 vol.% HDPE/SEBS/PLA blend, compared to its corresponding binary 50/50 vol.% HDPE/PLA blend. The authors attributed the reduced primary coarsening rate to: (i) the finely dispersed, low interfacial tension secondary HDPE/SEBS cocontinuous structure has a cascade effect on the coarsening of PLA domains; (ii) the high viscosity or even physical crosslinks of SEBS copolymer slowed down coarsening of the primary (HDPE/SEBS) and PLA domains. However, our results suggest the cascade effect is unlikely. In addition, we speculate there was no direct contact of PLA with HDPE in the HDPE/SEBS/PLA blend because PLA will be preferentially covered by the microphase-separated PS domains in the SEBS phase. Consequently,

the PLA/SEBS interfacial tension served as the driving force for coarsening of the primary phases, which is not as high as that in PLA/HDPE binary blend. In conclusion, both this study and the HDPE/SEBS/PLA hierarchical blend by Wang et. al indicate that viscosity (or yield stress) and interfacial tension are still the two main factors determining coarsening behavior of hierarchical ternary blends. If none of the blend components exhibit a yield stress and no interfacial modifier is used, the coarsening rate of the primary cocontinuous structure in "tri-continuous" ternary blend should still follow Equation 5-4, which is derived from binary blends.

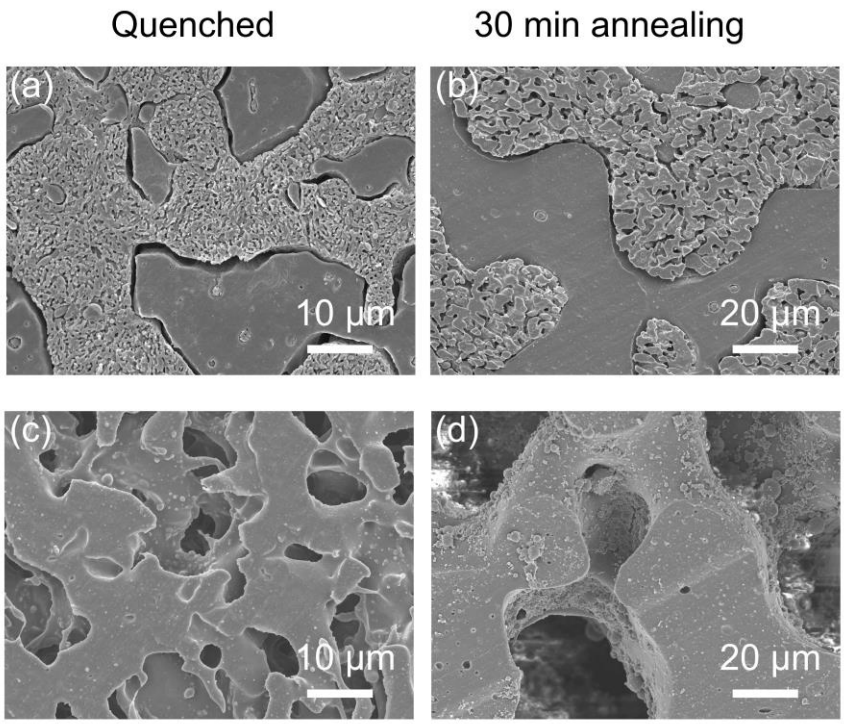

Figure 5-15 Coarsening behavior of 30/30/40 vol.% PLA/PS-OX/HDPE and 60/40 vol.% PS-OX/HDPE. (a), (b) PLA/PS-OX/HDPE; (c), (d) PS-OX/HDPE. (a), (c) quenched; (b), (d) annealed for 30 min. PS-OX phase was removed by cyclohexane.

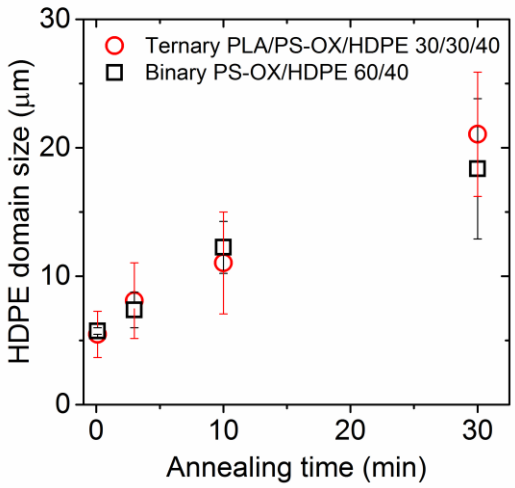

Figure 5-16 Characteristic size of HDPE domains (from SEM image analysis) for "tri-continuous" PLA/PS-OX/HDPE 30/30/40 vol.% blend and cocontinuous PS-OX/HDPE 60/40 vol.% blend as a function of annealing time at 180 °C.

5.4 Conclusions

This work demonstrated the preparation of hierarchically porous PLA from reactively compatibilized "tri-continuous" PLA/PS-OX/LLDPE blends. The reaction between oxazoline functional groups in PS-OX and PLA is vital for the development of hierarchical structure in PLA/PS-OX/LLDPE blends because it can generate submicron-sized PLA domains by forming graft copolymer at the PS-OX/PLA interface. Selective extraction of PS-OX and LLDPE from the ternary blend led to submicron small pores and large pores of 5 – 20 μm. Thermal annealing and composition variation were adopted to control the pore size and pore morphology. This strategy of making hierarchically porous PLA has potential applications as tissue scaffolds and it may be applied to other polymers containing carboxylic acid end groups, such as poly(glycolic acid) (PGA), polycaprolactone (PCL), and nylon.

The study on binary PLA/PS blend demonstrates that mixing force, or torque, during melt blending can be used to evaluate interfacial slip of immiscible polymer blends. Interfacial reaction

between PS-OX and PLA suppressed interfacial slip and the increase in mixing force was an effective measure of reaction rate. It was also found that the reactively formed PLA-PS graft copolymer narrowed the cocontinuity range of PLA/PS-OX blend.

Ternary PLA/PS/PE blends demonstrated complete wetting behavior with a PS layer located at the interface between PLA and PE. It was confirmed that the PLA/PE interfacial tension is much higher than PLA/PS interfacial tension. Static annealing experiments revealed that the "tri-continuous" ternary blend had similar coarsening behavior to cocontinuous binary blends.

Chapter 6 Cocontinuous PLA/PE blends: effect of extensional viscosity on blend cocontinuity*

6.1 Background

As introduced in Chapter 1, most immiscible polymer blends form cocontinuous morphologies over a range of compositions, defined as cocontinuity range. The available literature on immiscible polymer blends has explored predictions of cocontinuity based on a phase inversion point. These models have been limited to predictions based on shear rheological properties. However, it is well known that melt processing flows in a device like a twin-screw extruder are complex and cannot be modeled as simple shear flow. Extensional flows factor heavily in real mixing processes. As shown in Chapter 2, the extensional rheological properties of a material can deviate dramatically from their shear flow counterparts, especially in the case of long chain branched (LCB) polymers. The present study aims to determine the role that extensional viscosity plays in determining cocontinuous compositions, blend stability, and the size scale of the phase domains, in order to control cocontinuous morphologies and enable better product design. To achieve this, LCB polymers are used to independently control shear and extensional rheological properties, and investigate the effect of LCB on blend size, stability, and the ability to form a cocontinuous microstructure.

Blends were prepared from linear and branched versions of PE and PLA. Effort was made to select materials for which LCB would modify the extensional viscosity but only minimally influence the shear rheological behavior at shear rates typically observed in melt processing flows (>10 s^{-1}). Materials were characterized rheologically in shear using small amplitude oscillatory shear and capillary rheometry. Extensional flow properties were characterized using both EVF

* Reproduced in part from "A.T. Hedegaard, L. Gu, C.W. Macosko, J. Rheol. 59 (2015) 1397–1417". Financial support for this work came from the IPRIME program of the University of Minnesota.

extensional rheometry and Cogswell's analysis of entrance pressure drop from capillary rheometry [192 - 194]. Blend morphology was analyzed gravimetrically via solvent extraction of the PLA phase, and imaged by scanning electron microscopy (SEM) and laser scanning confocal microscopy (LSCM), the latter of which was used to generate 3D reconstructions of the cocontinuous microstructure for characteristic size analysis. The dependence of blend stability on long chain branching was investigated by using LSCM to measure characteristic size as a function of quiescent annealing time.

6.2 Experimental

6.2.1 Materials

For the present study, two polyethylene resins supplied by the Dow Chemical Company were used: linear high-density polyethylene (HDPE, Dow 4452N), and branched low-density polyethylene (LDPE, Dow 955I). Two PLA resins were used: a linear PLA (L-PLA, Natureworks Ingeo™ 2003D), and a branched PLA (B-PLA) derived from L-PLA via free radical chemistry, performed by Interfacial Solutions, LLC (deTerra® IP 1406-1)[73].

Table 6-1 Melting temperature, molecular weight, and density for PE and PLA materials.

Material	T_m (°C)	M_n (kg/mol)	M_w (kg/mol)	ρ (g/cm^3) @ 23 °C[a]
LDPE	105	12	59	0.92
HDPE	120	18	90	0.954
L-PLA	165	125	228	1.24
B-PLA	165	94	366	1.18

[a]The polymer densities are provided by suppliers.

The relevant material properties are shown in Table 6-1. Melting temperature, T_m, was measured by dynamic scanning calorimetry (DSC, TA Instruments Q1000). Molecular weight of the PE was measured by high temperature gel permeation chromatography (GPC, Agilent PL-GPC 220 High Temperature GPC/SEC System) at 155 °C using 1,2,4-trichlorobenzene as the eluent.

Molecular weight of PLA samples were characterized by GPC in chloroform at 35 °C (Hewlett-Packard 1100 series chromatograph equipped with three PLgel 5 μm MIXED-C columns and a Hewlett-Packard 1047A refractive index detector). The GPC values reported are based upon polystyrene standards. Density values were provided by the material suppliers.

A third PLA sample (henceforth referred to as mixed PLA or M-PLA) was produced with an intermediate amount of LCB by blending together linear and branched PLA at 75/25 wt% L-PLA/B-PLA, using a lab-scale 16-mm co-rotating twin screw extruder (PRISM Model CS/16-V2) at 180 °C. L-PLA and B-PLA were fed into the extruder at a rate of 500 g/hr, with a screw speed of 50 RPM. The product was extruded from a circular die, cooled in a recirculating water trough, and pelletized. For 3D imaging of the blends in laser scanning confocal microscopy (LSCM), 2-hydroxyethyl(methacrylate) (HEMA), azobisisobutyronitrile (AIBN), and Rhodamine B fluorescent dye were purchased from Aldrich and used as received.

6.2.2 Small amplitude oscillatory shear (SAOS)

The linear viscoelastic properties under shear flow of all pure materials were measured via SAOS on an ARES rheometer (TA Instruments) at 180 °C, using 25-mm parallel plates. Strain sweep tests were conducted on all materials at a frequency of 1 rad/s to determine the critical strain at which materials exhibited non-linear behavior, which was approximately 20% strain for all investigated materials. Frequency sweeps over a range of 100 – 0.01 rad/s were then conducted using strains below the measured critical strain.

6.2.3 Capillary rheometry

All materials were measured via capillary rheometry using a 15-mm diameter twin-bore capillary rheometer (Rosand RH-7, Malvern Instruments) in order to characterize the shear and extensional rheological properties at higher deformation rates. Pressure drop as a function of piston speed was measured independently in both barrels. In one barrel, pressure drop was measured across a capillary die with 16 mm length, 1 mm diameter, and 180° entrance angle, using a 10,000

psi pressure transducer. In the other barrel, the same material was run and pressure drop was measured across a 0.25 mm length, 1 mm diameter, and 180° entrance angle capillary die, using a 1,500 psi pressure transducer. Entrance pressure and capillary pressure were calculated treating the 0.25 mm length die as an effective zero-length die. The true shear rate in the die was calculated by applying the Rabinowitsch correction to account for non-Newtonian flow behavior of the material, and the shear viscosity was calculated from the capillary pressure drop. The extensional viscosity and an estimated extensional rate were calculated based on the entrance pressure drop, following Cogswell's analysis[192 - 194].

6.2.4 Extensional viscosity

Extensional viscosity of the PLA materials was measured on an ARES-G2 rheometer using the extensional viscosity fixture (EVF, TA Instruments). Rectangular samples with dimensions 25×5×1 mm were prepared via compression molding (Carver, Inc., Wabash, Indiana) at 180 °C and 2 tons of force. Materials were tested by clipping a rectangular bar onto the two posts of the fixture, then closing the oven to heat the sample to 180 °C. The sample was annealed at 180 °C for 20 seconds to allow the temperature to equilibrate. Following annealing, a pre-stretch was applied to a Hencky strain of 0.035 at a strain rate of 0.01 s^{-1} to ensure that the sample was adhered tightly to the posts prior to extension. Any residual stress from the pre-stretch was allowed to relax by annealing for another 20 seconds. The sample was then stretched at strain rates between 0.1 and 10 s^{-1} to a total Hencky strain of 5. Due to the design of the fixture, the material began to overlap at a Hencky strain of around 3, and so extensional viscosity data at Hencky strain between 0 and 3 was reported.

To compare the extensional response to the linear viscoelastic limit, the pure materials were also tested in start-up of steady shear at a shear rate of 0.1 s^{-1} for all materials except B-PLA, which was measured at 0.01 s^{-1} instead due to excessive torque on the rheometer at higher rates, on an ARES rheometer using a 25 mm cone and plate with an angle of 0.1. The measured shear viscosity

from these tests was multiplied by 3, based on Trouton's ratio of $\eta_u = 3\eta$, to predict the linear viscoelastic limit of the materials under extensional flow.

The extensional viscosity of the PE materials was not measured in this way due to their lower melting point and zero-shear viscosity, which resulted in sagging during the pre-stretch annealing. This compromised the accuracy of these results, and so extensional viscosity of the PE materials will only be reported as measured by entrance pressure drop in capillary rheometry.

6.2.5 Blending experiments

Blends of PE and PLA were prepared using a recirculating, conical twin-screw batch microcompounder (DACA Instruments) with a mixing volume of 5 cm^3. All blends were prepared at 180 °C with a rotation speed of 200 RPM, which generates a maximum shear rate of approximately 400 s^{-1}.[134] After 6 minutes of mixing, the recirculation channel was opened to extrude the product from a circular die. The residence time in the die is ~ 20 s. After the blend exited the die, it was quenched in liquid nitrogen to freeze the morphology. Blends were produced across compositions ranging from 10/90 wt% PE/PLA to 90/10 wt% PE/PLA.

6.2.6 Determination of cocontinuity

The extruded blends were soaked in chloroform for 48 hours in order to dissolve all continuously connected regions of PLA that contacted the outside surface of the extrudate. The degree of PLA continuity, Φ_{PLA}, a measure of the fraction of PLA in the blend that is continuously connected, was measured gravimetrically[173]:

$$\Phi_{PLA} = \frac{m_i - m_f}{m_{PLA,i}} \tag{6-1}$$

where m_i is the initial mass of the blend (typically 0.2 g), m_f is the final mass following extraction in chloroform, and $m_{PLA,i}$ is the initial mass of the PLA in the blend. A degree of PLA continuity of 1 was indicative of a completely continuous PLA phase, whereas a degree of continuity

approaching zero was indicative of a PLA phase composed of dispersed droplets. For the purposes of this study, $\Phi_{PLA} \geq 0.9$ was treated as a fully continuous PLA phase. Polyethylene continuity was determined by the ability of the blend to remain self-supporting after PLA extraction. A blend that collapsed following the chloroform wash indicated a discontinuous PE phase. Therefore, a cocontinuous blend was defined as one with $\Phi_{PLA} \geq 0.9$ which remained self-supporting following the chloroform wash. The range of cocontinuity of a material system was defined as the range of compositions that displayed these properties.

6.2.7 Coarsening

In order to determine blend stability, cocontinuous blends from each material system were compressed to 4 mm thick at 180 °C on a compression press (Carver, Inc., Wabash, Indiana) then annealed with no applied pressure for between 1 and 30 minutes. Upon completion of annealing, the samples were immediately transferred to a separate chilled compression press for rapid cooling to freeze the final morphology.

6.2.8 Scanning electron microscopy

Cross-sections normal to the extrusion direction of the blends were imaged by scanning electron microscopy (SEM, JEOL 6500). Prior to imaging, smooth cross-sections of the blends were prepared by cryo-microtome (Reichert UltraCut S Ultramicrotome) at -140 °C using a diamond knife. Blends were then soaked in chloroform for 48 hours to extract the PLA from the surface of the blend, leaving behind a PE matrix. Each PE matrix was dried in a vacuum oven overnight and then sputter coated with 50 Å of platinum to create a conductive surface, and then was imaged at an accelerating voltage of 5 kV and a working distance of 10 mm.

6.2.9 Laser scanning confocal microscopy

For the purposes of characteristic size analysis, cocontinuous blends were imaged in 3D using laser scanning confocal microscopy (LSCM, Olympus Fluo View 1000). In order to image

blends by LSCM, they need to be optically transparent to allow the laser to penetrate to the interior of the sample and have fluorescent contrast between the phases. The PE/PLA blends were not optically transparent, due to a difference between the refractive index of each component, and were not fluorescent. In order to generate optically clear samples, thin slices (~100 μm thick) were prepared with a razor blade and then soaked in chloroform overnight to extract the continuous PLA. The slices were placed between a glass slide and coverslip. This space was filled by pipette with 2-hydroxyethyl(methacrylate) (HEMA) containing 0.01wt% Rhodamine B fluorescent dye and 1 wt% azobisisobutyronitrile (AIBN) radical initiator, allowing the HEMA to fill the pores of the PE slice. The slides were then placed in an oven at 80 °C for 10-15 minutes, which polymerized the HEMA. The refractive index of the polymerized HEMA matched that of PE and the sample appeared optically transparent, with the fluorescent HEMA replacing the extracted PLA phase in the imaging. It should be noted that due to the requirement of PLA extraction prior to imaging, this technique could only be used for cocontinuous samples and not for blends consisting of dispersed droplets.

A series of 2D images were taken at different focal depths through the sample. Using Avizo (v. 6.3, http://www.vsg3d.com/avizo), these images were binarized so that black represented non-fluorescent PE and white the fluorescent HEMA (indicative of the continuous PLA domains). These formed a stack of binary images, from which a 3D reconstruction of the structure was generated. A triangular mesh was applied along the PE-HEMA interface using a marching cubes algorithm included in the Avizo software package. From these 3D images, a characteristic size of the blends could be calculated[174]:

$$a = V \Big/ \sum_{i=1}^{N} A_i \tag{6-2}$$

where a is the characteristic pore size of the cocontinuous blend, V is the total volume of the

analyzed sample, and A_i is the area of a single triangle of the interfacial triangular mesh.

6.3 Results

6.3.1 Rheology

Figure 6-1 shows the results of shear viscosity collected by both SAOS and capillary rheometry. Closed symbols show complex viscosity versus oscillatory frequency in a range of 0.01 – 100 s^{-1} collected from SAOS. Open symbols show shear viscosity versus the Rabinowitsch-corrected shear rate as collected by capillary rheometry. The overlapping data from SAOS and capillary rheometry in the range of 10-100 s^{-1} shows good agreement between the two methods, confirming Cox-Merz rule[1]. The solid lines show the Cross model fit to the combined data for each material. The Cross model coefficients are shown in Table 6-2.

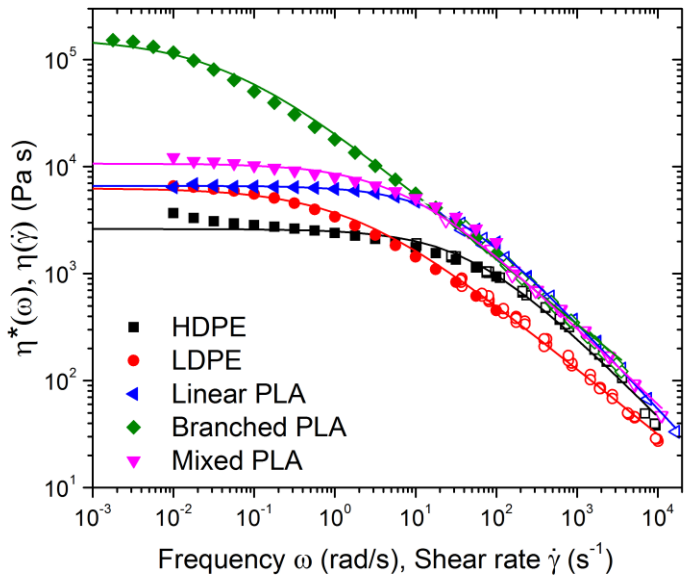

Figure 6-1 Shear viscosity of PE and PLA materials at 180 °C. Closed symbols for shear rates 0.01 – 100 s^{-1} are complex viscosity $\eta^*(\omega)$ collected by parallel plate SAOS rheology. Open symbols are $\eta(\dot{\gamma})$ collected by capillary rheometry. Lines show Cross model fits, using the parameters shown in Table 6-2.

Table 6-2 Cross model parameters, shear viscosity, extensional viscosity and Trouton ratio for PE and PLA materials at 180 °C.

Material	η_o (kPa s)	n	K (s)	η @ 400 s^{-1} (Pa s)	η_u @ 200 s^{-1} (Pa s)	X_e @ 200 s^{-1} [a]
HDPE	2.61	0.244	0.0204	444	4660	2
LDPE	6.30	0.387	0.560	220	9485	9
L-PLA	6.62	0.189	0.0369	671	8480	2
M-PLA	10.7	0.283	0.136	589	11350	4
B-PLA	158	0.390	23.56	589	21000	8

[a] X_e estimated from Figure 6-4.

Figure 6-2 shows the transient extensional viscosity of the PLA materials at extension rates between 0.1 and 10 s^{-1}, measured by EVF. As mentioned in the experimental methods, EVF results for PE materials are not reported here, due to their tendency to sag when attached to the fixture. The figure also shows the linear viscoelastic limit (LVE) of the transient response of each material under extension, given as 3 times the time-dependent shear viscosity, measured in start-up of steady shear experiments. Figure 6-3 shows the extensional viscosity measured by capillary rheometry and estimated using Cogswell's analysis.

Figure 6-4 shows the Trouton ratio, X_e, a measure of the degree of strain hardening, given by:

$$X_e\left(\dot{\varepsilon}\right) = \frac{\eta_u\left(\dot{\varepsilon}\right)}{3\eta\left(\dot{\gamma}\right)} \text{ when } \dot{\varepsilon} = \dot{\gamma} \tag{6-3}$$

In the case of a Newtonian fluid that shows no strain hardening, $X_e = 1$. The closed symbols at low extension rate are calculated from EVF for PLA. The open symbols at high extension rate are calculated from capillary rheometry. Table 6-2 gives X_e values at an extension and shear rate of 200 s^{-1}. Since measurements of extensional viscosity by EVF are transient and, particularly for the strain hardening materials, did not reach a steady state extensional viscosity before sample overlap or breakage, $\eta_u\left(\dot{\varepsilon}\right)$ was evaluated at a Hencky strain of 2.7.

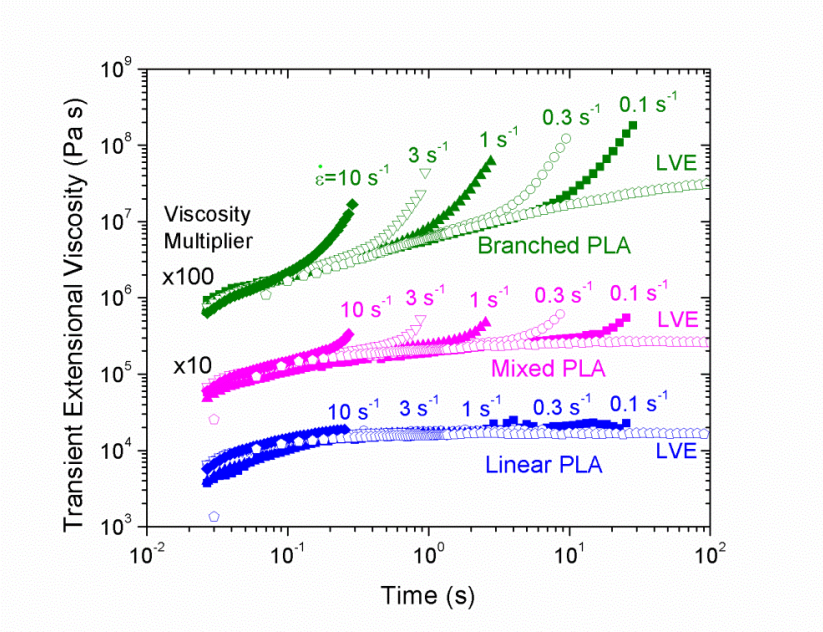

Figure 6-2 Transient extensional viscosity of PLA, as measured by EVF. The LVE limit is three times the transient shear viscosity, measured by 25-mm cone and plate. The data have been vertically offset by the reported viscosity multipliers for clarity.

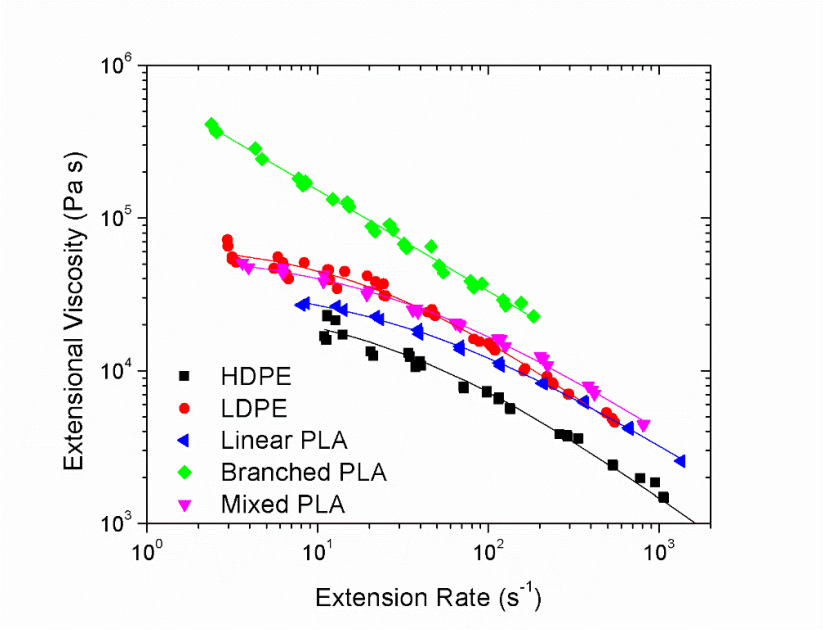

Figure 6-3 Extensional viscosity of PE and PLA materials, as measured by Cogswell's analysis for entrance pressure drop in capillary rheometry. The lines are to guide the eye.

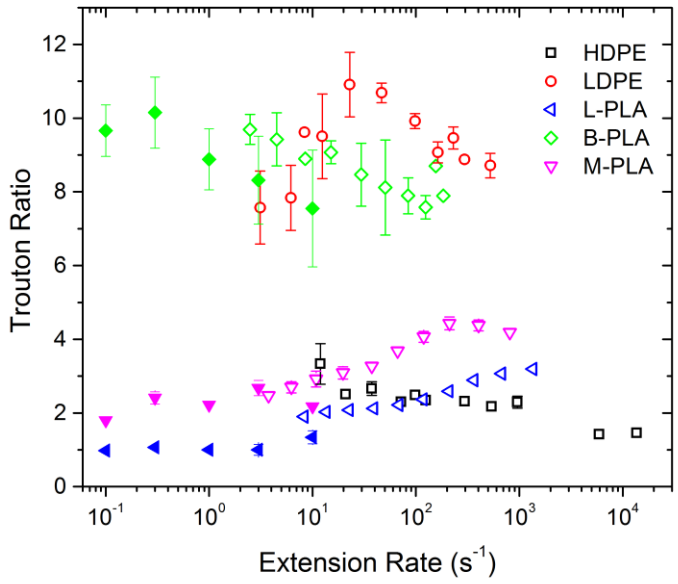

Figure 6-4 Trouton ratio, X_e. Closed symbols are for PLA materials as measured by EVF, with extensional viscosity evaluated at a Hencky strain of 2.7, and steady state shear viscosity evaluated from SAOS measurements. Open symbols at high extension rates are calculated from capillary rheometry.

From Figure 6-1 through Figure 6-3, a number of conclusions can be drawn concerning the various materials studied. First, from Figure 6-1, the presence of long-chain branching in the mixed and branched PLA shows a strong influence on the shear rheology of the material, but only at shear rates less than 10 s^{-1}. A higher degree of branching in the PLA was observed to increase the zero-shear viscosity and the time constant K, so that materials with a higher degree of branching showed an onset of shear thinning behavior at lower shear rates. However, at shear rates greater than 10 s^{-1}, the shear viscosities of the PLA materials were nearly indistinguishable. This suggests that during higher shear rate mixing such as that used in the blending conditions for the present study, long chain branching does not significantly influence the shear flow behavior. This behavior is consistent with results reported previously[101, 195, 196]. The shear viscosity of the PE materials follows a similar trend. Between HDPE and LDPE, the shear viscosity at high shear rates does not match

as consistently as was observed among the PLA materials, but the branched LDPE does show a higher zero-shear viscosity, while the viscosity at shear rates greater than 10 s^{-1} is lower than that of HDPE. The better viscosity match at high shear rate of all PLA materials may be due to the fact that they were derived from the same base material (L-PLA). This was not the case for the two PEs. To emphasize the most critical observation, when processing these materials (particularly the PLA) under conditions of shear rate >10 s^{-1}, the shear rheological response of these materials is very similar, and so differences between the blends are likely due to differences in extensional viscosity.

From Figure 6-4, it is observed that B-PLA and LDPE showed the strongest strain hardening response at all rates, with Trouton ratios around 9. Mixed PLA showed slight strain hardening behavior compared to the linear polymers. This strain hardening behavior is roughly independent of extension rate (within experimental error), such that the branched materials show higher extensional viscosity than their linear counterparts at all rates. This suggests that LCB, while only influencing shear viscosity at low rates, increases the extensional viscosity at all measured rates and that a higher degree of branching amplified this effect. According to EVF measurements, L-PLA showed no strain hardening behavior, while capillary rheometry gave a strain hardening factor of 2. This difference may be attributed to the different nature of the experiments – capillary rheometry is an indirect measure of extensional viscosity, a mixture of shear and extension, while EVF is a transient and direct measurement of η_u by uniaxial extension. However, the consistency of X_e for B-PLA and M-PLA when measured both by EVF and capillary rheometry suggests that extensional viscosity calculated by Cogswell's analysis relates to a Hencky strain of approximately 2.7. This observation is consistent with previous results by Padmanabhan and Macosko[197].

6.3.2 Range of cocontinuity

Figure 6-5 shows the degree of PLA continuity, as calculated by Equation 6-1, as a function of PLA volume fraction. All samples were quenched immediately after extrusion from the mixer

die. The symbols give the measure of PLA continuity, while the ranges shown at the bottom of the figure indicate all compositions that met the criteria of cocontinuity, $\Phi_{PLA} \geq 0.9$ and a self-supporting PE phase following extraction in chloroform, for each material system.

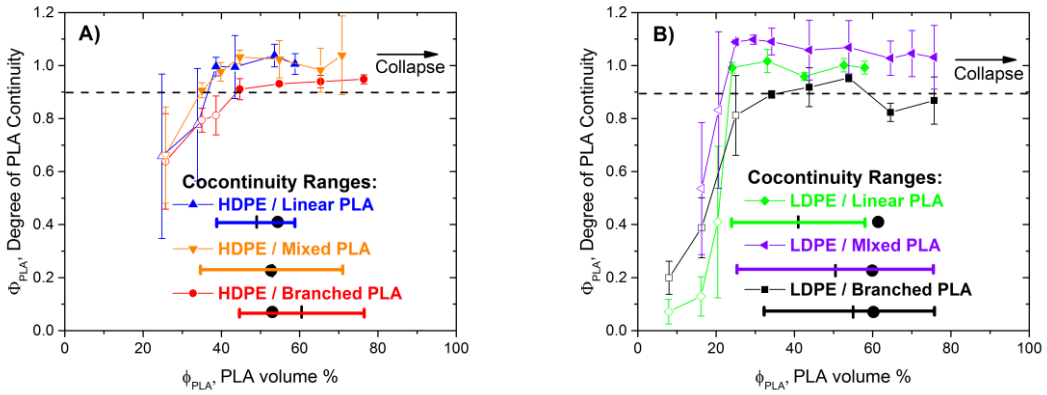

Figure 6-5 Degree of cocontinuity and range of cocontinuity. For the degree of cocontinuity data, the closed symbols represent fully cocontinuous blends. Open symbols are not completely cocontinuous, in which PLA exists in dispersed droplets. The horizontal bars mark the range of cocontinuous compositions. Along the ranges, the closed circles show the phase inversion composition as predicted by Equation 6-4, while a vertical bar marks the center of the experimental cocontinuity range.

The filled black circles along the ranges show the predicted phase inversion point, which is expected to coincide with the center of the range of cocontinuity. It is given by the following model by Utracki, derived from the packing of viscoelastic spheres to create a continuous network[39]:

$$\frac{\eta_{PE}(\dot{\gamma})}{\eta_{PLA}(\dot{\gamma})} = \left[\frac{\phi_m - \phi_{PLA,PI}}{\phi_m - (1-\phi_{PLA,PI})}\right]^{[\eta]\phi_m} \tag{6-4}$$

where $\eta_{PE}(\dot{\gamma})$ and $\eta_{PLA}(\dot{\gamma})$ are shear viscosity of the PE and PLA, respectively, at the shear rate of mixing, $\phi_{PLA,PI}$ is the predicted phase inversion volume fraction for the PLA phase, and ϕ_m is the

maximum packing fraction of deformable spheres and $[\eta]$ is the intrinsic viscosity of deformable viscoelastic spheres. Values of $[\eta]$=1.9 and ϕ_m=0.84 were used. These were empirically derived in previous studies when the viscosity ratio was near unity[39].

Table 6-3 tabulates results for the range of cocontinuity, as well as the experimentally observed center of the range of cocontinuity, the predicted center by Equation 6-4, and the deviation between the experimental and predicted values.

Table 6-3 Upper and lower bound of PLA volume % for the range of cocontinuity, with a comparison of the experimentally observed center of cocontinuity range to that predicted by Equation 6-4. All values represent PLA volume percent.

Material System	ϕ_{PLA}, lower bound	ϕ_{PLA}, upper bound	$\phi_{PLA\text{-}PI,exp}$, experimental center of cocontinuity range	$\phi_{PLA\text{-}PI,pred}$, predicted center of cocontinuity range, Equation 6-4	Deviation: $\phi_{PLA\text{-}PI,exp} - \phi_{PLA\text{-}PI,pred}$
HDPE/L-PLA	39	59	49	54.4	-5.4
HDPE/ M-PLA	35	71	53	52.7	0.3
HDPE/B-PLA	45	76	60.5	53.0	7.5
LDPE/L-PLA	24	58	41	61.4	-20.4
LDPE/Mixed PLA	25	76	50.5	59.9	-9.9
LDPE/B-PLA	34	76	55	60.2	-5.2

From the ranges of cocontinuity, it was observed that when blending with branched polymers, the blends were capable of forming cocontinuous networks containing a larger volume fraction of the branched polymer, or alternatively, formed cocontinuous blends with increasingly less of the other phase. This broadening of the range occurred despite no apparent increase in the shear viscosity at the blending shear rate when using branched polymers. The HDPE/L-PLA system, in which both phases were composed of linear polymers, showed the narrowest range of cocontinuous compositions, between 39-59 vol.% PLA. However, by replacing the linear PLA with a strain hardening material such as the M-PLA or B-PLA, the upper limit of PLA continuity can be extended from 59 vol.% PLA to as high as 76 PLA vol% PLA. Adding a branched PLA to

the HDPE blend systems resulted in only minimal deviation in the lower limit of cocontinuity, which remained at 40 ± 5 vol.% PLA.

Likewise, by substituting branched LDPE in place of the linear HDPE, the lower limit of PLA continuity is extended to as low as 24 vol.% PLA. This is particularly evident when comparing the case of HDPE/L-PLA to LDPE/L-PLA, where the upper bound of cocontinuity (58 vol.% PLA) remained unchanged, while the lower bound of continuity changed from 39 vol.% PLA for linear HDPE to 24 vol.% PLA for branched LDPE. In the case where both phases are branched and display strain hardening, the range of cocontinuity is extended in both directions, resulting in the widest ranges of cocontinuity, as seen in the LDPE/M-PLA system.

Broadening the cocontinuity range by branching provides a way to control the porosity of PE after selective extraction of PLA. Figure 6-6 shows the 3D structures of the porous PE with porosity of 25% (lower limit achieved by using branched PE), 56% and 76% (upper limit achieved by using branched PLA) respectively.

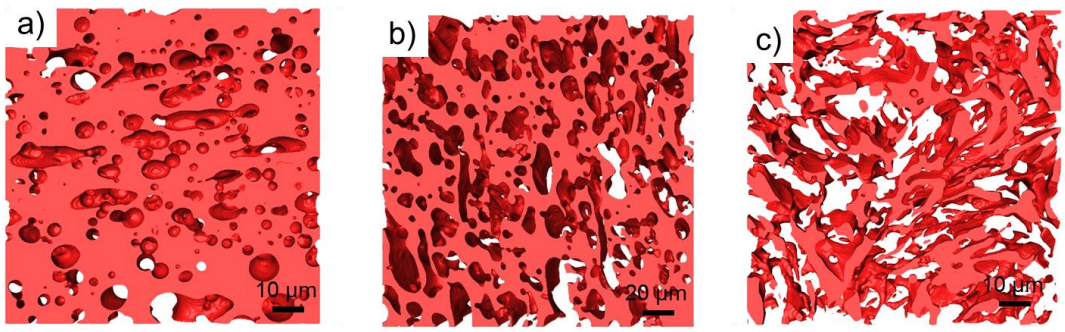

Figure 6-6 LSCM images of porous PE after PLA extraction from different blends. (a) LDPE/M-PLA 75/25 vol.% (b) LDPE/M-PLA 44/56 vol.% (c) HDPE/B-PLA 24/76 vol.%.

6.3.3 Size analysis

Characteristic size was measured for each of the six polymer combinations at volume fraction of 45/55 vol.% PE/PLA. Figure 6-7 shows representative SEM micrographs of the blends following PLA extraction in chloroform. As is observed in Figure 6-5, all of the samples at this

composition possess a cocontinuous morphology, and the SEM images qualitatively support this claim, being composed of continuously connected regions and what appear to be droplets. It is important to keep in mind that the appearance of droplet-like features is not necessarily indicative of a dispersed droplet morphology. The characteristic size of the blend, *a*, is reported with each image in Figure 6-7, and shown graphically in Figure 6-8.

In Figure 6-8 the characteristic size ranges two fold, from 3.8 to 7.7 μm. A minimum is observed for blends with an intermediate amount of branching, while HDPE/L-PLA with no branching and LDPE/B-PLA with a large amount of branching in each phase showed the largest characteristic size.

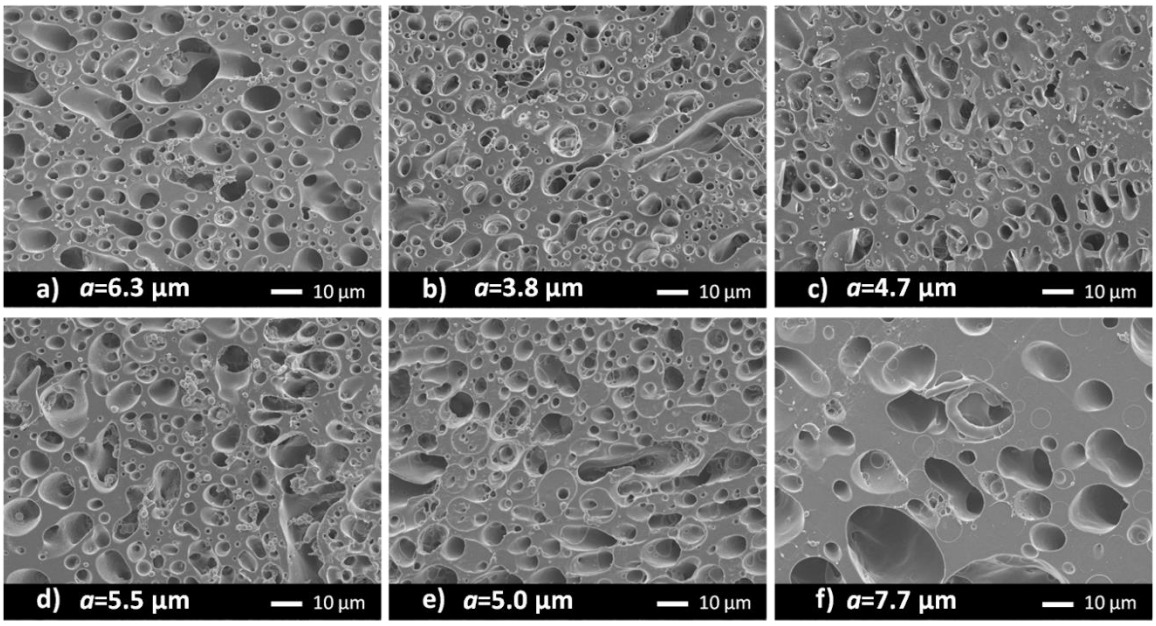

Figure 6-7 SEM images of PE/PLA blends at 45/55 vol.% after extracting PLA. (a) HDPE/L-PLA, (b) HDPE/M-PLA, (c) HDPE/B-PLA, (d) LDPE/L-PLA, (e) LDPE/M-PLA, and (f) LDPE/B-PLA. All scale bars are 10 μm, and the mean phase size, *a*, from analysis of LSCM images is reported with each micrograph.

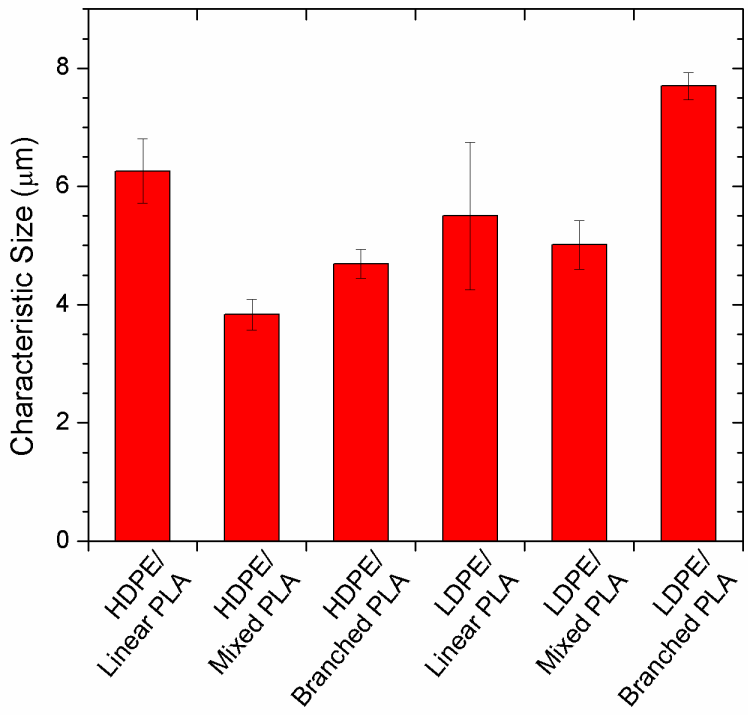

Figure 6-8 Initial mean characteristic size for 45/55 vol% PE/PLA blends. Error bars show one standard deviation for values of *a* from four different LSCM images. Overall branching content increases from left to right.

6.3.4 Stability analysis via coarsening

In order to investigate stability, blends at 45/55 volume% PE/PLA were also subjected to coarsening at 180 °C for up to 30 minutes. The coarsening results are shown in Figure 6-9. All the blends showed a continuous increase of characteristic size with annealing time with no apparent plateau, indicative of an uncompatibilized cocontinuous blend undergoing self-similar coarsening.

Theory predicts [44, 198, 199] that the rate of coarsening of a cocontinuous blend should be analogous to the rate of breakup of a viscous fiber in an infinite matrix of another viscous material[200]. The rate of cocontinuous coarsening is expected to follow Equation 6-5:

$$\frac{da}{dt} \propto \frac{\Gamma\Omega}{\eta} \tag{6-5}$$

where a is the blend characteristic size, Γ is the interfacial tension between the two phases, η is the matrix viscosity, and Ω is a tabulated function referred to as Tomotika's function, which describes the growth rate of the disturbance and is dependent on the viscosity ratio between the dispersed and matrix phase, η_d/η_m. The value of Ω approaches 1 as η_d/η_m becomes 0, and approaches 0 as η_d/η_m becomes infinite. For the present analysis, the interfacial tension Γ was measured following the Palierne viscoelastic droplet model, described more fully in other publications[106, 145, 201], and was measured to be approximately 11 mN/m for all combinations of PE and PLA.

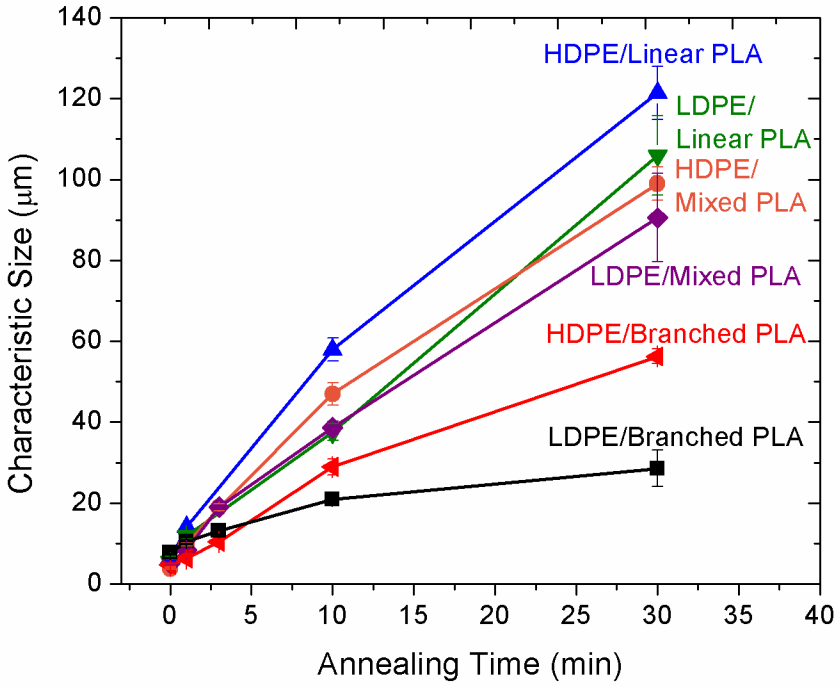

Figure 6-9 Characteristic phase size, a, of cocontinuous blended polymers as a function of annealing time at 180 °C. Error bars show one standard deviation of a, measured across three images.

Coarsening of cocontinuous blends poses a unique problem for evaluating Ω, in that there is no discernible dispersed and continuous phase: the assumption of an infinite matrix fails, as both phases exhibit both continuity and coarsening behavior, such that each phase simultaneously

satisfies the definition of both matrix and "breaking thread." However, we find that using $1/\eta_{blend}$ to replace the Ω/η term is an effective way to simplify the problem,

$$\frac{da}{dt} \propto \frac{\Gamma}{\eta_{blend}} \tag{6-6}$$

where $\ln(\eta_{blend}) = \phi_1 \ln(\eta_1) + \phi_2 \ln(\eta_2)$, the log volume average of the zero shear viscosities of the blend components. McMaster[202] has shown that for symmetric blends, $\phi_1 = 0.5$, and picking $\eta_1 \leq \eta_2$ then $1/\eta_{blend} \cong \Omega/2\eta$ over a fairly wide range of viscosity ratio, $0.05 < \eta_1/\eta_2 < 1$.

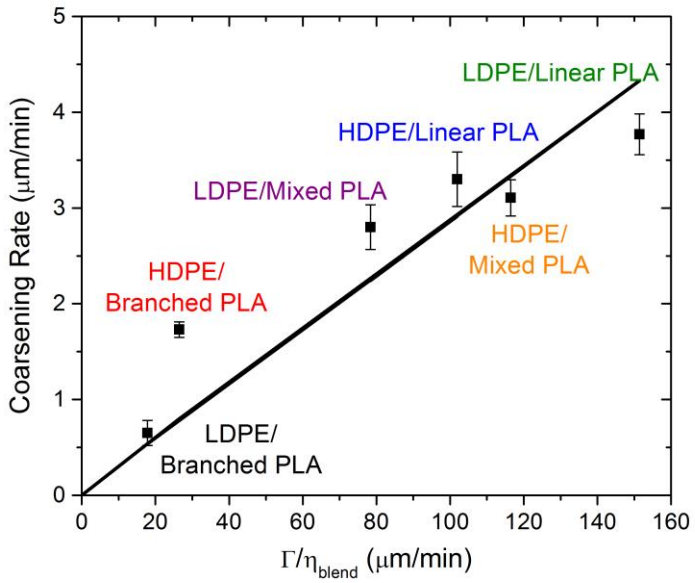

Figure 6-10 Coarsening rate of PE/PLA cocontinuous blends from 1-30 minutes of coarsening, as a function of Γ/η_{blend}. The line shows a linear regression with a zero intercept. Error bars show one standard deviation, measured across three samples.

The rate of coarsening was measured as the linear increase of the characteristic size from 1 – 30 minutes of annealing time. The characteristic size at 1 minute of coarsening was used as the initial condition to limit the effect of anisotropy in the initial sample – samples that had not undergone any coarsening were still shear aligned from the extrusion, which complicated

assumptions of self-similar coarsening during the first minute of annealing. The results for coarsening rate plotted against Γ/η_{blend} are shown in Figure 6-10. These results were fit with an intercept of zero, since infinite viscosity or zero interfacial tension would result in no coarsening.

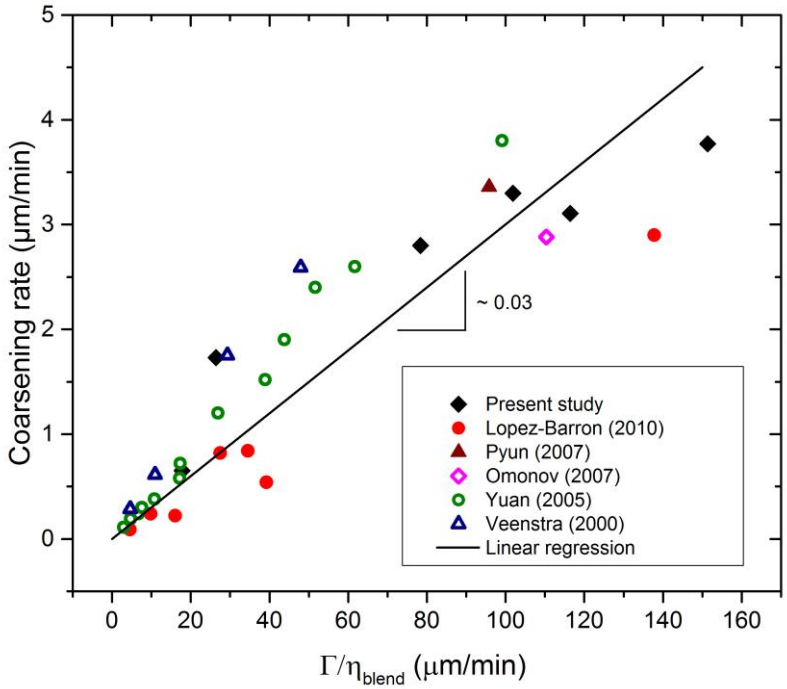

Figure 6-11 Coarsening rates of PE/PLA blends, compared to coarsening data from literature, plotted against Γ/η_{blend}. The literature studies are by Lopez-Barron and Macosko[45], Pyun *et al.*[203], Omonov *et al.*[204], Yuan and Favis[205], and Veenstra *et al.*[44]. The line shows the linear regression with zero intercept.

As can be seen in Figure 6-10, the rate of coarsening correlates linearly to the term Γ/η_{blend}, as predicted by Equation 6-6. Figure 6-11 compares these same results along with coarsening data from previous studies over a range of different material systems. The proportionality constant between the coarsening rate and Γ/η_{blend} is ~0.03 and independent of the material system, suggesting that the present relationship is both general and sufficient when no interfacial species are present. We note that one material pair in the literature, LDPE/polyethylene oxide also coarsened linearly

but significantly faster with a proportionality constant ~0.6[106].

The analysis here also suggests that coarsening of blend morphology during quiescent annealing is resisted primarily by the zero shear viscosity of the blend, and not by the strain hardening behavior of the constitutive polymers. Coarsening is a relatively small strain, long time process which occurs over minutes. As Figure 6-2 illustrates, strain hardening requires Hencky strains >1 and relatively rapid deformations.

6.4 Discussion

The fact that strain hardening expands the window of cocontinuity is a valuable result. This allows creation of high porosity films. But why does branching of one component allow the other to percolate into a continuous network with less material. As Table 6-3 shows, the predictions of the droplet packing model, Equation 6-4, fail to match the observed center of cocontinuity range, especially in cases where the PE and PLA differ in branching content. The reality is that cocontinuity exists over a range of compositions. There does not appear to be a theory which can predict the onset of cocontinuity from either side of the composition range.

Li and Favis[206] suggested a potential mechanism for cocontinuity formation, based on either fiber-fiber or droplet-droplet flow-induced coalescence of the minor phase into a continuous network. Coalescence occurs when dispersed features approach each other, thereby displacing the major-phase fluid between them in draining flow. The film of the major phase eventually ruptures, allowing contact and percolation of the dispersed features. This coalescence is limited by the rate at which the film can be drained – if the dispersed features flow past each other before the major phase film can rupture, no coalescence will occur. A schematic of droplet coalescence accompanied by draining flow of the major phase film is shown in Figure 6-12. It is expected that a strain hardening matrix fluid will resist the draining flow is step b, thereby reducing coalescence.

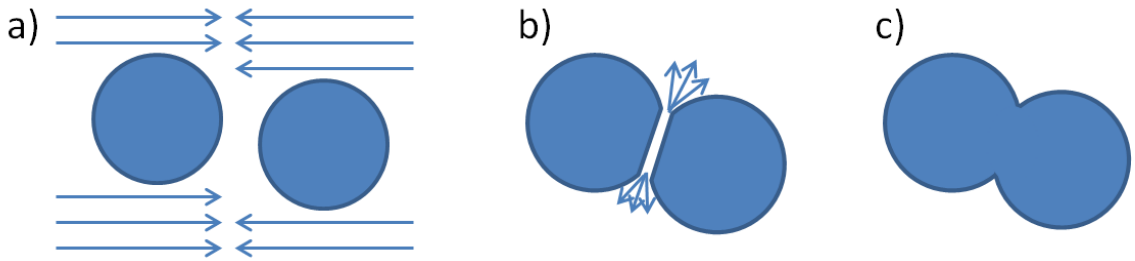

Figure 6-12 Schematic of droplet coalescence. (a) Droplets in a matrix flow towards each other. (b) The droplets collide, but the matrix fluid must be squeezed out of the space in draining flow. (c) The draining film of the matrix fluid ruptures, and the droplets coalesce.

An alternative mechanism for formation of a cocontinuous morphology has been proposed by Sundararaj *et al.*[207, 208]. They show that cocontinuity is a transition state resulting from sheet formation during initial stages of mixing. As the original polymer pellets or powder melt, sheets peal off and then break up irregularly to form an interpenetrating transition state over a broad range of compositions. This transition state can continue to develop either to "steady state" cocontinuous morphology or break up into dispersed droplets.

Based on this mechanism, the conditions for cocontinuity are less influenced by the ability of the minor phase to coalesce and percolate, and more influenced by the stability of sheets and elongated features formed during mixing flows. Considering the case of a strain hardening major phase and a non-strain hardening minor phase, the strain hardening phase serves two purposes. First, the viscosity of the major phase increases during extensional flows. This encourages the minor phase to encapsulate the higher viscosity material, as is observed in typical blending processes,[178, 209, 210] and also increases the time required to breakup any elongated domains. Second, as the major phase is stretched during extensional flows it transfers its deformation to the minor phase, promoting elongation of the minor phase. This is shown schematically in Figure 6-13. These elongated features would more readily percolate into a continuous network, as is shown schematically in Figure 6-14.

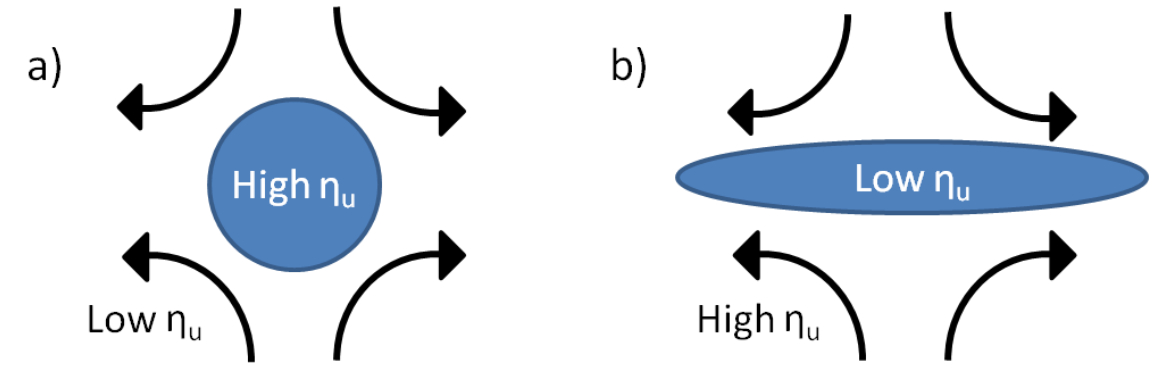

Figure 6-13 Droplet stretching in elongational flow. (a) A low viscosity matrix and high viscosity droplet resists stretching due to lower stress transfer to the dispersed phase. (b) A high viscosity matrix stretches the droplet due to higher stress transfer.

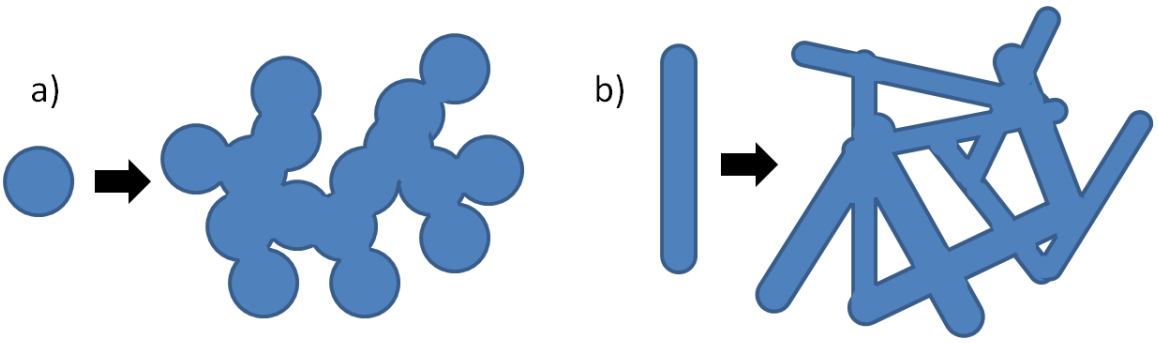

Figure 6-14 Schematic comparing percolation of spherical droplets to elongated features. Elongated features will more readily form a percolated network, and therefore promote cocontinuity. It is expected that strain hardening will stabilize elongated features by inhibiting fiber breakup.

The results reported here suggest a combined mechanism of cocontinuity formation, one based on both coalescence and stabilization of irregular features, will predict the observed behavior best. The trend of strain hardening matrices to promote percolation of their minor phase suggests that the second mechanism of the stabilization of elongated features must be taken into account, as theories of coalescence and percolation alone suggest an opposite outcome. However, coalescence is still needed to explain the lack of improvement of the cocontinuity range between higher degrees of strain hardening, particularly when considering that blends containing M-PLA tended to show a

wider range of cocontinuity compared to those containing B-PLA. Further increasing extensional viscosity of the PLA phase would inhibit coalescence and percolation by inhibiting draining flows, as observed previously in extrusion foaming[195, 211], which would explain the lack of improvement when using a fully branched PLA.

The competing role of strain hardening as both resisting flow and providing stability to elongated features can also serve to explain the dependence of the characteristic size of the blends on the strain hardening properties of the constitutive polymers. Characteristic size was minimized when blending with slightly strain hardening materials, and maximized when blending with two highly-branched materials or with two materials with no strain hardening. A fiber under extensional flow can experience necking, a flow instability which results in an uneven rate of deformation over the length of an elongated feature, with faster deformation within the necking region than outside of it. The presence of strain hardening behavior will increase the viscosity within the necking region, stabilizing that region so that strain hardening materials can achieve a higher degree of total elongation without breaking[212, 213]. This promotes the formation of narrower features as "fibers" within the matrix are able to be stretched further. However, a dramatically increased extensional viscosity due to a high degree of branching will resist extensional flow, and elongated features would be formed more slowly, allowing retraction into larger diameter features to occur.

6.5 Conclusions

The role of rheology in the formation of continuous morphology via melt blending of immiscible polymer was investigated. Long-chain branching dramatically increased both the extensional viscosity and the zero-shear viscosity of PE and PLA, while leaving the shear viscosity relatively unchanged at $\dot{\gamma} \geq 10 s^{-1}$. These materials provided a basis to explore the role of strain hardening in the formation of cocontinuous polymer blends, as the extensional flow properties

could be tuned independently while leaving shear flow properties at processing-relevant shear rates unchanged.

When blending with strain hardening materials, the range of compositions of complete cocontinuity was asymmetrically expanded to include more of the strain hardening material and less of the other dispersed phase while still retaining cocontinuity. Models in the literature fail to predict the center of the cocontinuity range, but more importantly they only consider a single phase inversion concentration. In reality concontinuity occurred over a wide concentration range, up to 25-76 vol% PLA when both polymers were branched.

The expansion of the range of cocontinuity was attributed to the stabilizing effect of a strain hardening matrix on dispersed elongated structures within that matrix. However, further increases in strain hardening, such as when blending with B-PLA instead of mixed PLA, did not further expand the cocontinuous range, suggesting that draining flows and extension of the dispersed phase into elongated features were suppressed due to the increased extensional viscosity. This suggests that the mechanism for the formation of cocontinuity depends simultaneously on the stability of elongated structures and on the percolation and coalescence of dispersed phases. Hence, strain hardening materials can expand the range of cocontinuity, up to the point where they inhibit draining flows during coalescence of the dispersed phase.

The initial characteristic size of the blends was minimized when blending with materials that showed slight amounts of strain hardening, and was maximized when blending with two linear, non-strain hardening materials or with two strongly strain hardening materials with $X_e > 9$. This supports the assertion above that some strain hardening can stabilize thinner elongated features in the blend, but an excessively strain hardening minor phase resists the formation of these thinner features. While long-chain branching did serve to slow down the rate of coarsening of these blends during post-processing annealing, this was not a result of strain hardening but rather increased zero-

shear viscosity. This was confirmed by the linear dependence of the coarsening rate on the ratio of interfacial tension to the log volume average zero-shear rate viscosity, Γ/η_{blend}. We find very similar dependence for nearly all the coarsening studies in the literature, indicating a universal relation with a coefficient of 0.03.

Chapter 7 Outlook

Great advances in PLA modification have been made over the past years.[30, 214, 215] The rapidly growing usage of PLA continues driving the development of new strategies to improve the performance and processability of PLA. Here we suggest some future directions which can further the efforts made in this thesis.

7.1 Use Pom-Pom model to study the critical chain segment length between branch points for extensional hardening

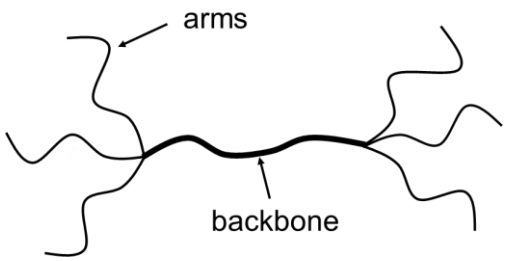

Figure 7-1 The structure of a pom-pom polymer.

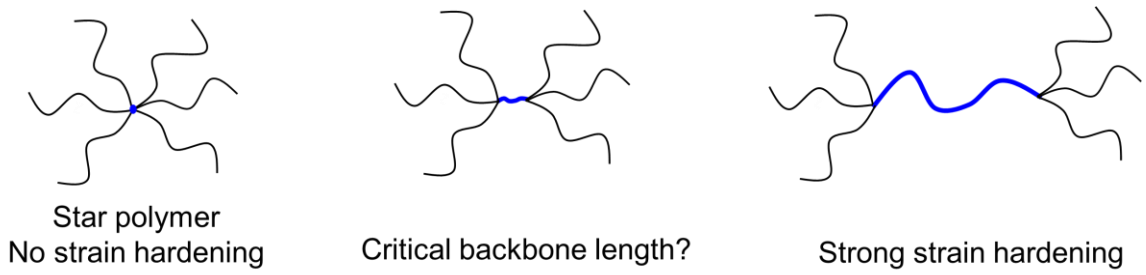

Figure 7-2 Transition from star polymer to pom-pom polymer.

As discussed in Chapter 2, star-shaped polymers can not strain harden in extensional flow. The Pom-Pom model introduced by McLeish and Larson[103] describes the extensional hardening behavior of long chain branched polymer with a simplified topology as show in Figure 7-1. The strain hardening comes from stretching of the backbone between the two branch points. The backbone can not relax freely because its ends are temporarily pinned by multiple branches. This allows build-up of large stress. Although the comb-shaped polymer in Chapter 3 is not a pom-pom

polymer, the Pom-Pom model can help understand the role of backbone length on extensional rheology. For our practical use, the arms are commercial linear PLA chains with high molecular weight, 80 kg/mol. If the backbone is very short, the pom-pom structure is actually a star polymer without strain hardening (Figure 7-2). There must be a critical backbone length (or transition range) for the onset of strain hardening. Yet we were not able to find any literature reports on this topic. It would be valuable to find the critical backbone length because it could teach us what type of molecule to synthesis for improving melt strength of PLA.

7.2 Synthesis of comb shaped PLA with well-defined comb topology

The GPC traces in Chapter 3 showed that there were a large amount of linear chains in the PLA branched with aziridine-functional PMMA by melt blending. The linear chains add to the difficulty of analyzing the structure of branched chains because rheology measures the collective properties of all chains in the sample. Since Chapter 3 demonstrated an easy synthesis route of poly(MMA-co-HEMA), we can use this random copolymer as initiator to make 100% comb-shaped PLA. We already showed that the backbone length and # functional group/chain can be easily tuned in the synthesis of poly(MMA-co-HEMA). Thus the effect of those factors on extensional rheology can be studied, which serves as experimental evidences for understanding the question brought up in Section 7.1.

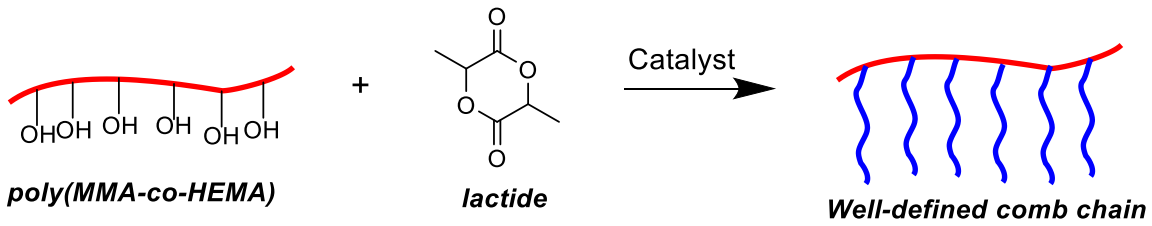

Figure 7-3 Synthesis of comb PLA.

7.3 Comb PLA/linear PLA blends

Blending the comb PLA in 7.2 with linear chains at known weight ratio helps decoupling their rheological response in extension flow. The effect of blending linear chains into branched chains on strain hardening can be studied.

7.4 3D printing of cocontinuous PLA/polycaprolactone (PCL) blend for hierarchical tissue scaffolding

Appendix A1 successfully used cocontinuous PLA/PS blend as a model system to make hierarchical porous PLA by fused deposition modeling. One drawback of PLA/PS blend is that PS is not biodegradable. Although solvent extraction can remove > 90% of the PS from the printed scaffold, small amount of PS remained in the scaffold as droplets. This is not good for implantations because after PLA degraded, PS remains in the body.

PCL is another biocompatible, biodegradable, and bioresorbable polymer widely used in biomedical engineering.[216] Porous PLA can be made from cocontinuous PLA/PCL blend by selective extracting PCL with ethyl acetate.[217] Unlike PS, the PCL droplet remaining in PLA is not a problem for in vivo applications. We can 3D-print PLA/PCL cocontinuous blends into a porous structure. Removing PCL from the printed object will result in a hierarchically porous PLA.

Bibliography

1 Callister, W. D. Materials Science and Engineering An Introduction, John Wiley & Sons, Inc.: Hoboken, NJ, 2003.

2 Plastics Insight: Global consumption of plastic materials by region. https://www.plasticsinsight.com/global-consumption-plastic-materials-region-1980-2015/ (accessed on 08/07/2017)

3 R. Geyer, J.R. Jambeck, K.L. Law, Sci. Adv. 3 (2017) e1700782.

4 A. Ammala, S. Bateman, K. Dean, E. Petinakis, P. Sangwan, S. Wong, Q. Yuan, L. Yu, C. Patrick, K.H. Leong, Prog. Polym. Sci. 36 (2011) 1015–1049.

5 S.A. Miller, ACS Macro Lett. 2 (2013) 550–554.

6 J. R. Jambeck, R. Geyer, C. Wilcox, T. R. Siegler, M. Perryman, A. Andrady, R. Narayan, K. L. Law, Science 347 (2015) 768–771.

7 M.R. Gregory, Philos. Trans. R. Soc. B Biol. Sci. 364 (2009) 2013–2025.

8 M. Wagner, C. Scherer, D. Alvarez-Muñoz, N. Brennholt, X. Bourrain, S. Buchinger, E. Fries, C. Grosbois, J. Klasmeier, T. Marti, S. Rodriguez-Mozaz, R. Urbatzka, A.D. Vethaak, M. Winther-Nielsen, G. Reifferscheid, Environ. Sci. Eur. 26 (2014) 12.

9 M.C. Rillig, Environ. Sci. Technol. 46 (2012) 6453–6454.

10 A. M. Mannion, Rheological Design of Sustainable Block Copolymers. Ph.D. thesis (2016), University of Minnesota.

11 J. Hopewell, R. Dvorak, E. Kosior, Philos. Trans. R. Soc. B Biol. Sci. 364 (2009) 2115–2126.

12 R.C. Thompson, S.H. Swan, C.J. Moore, F.S. vom Saal, Philos. Trans. R. Soc. B Biol. Sci. 364 (2009) 1973–1976.

13 D.K. Schneiderman, M.A. Hillmyer, Macromolecules. 50 (2017) 3733–3749.

14 Growth in PLA bioplastics: a production capacity of over 800,000 tonnes expected by 2020. http://www.bioplasticsmagazine.com/en/news/meldungen/PLA_Growth.php (accessed on 08/07/2017).

15 R. Datta, M. Henry, J. Chem. Technol. Biotechnol. 81 (2006) 1119–1129.

16 O. Dechy-Cabaret, B. Martin-Vaca, D. Bourissou, Chem. Rev. 104 (2004) 6147–6176.

17 D.W. Grijpma, a. J. Pennings, Macromol. Chem. Phys. 195 (1994) 1633–1647.

18 K. Madhavan Nampoothiri, N.R. Nair, R.P. John, Bioresour. Technol. 101 (2010) 8493–8501.

19 R. Auras, L.-T. Lim, S. E.M. Selke, H. Tsuji, Ploy(lactic acid): Synthesis, Structures, Properties, Processing and Applications, John Wiley & Sons, Inc.: Hoboken, NJ, 2010.

20 Y. Ikada, K. Jamshidi, H. Tsuii, S.H. Hyon, Macromolecules. 20 (1987) 904–906.

21 I. Engelberg, J. Kohn, Biomaterials. 12 (1991) 292–304.

22 H. Urayama, S. Il Moon, Y. Kimura, Macromol. Mater. Eng. 288 (2003) 137–143.

23 J.R. Dorgan, J. Janzen, M.P. Clayton, S.B. Hait, D.M. Knauss, J. Rheol. 49 (2005) 607–619.

24 J. Ahmed, J.X. Zhang, Z. Song, S.K. Varshney, J. Therm. Anal. Calorim. 95 (2009) 957–964.

25 P. Pan, B. Zhu, Y. Inoue, Macromolecules. 40 (2007) 9664–9671.

26 NatureWorks, Crystallizing and Drying Ingeo Biopolymer, NatureWorks LLC, Minnetonka, MN.

27 R.E. Drumright, P.R. Gruber, D.E. Henton, Adv. Mater. 12 (2000) 1841–1846.

28 P. R. Gruber, E. S. Hall, J. J. Kolstad, M. L. Iwen, R. D. Benson, R. L. Borchardt, Continuous process for manufacture of lactide polymers with purification by distillation, U.S. Patent 5,357,035, 1994.

29 P. R. Gruber, E. S. Hall, J. J. Kolstad, M. L. Iwen, R. D. Benson, R. L. Borchardt, Continuous process for the manufacture of lactide and lactide polymers, U.S. Patent 6,326,458, 2001.

30 H. Liu, J. Zhang, J. Polym. Sci. Part B Polym. Phys. 49 (2011) 1051–1083.

31 G.M. Jordhamo, J.A. Manson, L.H. Sperling, Polym. Eng. Sci. 26 (1986) 517–524.

32 I.S. Miles, A. Zurek, Polym. Eng. Sci. 28 (1988) 796–805.

33 D.R. Paul, C.B. Bucknall (2000). Polymer Blends Volume 1: Formulation, John Wiley & Sons, Inc.: Hoboken, NJ, 2000.

34 X. Zhang, Z. Yin, J. Yin, J. Appl. Polym. Sci. 62 (1996) 893–901.

35 I. Forteln, J. Kova, Eur. Polym. J. 28 (1992) 85–90.

36 R.M. Ho, C.H. Wu, A.C. Su, Polym. Eng. Sci. 30 (1990) 511–518.

37 B. De Roover, J. Devaux, R. Legras, J. Polym. Sci. Part A Polym. Chem. 35 (1997) 917–925.

38 V.I. Metelkin, V.S. Blekht, Colloid Journal of the USSR. 46 (1984), 425.

39 L.A. Utracki, J. Rheol. 35 (1991) 1615–1637.

40 R.C. Willemse, A. Posthuma de Boer, J. van Dam, A.D. Gotsis, Polymer. 39 (1998) 5879–5887.

41 R.C. Willemse, Polymer. 40 (1999) 2175–2178.

42 R.C. Willemse, A. Posthuma De Boer, J. Van Dam, A.D. Gotsis, Polymer. 40 (1998) 827–834.

43 A.T. Hedegaard, Effect of Viscosity Ratio and Interfacial Reaction on Cocontinuity. Ph.D. Thesis (2013), University of Minnesota, 79-111.

44 H. Veenstra, J. Van Dam, A. Posthuma de Boer, Polymer. 41 (2000) 3037–3045.

45 C.R. López-Barrón, C.W. Macosko, Soft Matter. 6 (2010) 2637–2647.

46 C.W. Macosko, P. Guégan, A.K. Khandpur, A. Nakayama, P. Marechal, T. Inoue, Macromolecules. 29 (1996) 5590–5598.

47 B. Majumdar, H. Keskkula, D.R. Paul, Polymer. 35 (1994) 3164–3172.

48 H.K. Jeon, C.W. Macosko, B. Moon, T.R. Hoye, Z. Yin, Macromolecules. 37 (2004) 2563–2571.

49 C. Calberg, S. Blacher, F. Gubbels, F. Brouers, R. Deltour, R. Jérôme, J. Phys. D. Appl. Phys. 32 (1999) 1517–1525.

50 L. Bai, S. He, J.W. Fruehwirth, A. Stein, C.W. Macosko, X. Cheng, J. Rheol. 61 (2017) 575–587.

51 L. Bai, J.W. Fruehwirth, X. Cheng, C.W. Macosko, Soft Matter. 11 (2015) 5282–5293.

52 S. Huang, L. Bai, M. Trifkovic, X. Cheng, C.W. Macosko, Macromolecules. 49 (2016) 3911–3918.

53 L. Bai, R. Sharma, X. Cheng, C.W. Macosko, Langmuir. (2017) doi: 10.1021/acs.langmuir.7b03085.

54 C.R. López-Barrón, On the Coarsening of Immiscible Polymer Blends with Cocontinuous Morphology. Ph.D. Thesis (2009), University of Minnesota, 74-77.

55 H.C. Lau, S.N. Bhattacharya, G.J. Field, Polym. Eng. Sci. 38 (1998) 1915–1923.

56 C. Gabriel, H. Münstedt, J. Rheol. 47 (2003) 619.

57 A.D. Gotsis, B.L.F. Zeevenhoven, A.H. Hogt, Polym. Eng. Sci. 44 (2004) 973–982.

58 H. Münstedt, J. Rheol. 24 (1980) 847–867.

59 D.J.A. Cameron, M.P. Shaver, Chem. Soc. Rev. 40 (2011) 1761–1776.

60 Y. Ohya, S. Maruhashi, T. Ouchi, Macromol. Chem. Phys. 199 (1998) 2017–2022.

61 Q. Xin, A. Wirsén, A.C. Albertsson, J. Appl. Polym. Sci. 74 (1999) 3193–3202.

62 A. Breitenbach, T. Kissel, Polymer. 39 (1998) 3261–3271.

63 F. Tasaka, Y. Ohya, T. Ouchi, Macromol. Rapid Commun. 22 (2001) 820–824.

64 L.M. Pitet, S.B. Hait, T.J. Lanyk, D.M. Knauss, Macromolecules. 40 (2007) 2327–2334.

65 S. Skaria, M. Smet, H. Frey, Macromol. Rapid Commun. 23 (2002) 292–296.

66 C.-Q. Chen, D.-M. Ke, T.-T. Zheng, G.-J. He, X.-W. Cao, X. Liao, Ind. Eng. Chem. Res. 55 (2016) 597–605.

67 H. Fang, Y. Zhang, J. Bai, Z. Wang, Z. Wang, RSC Adv. 3 (2013) 8783–8795.

68 Y. Wang, L. Yang, Y. Niu, Z. Wang, J. Zhang, F. Yu, H. Zhang, J. Appl. Polym. Sci. 122 (2011) 1857–1865.

69 H. Xu, H. Fang, J. Bai, Y. Zhang, Z. Wang, Ind. Eng. Chem. Res. 53 (2014) 1150–1159.

70 D. Carlson, P. Dubois, L. Nie, R. Narayan, Polym. Eng. Sci. 38 (1998) 311–321.

71 K.M. Dean, E. Petinakis, S. Meure, L. Yu, A. Chryss, J. Polym. Environ. 20 (2012) 741–747.

72 J. You, L. Lou, W. Yu, C. Zhou, J. Appl. Polym. Sci. 129 (2013) 1959–1970.

73 J.J. Cernohous, G.S. Van Gordon, "Biobased polymer compositions," U.S. patent EPf 2010108076 A2 (2010).

74 A.T. Hedegaard, L. Gu, C.W. Macosko, J. Rheol. 59 (2015) 1397–1417.

75 J. Cailloux, O.O. Santana, M.L. Maspoch, J.J. Bou, F. Carrasco, J. Rheol. 59 (2015) 1191–1227.

76 B. Mallet, K. Lamnawar, A. Maazouz, Polym. Eng. Sci. 54 (2014) 840–857.

77 Q. Meng, M.-C. Heuzey, P.J. Carreau, Polym. Degrad. Stab. 97 (2012) 2010–2020.

78 M. Mihai, M.A. Huneault, B.D. Favis, Polym. Eng. Sci. 50 (2010) 629–642.

79 J. Liu, L. Lou, W. Yu, R. Liao, R. Li, C. Zhou, Polymer. 51 (2010) 5186–5197.

80 J. Liu, S. Zhang, L. Zhang, Y. Bai, Ind. Eng. Chem. Res. 52 (2012) 13670–13679.

81 C.A. Orr, J.J. Cernohous, P. Guegan, A. Hirao, H.K. Jeon, C.W. Macosko, Polymer. 42 (2001) 8171–8178.

82 C. Thurber, L. Gu, J.C. Myers, T.P. Lodge, C. W. Macosko, Polym. Eng. Sci. (2017) DOI 10.1002/pen.24527.

83 M. Villalobos, A. Awojulu, T. Greeley, G. Turco, G. Deeter, Energy. 31 (2006) 3227–3234.

84 Randall, J. R., K. Cink, and J. C. Smith, "Branched polylactic acid polymers and method of preparing same," U. S. Patent WO2006002372 A2 (2006).

85 J.R. Dorgan, J. Janzen, D.M. Knauss, S.B. Hait, B.R. Limoges, M.H. Hutchinson, J. Polym. Sci. Part B Polym. Phys. 43 (2005) 3100–3111.

86 C. Jackson, Y-J. Chen, J.W. Mays, J. Appl. Polym. Sci. 61, 865-874 (1996).

87 G. Tillet, B. Boutevin, B. Ameduri, Prog. Polym. Sci. 36 (2011) 191–217.

88 V. Vargha, O. Vorster, Z. Finta, G. Csuka, J. Therm. Anal. Calorim. 83 (2006) 199–206.

89 F. Liu, Z. Wang, D. Liu, J. Li, Polym. Int. 58 (2009) 912–918.

90 R. Dhavalikar, M. Xanthos, Polym. Eng. Sci. 44 (2004) 474–486.

91 S. Japon, L. Boogh, Y. Leterrier, J.A.E. Månson, Polymer. 41 (2000) 5809–5818.

92 B.H. Zimm, W.H. Stockmayer, J. Chem. Phys. 17 (1949) 1301–1314.

93 R. Roesler, Prog. Org. Coatings. 50 (2004) 1–27.

94 J.R. Dorgan, J.S. Williams, D.N. Lewis, J. Rheol. 43 (1999) 1141–1155.

95 L. Martinetti, C.W. Macosko, F.S. Bates, J. Polym. Sci. Part B Polym. Phys. 54 (2016) 1437–1442.

96 D.R. Daniels, T.C.B. McLeish, R. Kant, B.J. Crosby, R.N. Young, A. Pryke, J. Allgaier, D.J. Groves, R.J. Hawkins, Rheol. Acta. 40 (2001) 403–415.

97 T.C.B. McLeish, Adv. Phys. 51 (2002) 1379–1527.

98 S. Trinkle, C. Freidrich, Rheol. Acta. 40 (2001) 322–328.

99 S. Trinkle, P. Walter, C. Friedrich, Rheol. Acta. 41 (2002) 103–113.

100 M. Kempf, D. Ahirwal, M. Cziep, M. Wilhelm, Macromolecules. 46 (2013) 4978–4994.

101 D.J. Lohse, S.T. Milner, L.J. Fetters, M. Xenidou, N. Hadjichristidis, R.A. Mendelson, C.A. García-Franco, M.K. Lyon, Macromolecules. 35 (2002) 3066–3075.

102 H. Lentzakis, C. Das, D. Vlassopoulos, D.J. Read, J. Rheol. 58 (2014) 1855–1875.

103 T.C.B. McLeish, R.G. Larson, J. Rheol. 42 (1998) 81–110.

104 C.H. Tselios, D. Bikiaris, J. Prinos, C. Panayiotou, J. Appl. Polym. Sci. 64 (1997) 983–999.

105 M. Flores, G. Hernandez, A. Escobar, J. Cardoso, A. Palma, A. Maciel, E. Sanchez, O. Manero, J. Appl. Polym. Sci. 67 (1998) 1071–1083.

106 M. Trifkovic, A. Hedegaard, K. Huston, M. Sheikhzadeh, C.W. Macosko, Macromolecules. 45 (2012) 6036–6044.

107 C.W. Macosko, D.R. Miller, Macromolecules. 9 (1976) 199–206.

108 J. Stange, C. Uhl, H. Münstedt, J. Rheol. 49 (2005) 1059–1079.

109 D. Auhl, F.J. Stadler, H. Münstedt, Macromolecules. 45 (2012) 2057–2065.

110 A. Malmberg, C. Gabriel, T. Steffl, H. Münstedt, B. Löfgren, Macromolecules. 35 (2002) 1038–1048.

111 M. Yamaguchi, K.I. Suzuki, S. Maeda, J. Appl. Polym. Sci. 86 (2002) 73–78.

112 H. Lentzakis, D. Vlassopoulos, D.J. Read, H. Lee, T. Chang, P. Driva, N. Hadjichristidis, J. Rheol. 57 (2013) 605.

113 G. Zhang, J. Zhang, S. Wang, D. Shen, J. Polym. Sci. Part B Polym. Phys. 41 (2003) 23–30.

114 L.J. Fetters, D.J. Lohse, D. Richter, T.A. Witten, A. Zirkel, Macromolecules. 27 (1994) 4639–4647.

115 Y. Hu, Y.S. Hu, V. Topolkaraev, A. Hiltner, E. Baer, Polymer 44 (2003) 5711–5720.

116 Y. Hu, M. Rogunova, V. Topolkaraev, A. Hiltner, E. Baer, Polymer 44 (2003) 5701–5710.

117 Z. Kulinski, E. Piorkowska, K. Gadzinowska, M. Stasiak, Biomacromolecules. 7 (2006) 2128–2135.

118 E. Piorkowska, Z. Kulinski, A. Galeski, R. Masirek, Polymer 47 (2006) 7178–7188.

119 K.M. Choi, M.C. Choi, D.H. Han, T.S. Park, C.S. Ha, Eur. Polym. J. 49 (2013) 2356–2364.

120 Z. Kulinski, E. Piorkowska, Polymer 46 (2005) 10290–10300.

121 M. Sheth, R.A. Kumar, V. Dave, R. a Gross, S.P. Mccarthy, J. Appl. Polym. Sci. 66 (1997) 1495–1505.

122 Brandrup, J., and E. H. Immergut, eds. Polymer Handbook, Wiley-Interscience, New York, 1989.

123 http://www.dow.com/polyglycols/ppgc/na/products/ppgs.htm accessed 10/20/2017

124 M.H. Hutchinson, J.R. Dorgan, D.M. Knauss, S.B. Hait, J. Polym. Environ. 14 (2006) 119–124.

125 T. Li, J. Zhang, D.K. Schneiderman, L.F. Francis, F.S. Bates, ACS Macro Lett. 5 (2016) 359–364.

126 T. Li, M.J. Heinzer, L.F. Francis, F.S. Bates, J. Polym. Sci. Part B Polym. Phys. 54 (2016) 189–204.

127 T. Li, M.J. Heinzer, E.M. Redline, F. Zuo, F.S. Bates, L.F. Francis, Prog. Org. Coatings. 77 (2014) 1145–1154.

128 T. Li, S. He, A. Stein, L.F. Francis, F.S. Bates, Macromolecules. 49 (2016) 9507–9520.

129 M. Pluta, E. Piorkowska, Polymer testing. 46 (2015) 79-87.

130 T.G. Park, S. Cohen, R. Langer, Macromolecules. 25 (1992) 116–122.

131 É. Kiss, K. Dravetzky, K. Hill, E. Kutnyánszky, A. Varga, J. Colloid Interface Sci. 325 (2008) 337–345.

132 P. Alexandridis, T. Alan Hatton, Colloids Surfaces A Physicochem. Eng. Asp. 96 (1995) 1–46.

133 D.H. Builes, H. Hernandez, I. Mondragon, A. Tercjak, J. Phys. Chem. 117 (2013) 3563–3571.

134 M. Maric, C.W. Macosko, Polym. Eng. Sci. 41 (2001) 118–130.

135 J. E. Mark, Polymer Data Handbook, Oxford University Press, Inc., 1999, 545–546.

136 W.C. Lai, W.B. Liau, T.T. Lin, Polymer 45 (2004) 3073–3080.

137 A.J. Nijenhuis, E. Colstee, D.W. Grijpma, A.J. Pennings, Polymer 37 (1996) 5849–5857.

138 M. Kowalczyk, M. Pluta, E. Piorkowska, N. Krasnikova, J. Appl. Polym. Sci. 125 (2012) 4292–4301.

139 A. Zubrowska, E. Piorkowska, A. Kowalewska, M. Cichorek, Colloid Polym. Sci. 293 (2014) 23–33.

140 M. Kowalczyk, E. Piorkowska, S. Dutkiewicz, P. Sowinski, Eur. Polym. J. 59 (2014) 59–68.

141 M. Pluta, E. Piorkowska, Polymer testing. 46 (2015) 79-87.

142 J.Z. Liang, R.K.Y. Li, J. Appl. Polym. Sci. 77 (2000) 409–417.

143 J. Yang, Y. Zhang, Y. Zhang, Polymer 44 (2003) 5047–505.

144 http://www.xplore-together.com/products/software/rheological Accessed on 8/4/2017.

145 D. Graebling, R. Muller, J.F. Palierne, Macromolecules. 26 (1993) 320–329.

146 P. Salehi, P. Sarazin, B.D. Favis, Biomacromolecules. 9 (2008) 1131–1138.

147 D.H. Rosenzweig, E. Carelli, T. Steffen, P. Jarzem, L. Haglund, Int. J. Mol. Sci. 16 (2015) 15118–15135.

148 X. Liu, P.X. Ma, Ann. Biomed. Eng. 32 (2004) 477–486.

149 S. Ghosh, J.C. Viana, R.L. Reis, J.F. Mano, Acta Biomater. 4 (2008) 887–896.

150 M. Nofar, C.B. Park, Prog. Polym. Sci. 39 (2014) 1721–1741.

151 A. Bertrand, M.A. Hillmyer, J. Am. Chem. Soc. 135 (2013) 10918–10921.

152 S. Ravati, B.D. Favis, Polymer. 51 (2010) 4547–4561.

153 J. Wang, B.H. Lessard, M. Maric, B.D. Favis, Polymer. 55 (2014) 3461–3467.

154 H. Sai, K.W. Tan, K. Hur, E. Asenath-Smith, R. Hovden, Y. Jiang, M. Riccio, D.A. Muller, V. Elser, L.A. Estroff, S.M. Gruner, U. Wiesner, Science. 341 (2013) 530–534.

155 D.M.G. Cruz, M. Gomes, R.L. Reis, D. Moratal, M. Salmerón-Sánchez, J.L.G. Ribelles, J.F. Mano, J. Biomed. Mater. Res. A. 95 (2010) 1182–93.

156 P.A. George, K. Quinn, J.J. Cooper-White, Biomaterials. 31 (2010) 641–647.

157 J.R. Jones, P.D. Lee, L.L. Hench, Philos. Trans. A. Math. Phys. Eng. Sci. 364 (2006) 263–281.

158 P. Sarazin, B.D. Favis, Biomacromolecules. 4 (2003) 1669–1679.

159 Z. Yuan, B.D. Favis, Biomaterials. 25 (2004) 2161–2170.

160 D. Yao, W. Zhang, J.G. Zhou, Biomacromolecules. 10 (2009) 1282–1286.

161 H.K. Jeon, J. Zhang, C.W. Macosko, Polymer. 46 (2005) 12422–12429.

162 C. Koning, M. Van Duin, C. Pagnoulle, R. Jerome, Prog. Polym. Sci. 23 (1998) 707–757.

163 E.M. Fry, J. Org. Chem. 15 (1950) 802–806.

164 W.E. Baker, M. Saleem, Polymer. 28 (1987) 2057–2062.

165 M. Saleem, W.E. Baker, J. Appl. Polym. Sci. 39 (1990) 655–678.

166 N.C. Beck Tan, S.K. Tai, R.M. Briber, Polymer. 37 (1996) 3509–3519.

167 T. Vainio, G.-H. Hu, M. Lambla, J. V. Seppälä, J. Appl. Polym. Sci. 61 (1996) 843–852.

168 S. Lee, O.O. Park, Polymer. 42 (2001) 6661–6668.

169 X. Liu, F. La Mantia, R. Scaffaro, J. Appl. Polym. Sci. 86 (2002) 449–455.

170 G. Pompe, P. Ptschke, J. Pionteck, J. Appl. Polym. Sci. 86 (2002) 3445–3453.

171 B. Liu, L. Jiang, H. Liu, J. Zhang, Ind. Eng. Chem. Res. 49 (2010) 6399–6406.

172 M. Wulf, S. Michel, K. Grundke, O.I. del Rio, D.Y. Kwok, A.W. Neumann, J. Colloid Interface Sci. 210 (1999) 172–181.

173 J.A. Galloway, K.J. Koester, B.J. Paasch, C.W. Macosko, Polymer. 45 (2004) 423–428.

174 C.R. Lopez-Barron, C.W. Macosko, Langmuir. 25 (2009) 9392–404.

175 R. Zhao, C.W. Macosko, J. Rheol. 46 (2002) 145–167.

176 P. Van Puyvelde, Z. Oommen, P. Koets, G. Groeninckx, P. Moldenaers, Polym. Eng. Sci. 43 (2003) 71–77.

177 L.A. Utracki, Polym. Eng. Sci. 23 (1983) 602–609.

178 D. Bourry, B.D. Favis, J. Polym. Sci. Part B Polym. Phys. 36 (1998) 1889–1899.

179 J.R. Bell, K. Chang, C.R. López-Barrón, C.W. Macosko, D.C. Morse, Macromolecules. 43 (2010) 5024–5032.

180 G. Pu, Y. Luo, A. Wang, B. Li, Macromolecules. 44 (2011) 2934–2943.

181 G. Biresaw, C.J. Carriere, J. Polym. Sci. Part B Polym. Phys. 40 (2002) 2248–2258.

182 E. Jalali Dil, B.D. Favis, Polymer. 77 (2015) 156–166.

183 A.S. Zalusky, R. Olayo-Valles, J.H. Wolf, M. A. Hillmyer, J. Am. Chem. Soc. 124 (2002) 12761–73.

184 S. Torza, S.G. Mason, J. Colloid Interface Sci. 33 (1970) 67–83.

185 S.Y. Hobbs, M.E.J. Dekkers, V.H. Watkins, Polymer. 29 (1988) 1598–1602.

186 W.D. Harkins, A. Feldman, Films. J. Am. Chem. Soc. 44 (1922) 2665–2685.

187 W.D. Harkins, J. Chem. Phys. 9 (1941) 552.

188 S. Wu, J. Colloid Interface Sci. 31 (1969) 153–161.

189 I. Luzinov, C. Pagnoulle, R. Jérôme, Polymer. 41 (2000) 3381–3389.

190 P.H.M. Elemans, J.M.H. Janssen, H.E.H. Meijer, J. Rheol. 34 (1990) 1311–1325.

191 Z. Yuan, B.D. Favis, J. Polym. Sci. Part B Polym. Phys. 44 (2006) 711–721.

192 C.W. Macosko, Rheology Principles, Measurements, and Applications, VHC, New York, NY, 1994.

193 F.N. Cogswell, Polym. Eng. Sci. 12 (1972), 64-73.

194 F.N. Cogswell, Trans. Soc. Rheol. 16 (1972), 383-403.

195 P. Spitael, C.W. Macosko, Polym. Eng. Sci. 44 (2004) 2090–2100.

196 H.J. Lehermeier, J.R. Dorgan, Polym. Eng. Sci. 41 (2001) 2172–2184.

197 M. Padmanabhan, and C. W. Macosko, Rheol. Acta 36 (1997), 144-151 (1997).

198 L.P. McMaster, Aspects of liquid-liquid phase transition phenomena in multicomponent polymeric systems, Adv. Chem. Ser (1975) 43–65.

199 E.D. Siggia, Phys. Rev. A. 20 (1979) 595–605.

200 S. Tomotika, P. Roy Soc. Lond. A Mat. 150 (1935), 322-337.

201 U. Jacobs, M. Fahrlander, J. Winterhalter, and C. Friedrich, J. Rheol. 43 (1999), 1495-1509.

202 L.P. McMaster, AIChE J. 62 (2016) 4140–4156.

203 A. Pyun, J.R. Bell, K.H. Won, B.M. Weon, S.K. Seol, J.H. Je, C.W. Macosko, Macromolecules. 40 (2007) 2029–2035.

204 T.S. Omonov, C. Harrats, G. Groeninckx, P. Moldenaers, Polymer. 48 (2007) 5289–5302.

205 Z. Yuan, B.D. Favis, AIChE J. 51 (2005) 271–280.

206 J. Li, P.L. Ma, B.D. Favis, Macromolecules. 35 (2002) 2005–2016.

207 U. Sundararaj, Y. Dori, C. Macosko, Polymer. 36 (1995) 1957–1968.

208 U. Sundararaj, C.W. Macosko, C.-K. Shih, Polym. Eng. Sci. 36 (1996) 1769–1781.

209 B.D. Favis, J. P. Chalifoux, Polymer 29 (1998), 1761-1767.

210 S. Steinmann, W. Gronski, C. Friedrich, Polymer 42 (2001), 6619-6629.

211 J. Stange, H. Münstedt, J. Rheol. 50 (2006) 907.

212 R. G. Larson, Macromolecules 34 (2001), 4556-4571.

213 G.H. McKinley, T. Sridhar, Annu. Rev. Fluid Mech. 34 (2002), 375-415.

214 R.M. Rasal, A. V. Janorkar, D.E. Hirt, Prog. Polym. Sci. 35 (2010) 338–356.

215 L.-T. Lim, R. Auras, M. Rubino, Prog. Polym. Sci. 33 (2008) 820–852.

216 M.A. Woodruff, D.W. Hutmacher, Prog. Polym. Sci. 35 (2010) 1217–1256.

217 P. Sarazin, X. Roy, B.D. Favis, Biomaterials. 25 (2004) 5965–78.

Appendix 1 3D printing of cocontinuous immiscible polymer blends for hierarchically porous polymer*

A1.1 Abstract

Fused deposition modeling, commonly referred to as 3D printing, has been lauded for its great ease in fabrication and ability to allow for rapid, low-risk prototyping. As a continuation of Chapter 4, this work uses fused deposition modeling to print co-continuous PLA/PS blend into a well-defined structure with 1 mm pores. Extraction of PS with cyclohexane results in hierarchically porous PLA scaffold which maintains its original printed geometry. This porous PLA scaffold exhibits a unique interconnected, fibrous morphology that may present better functional capabilities for specific biomedical applications.

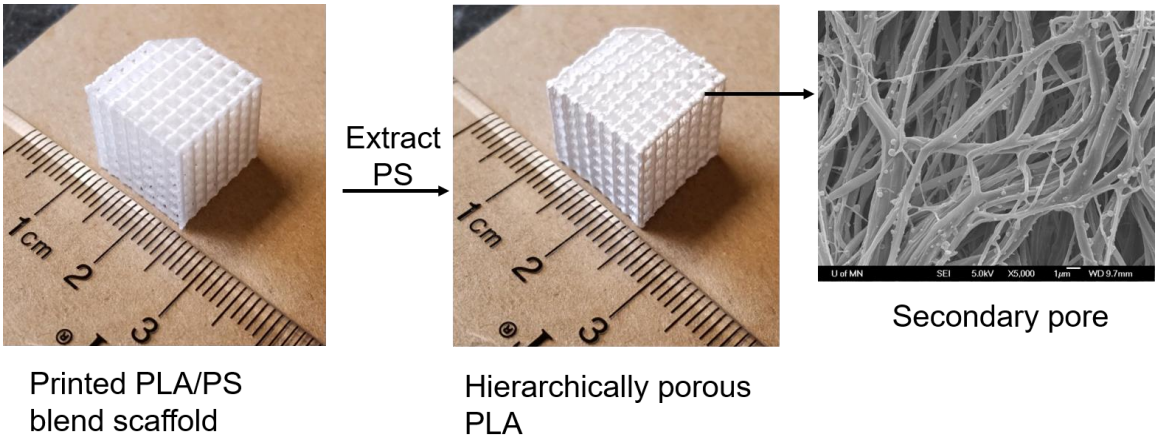

Figure A1-1 Hierarchically porous PLA from 3D printed cocontinuous blends. The primary pore size (~ 1 mm) can be tuned by computer aided design and secondary pore size (~1 μm) can be tuned by polymer viscosity and compatibilization.

* Portions of this work was done in collaboration with Jamie Wooding and Jeanette Caronia. Financial support for this work came from the National Science Foundation through the Center for Sustainable Polymers (CHE-1413862).

A1.2 Background

In tissue engineering, a highly porous scaffold aids in mass transport of cell nutrition, encourages cell migration and cell proliferation, and allows better host tissue to scaffold integration once the scaffold is placed into the body[1 - 4]. In discussing the growth of cells into tissue, recognize that growth needs to occur on multiple length scales. As a result, the proposed tissue scaffold should have hierarchical porosity.[5] Large pores can allow material diffusion, cell penetration and tissue ingrowth. The secondary level pores can provide high specific surface area which facilitates biofactor deposition, as well as surface features that can mimic extracellular matrix.[6, 7]

Polymeric materials in biomedical applications is also being furthered with the push to advance the field of 3D biomaterial printing. 3D biomaterial printing can be a revolutionary technology for its promise to allow for the fabrication of diverse tissue and organ structures via rapid prototyping and great ease for immediate implantation.[8, 9] Through 3D printing, complex structures can be developed via computer-aided design layer-by-layer, such that all aspects of manufacturing are carefully controlled and all aspects of design are intentional.[10] Furthermore, 3D printing is a universal fabrication method, which can be employed for different tissues types to develop the desired mechanical and biological properties through structure design, material choice, and post-printing modifications, such as washing and coating with bioactive components[11]. A material choice is additionally advantageous if it offers tunability, in which the formulation of the material could be altered to establish different properties in the scaffold, without compromising its ability to be successfully 3D printed.

In this study, we explore the possibility of 3D printing a model cocontinuous polymer blend, PLA/PS. Different compositions of polymer blends are explored to evaluate their printability and viability as a scaffold. The goal is to develop a hierarchically porous PLA with versatility in

design, a tunable pore size, and better functional capabilities. Oxazoline-functional PS (PS-OX) was used to reduce the size of the secondary pores.

A1.3 Experimental

A1.3.1 Materials

The material properties of PLA, PS, PS-OX used in this work can be found in Chapter 5, section 5.1.2.

A1.3.2 Twin Screw Extrusion

Filaments of PLA/PS blends were prepared using a PRISM TSE 16 TC twin screw extruder. The screws have a 16 mm diameter, a 25:1 L:D ratio, and co-rotating self-wiping intermeshing elements. All material was dried prior to processing at 40°C for 24 hours. The volume percent compositions were calculated assuming a density of 1.12 g/cm^3 for PLA and a density of 0.983 g/cm^3 for PS and PS-OX. For extrusion, the nozzle was set at 150 °C, with the next two heating zones set at 180 °C. The heating zone prior to the feed zone was set at 175 °C. Finally, the temperature for the feed zone was set at 130 °C. The following compositions were extruded into a filament throughout this study: PLA/PS 40/60 vol.%, PLA/PS 30/70 vol.%, PLA/PS 25/75 vol.%, PLA/PS 80/20 vol.%, PLA/PS-OX 40/60 vol.%, and PLA/PS-OX 70/30 vol.%.

In order to form a filament between 1.25 mm and 1.80 mm in diameter, as required for 3D printing, the roller was placed 17 inches from where the polymer blend exists the nozzle. The beginning and the end of the filament of the blend was always discarded to ensure only filament of proper composition was kept. The roller speed was set between 15 and 25 RPM to achieve a filament of acceptable diameter and was adjusted as needed. The screw rotation speed was set to 12-13 RPM, generally achieving a residence time of around 10 minutes. For the reactive PLA/PS-OX blends, a total residence time of 30 minutes was required for the reaction to complete—

warranting two cycles of processing, with a RPM of 9-11 and a residence time greater than 15 minutes.

A1.3.3 Fused Deposition Modeling (FDM)

FDM of PLA/PS blends was performed on a MakerBot Replicator printer. The targeted filament diameter was 1.5 mm. The thicker filament diameter tended to print better than filament below 1.3 mm. The MakerBot has three different resolutions: high, standard, and low. The resolution refers to the layer thickness in the z direction or the effective layer height. High resolution refers to a 0.1 mm layer height. Standard resolution is a 0.2 mm layer height. And low resolution is a 0.3 mm layer height. A 3D, uniform, open-pore orthogonal "matrix" construct .stl file was downloaded from the freeware website (http://www.thingiverse.com/thing:45228/#files) and modified for printing PLA/PS blends. Three different sizes of scaffolds were successfully printed: 20 × 20 × 20 mm, 15 × 15 × 15 mm, 12.5 × 12.5 ×12.5 mm.

Fused deposition modeling to obtain the as-printed structure establishes the primary porosity of the scaffold. The pore diameter for the 12.5 mm scaffold measures 500-600 μm. The pore diameter for the 15 mm scaffold measures 1-1.1 mm. Finally, the pore diameter for the 20 mm scaffold measures 1.5 mm.

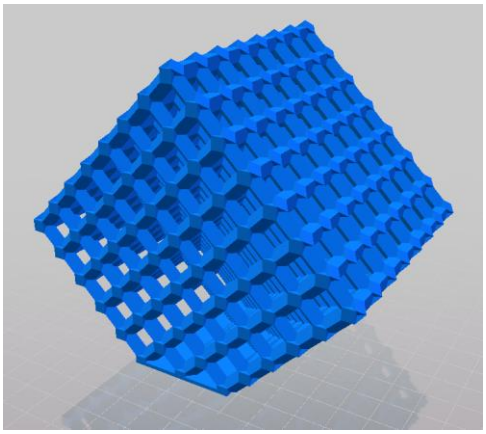

Figure A1-2 Representative .stl image of scaffold structure

A1.3.4 Extraction and PS continuity

PS Extraction from scaffolds and continuity calculation were conducted the same way as 4.2.4.

A1.3.5 Scanning Electron Microscopy

Scanning Electron Microscopy (SEM) was performed on the specimens to analyze the secondary porosity and how consistent the morphology was throughout the material. For the varying compositions, both extracted filaments and extracted scaffolds were imaged. Extracted filaments refer to the filaments pulled during twin screw extrusion that are extracted prior to fused deposition modeling. For filaments, the cross section, inner surface, and outer surface were imaged. For the scaffolds, two different matrix network orientations were imaged. The surface of the deposited filament strands and regions of deposited filament attachment were of particular interest.

A1.3.6 Scaffold Compression Testing

Compression testing of the scaffolds was completed on an Instron 5960 Dual Column Testing System. A 500 N load cell was used with a 1 mm/min rate. There was not an appropriate ASTM procedure for compression testing of a porous object, however ASTM D695 was consulted when preparing for these tests. Gauge length was reset once the load was in contact with the specimen. At least three specimens were run for the 15 mm, standard resolution scaffolds.

A1.3.7 Cell culture experiment

15 mm × 15 mm × 2 mm non-porous plates were printed with neat PLA and different blends. The blend-plates were then made porous by extracting PS phase with cyclohexane. The scaffolds were sterilized with UV light first (15 min / side) and then 70% ethanol solution. The scaffolds were attached to the bottom of polyhydroxyethylmethacrylate (PolyHEMA) coated wells with 3M tissue adhesive. This prevented the hydrophobic porous scaffolds from floating. 0.5 million Fibroblast cells were seeded onto each scaffold. Cells were tracked for 9 days with AlamarBlue Assay dye. Cells uptake the dye and the uptake was measured by recording the

absorbance of the wells. (The higher the number of cells, the more dye that is uptake and the higher the absorbance of the well).

A1.4 Results and discussion

A1.4.1 Fused deposition modeling and PS extraction

A1.4.1.1 Scaffold size and print resolution

As a model study, PLA/PS 40/60 vol.% scaffolds of 20 mm and 15 mm size were printed at high standard, and low resolution. The 15 mm scaffold could not be printed at low resolution. The 20 mm scaffolds could take 1.5 to 2 times the fabrication time in comparison to the 15 mm scaffolds for the high and standard resolutions, as shown in Table A1-1. For the construct shown in Figure A1-2, the minimum scaffold size able to be properly printed with the MakerBot Replicator was found to be 12.5 mm, printed at standard resolution (fabrication time ~15 min). Below 12.5 mm, the printer alters the way in which it prints—neglecting supports in some directions in order to achieve the smaller size. As a result, the smallest attainable primary pore size in this study appears to be 500-600 μm. The 12.5 mm scaffold size can undergo extraction while maintaining the as-printed geometry. Better printing equipment may help achieve smaller primary pore size.

Table A1-1 Effect of printing parameters on cocontinuity for PLA/PS 40/60 vol.% scaffolds.

Scaffold Size (mm)	Resolution	Fabrication Time (min)	Structure integrity after printing?	PS mass loss after extraction (%)
15	Low	20	No	-
15	Standard	20	Yes	82.2 ± 4.0
15	High	40	Yes	86.7 ± 2.1
20	Low	20	Yes	89.1 ± 6.7
20	Standard	30	Yes	88.3 ± 1.7
20	High	65	Yes	82.1 ± 6.8

Table A1-1 also shows the PS continuity of scaffolds with different printing parameters. The “PS mass loss after extraction” is the average of at least three specimens. No clear trend was

identified regarding the effect of printing resolution on PS continuity. Considering the advantages of smaller primary pore size (a good primary pore size can be 0.5 mm)[12 13] in proposed tissue scaffolds in addition to the advantages of rapid fabrication time and equipment limitations, the 15 mm matrix size printed with standard resolution was selected as the primary scaffold construction for the rest this study.

A1.4.1.2 Effect of PS volume fraction on PS extraction

Presented in Table A1-2 is the primary PS extraction data for scaffolds 15 mm in size, printed with standard resolution. 82% of the PS can be extracted from 40/60 vol.% PLA/PS scaffold. In theory, if the immiscible polymer blend was fully cocontinuous, then 100% of the PS could be successfully extracted—so with the 40/60 vol.% PLA/PS, 100% cocontinuity was not established. When PS volume higher than 70%, polystyrene mass loss percentages after extraction increased above 95%, indicating nearly full cocontinuity. Figure A1-3a, b shows the porous scaffold made from 70/30 vol.% PLA/PS blend. The primary structure was successfully retained after extraction of PS.

Table A1-2 Effect of PS volume fraction on PS continuity.

Blend	**PS volume fraction (%)**	**PS Mass Loss (%)**
PLA/PS	60	82.2 ± 4.0
	70	95.1 ± 2.6
	75	99.6 ± 1.7
	80	96.7 ± 0.1
PLA/PS-OX	60	98.2 ± 0.1
	70	97.3 ± 0.7 (collapse)

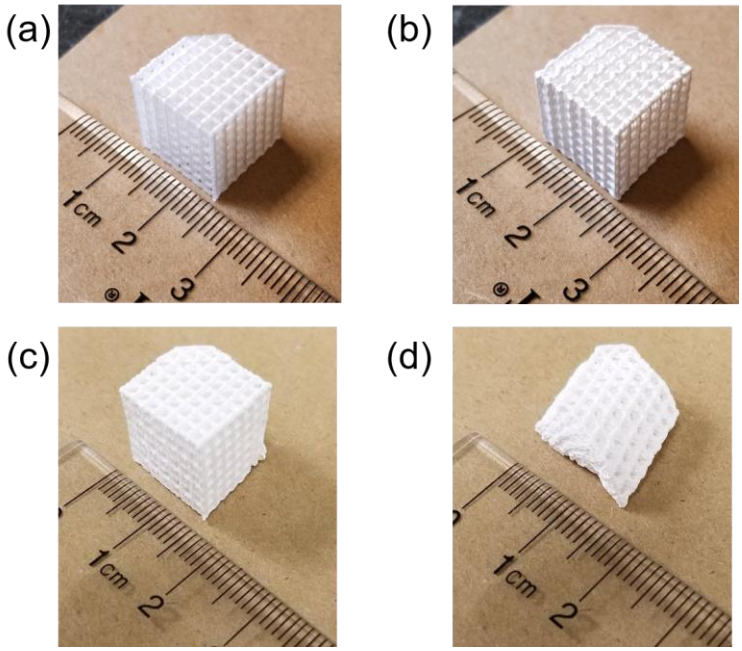

Figure A1-3 Representative images of printed PLA scaffolds. (a) 70/30 vol.% PLA/PS before extracting PS, (b) 70/30 vol.% PLA/PS after extracting PS, (c) 60/40 vol.% PLA/PS-OX after extracting PS, (d) collapsed 70/30 vol.% PLA/PS-OX after extracting PS.

However, 70/30 vol.% PLA/PS-OX scaffold collapsed after extraction of PS-OX (Figure A1-3d). As discussed in Chapter 4.3.2, the graft copolymer formed by reaction of PLA with PS-OX would narrow the cocontinuity range. The morphology of 70/30 vol.% PLA/PS-OX blend possess a large portion of drop-in-matrix characteristics. Interestingly, 60/40 vol.% PLA/PS scaffold maintained its structure after extracting 98% of the PS-OX (Figure A1-3c). Note that only 82% PS can be extracted from 40/60 vol.% PLA/PS scaffold. It seems that for printed scaffolds, graft copolymer shifted the cocontinuity window more than narrowing it.

A1.4.2 Filament morphology

The filaments were first imaged to study the blend morphology. Figure A1-4 presents the cross section morphology of PLA/PS filaments with different compositions. The feature size in the reactive PLA/PS-OX (Figure A1-4b) is smaller than nonreactive PLA/PS (Figure A1-4a), due to

the compatibilization effect of reactively form graft copolymer. The evolution of morphology from Figure A1-4a to Figure A1-4b indicates an increasing degree of co-continuity. If one were to only observe Figure A-4a two-dimensionally-speaking, it would appear to have a droplet-in-matrix morphology, with droplets of PS suspended in a matrix of PLA. However, three-dimensionally-speaking this is certainly not the case due to the amount of PS that was successfully extracted—indicating that there is a high degree of co-continuity. In fact, the PS phase was highly elongated by the extrusion flow (Figure A1-5).

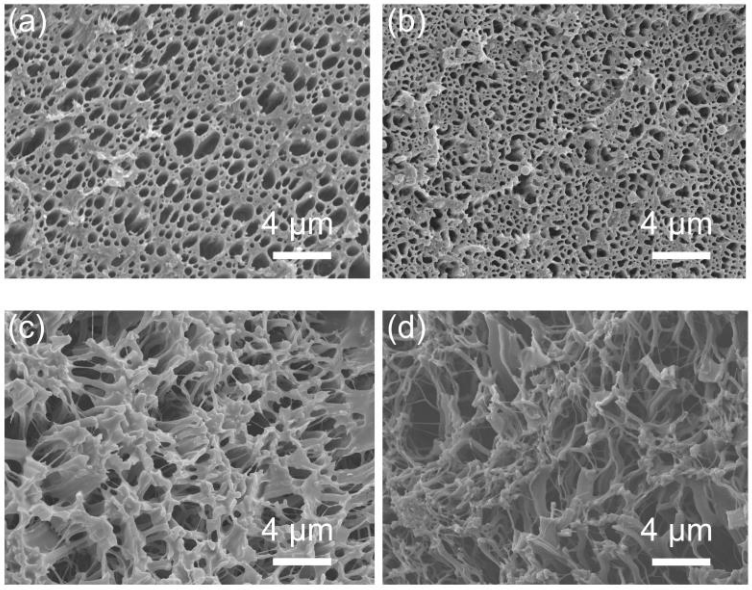

Figure A1-4 Cross section morphology of filaments. (a) 40/60 vol.% PLA/PS, (b) 40/60 vol.% PLA/PS-OX, (c) 30/70 vol.% PLA/PS, (d) 20/80 vol.% PLA/PS. PS phase was extracted.

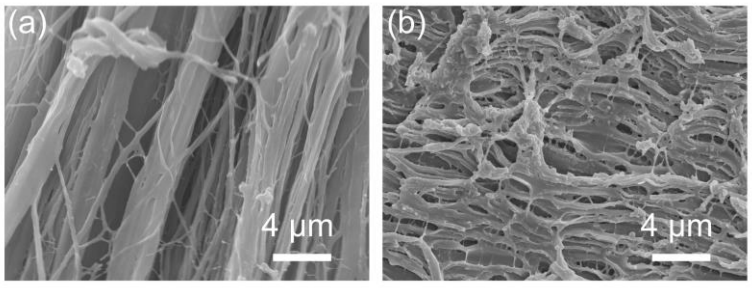

Figure A1-5 Flow direction morphology of extracted filaments. (a) 30/70 vol.% PLA/PS, (b) 40/60 vol.% PLA/PS-OX.

A1.4.3 Scaffold morphology

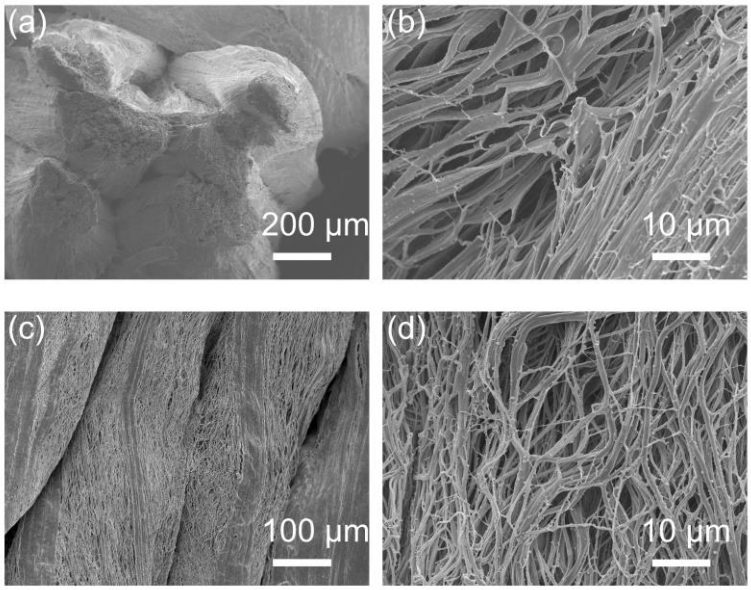

Figure A1-6 Morphology of secondary pores of PLA scaffold. (a) 30/70 vol.% PLA/PS, perpendicular to printing direction, (b) 30/70 vol.% PLA/PS, printing direction, (c) and (d) 40/60 vol.% PLA/PS-OX, printing direction.

Figure A1-6 demonstrates the fibrous and interconnected secondary features of the hierarchically porous PLA. In the region where two printed strands come together, the connection is not seamless. But most of the fibers are fused, which are strong enough to hold the strands together. This interconnected fibrosity appears to be the result of the unidirectional extrusion both to form the filament and to form the scaffold—with the interconnected structure inherited from cocontinous morphology. The fiber size of 40/60 vol.% PLA/PS-OX scaffold is smaller than 30/70 vol.% PLA/PS scaffold because of interfacial reaction.

A1.4.4 Scaffold Compression Testing

Displayed in Table 6 are the maximum compressive stress values for each of the PS – PLA compositions. The strain at which this maximum compressive stress occurred varied greatly, meaning the linear portion of the stress-strain curves also varied specimen by specimen. As a result, the modulus of elasticity for each of the specimens was not calculated. For PLA/PS scaffold, the maximum compression stress decreased with decreasing PLA volume fraction. The PLA/PS-OX specimens had higher maximum compressive stresses in comparison to the PLA/PS specimens. Furthermore, these specimens appeared to have greater rigidity and less elasticity to them after compression in comparison to the PLA/PS specimens.

Table A1-3 Compression results for 15 mm sized scaffolds after extracting PS.

Blend	PS volume fraction (%)	Resolution	Maximum compressive stress (MPa)
PLA/PS	60	High	0.173 ± 0.039
	60	Standard	0.177 ± 0.082
	70	Standard	0.185 ± 0.013
	75	Standard	0.144 ± 0.014
	80	Standard	0.086 ± 0.018
PLA/PS-OX cycle 1	60	Standard	0.377 ± 0.038
PLA/PS-OX cycle 2	60	Standard	0.251 ± 0.019

A1.4.5 Cell experiment

Figure A1-7 shows the trend of cell growth on different scaffolds. The growth on the porous scaffolds are much lower than the on the neat PLA scaffold. The cells didn't survive on porous PLA made from PLA/PS-OX blend. We think the oxazoline functional groups in PS-OX is responsible for killing the cells. For the scaffold from PLA/PS blend, the PS remaining on the surface of porous PLA may have caused the lower growth rate of cell. In the further, we will use PLA/polycaprolactone (PCL) blend instead of PLA/PS blend because PCL is biodegradable and biocompatible.

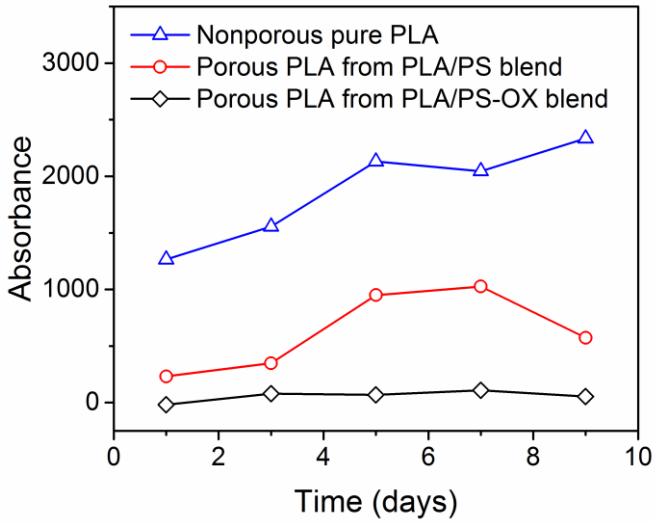

Figure A1-7 Cell growth indicated by well absorbance.

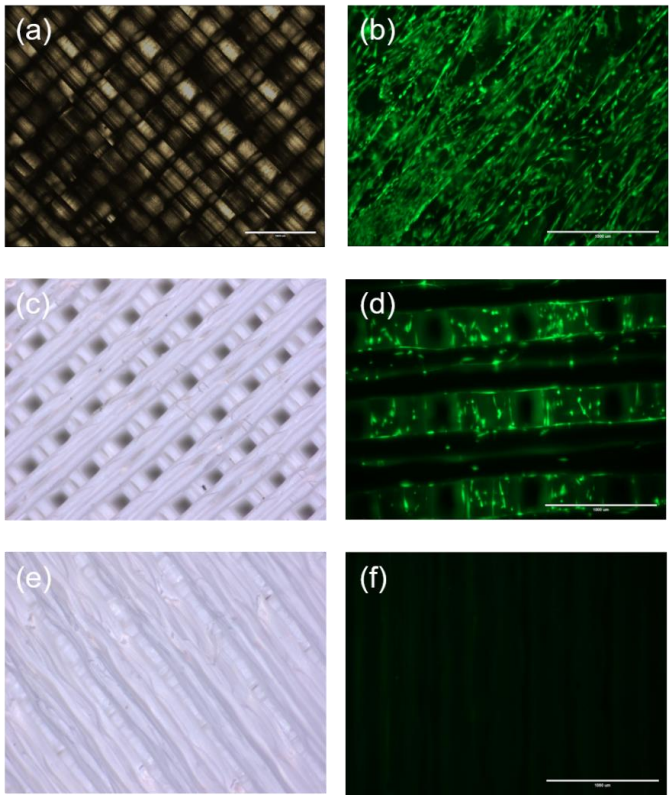

Figure A1-8 Scaffold surface structure (left) and cell attachment results (right). Green indicates living cells. The scale bars represent 1 mm.

A1.5 Conclusions

We demonstrated 3D printing a cocontinuous polymer blends as a new method to prepare hierarchically porous polymer scaffolds. Cocontinuous PLA/PS blend was 3D printed into porous scaffold and after selectively extracting the PS, the scaffold was self-supporting and geometry-retaining with good layer-to-layer attachment. The secondary porosity is fibrous and highly interconnected, with fiber diameter of several microns. This method of fabricating hierarchical porous material is versatile in pore size control. Primary pore can be controled by computer aided design and fused deposition modeling, while the secondary pore can be altered with compatibilization.

A1.6 References

1 S.J. Hollister, Nat. Mater. 4 (2005) 518–524.

2 X. Liu, P.X. Ma, Ann. Biomed. Eng. 32 (2004) 477–486.

3 E. Traversa, B. Mecheri, C. Mandoli, S. Soliman, A. Rinaldi, S. Licoccia, G. Forte, F. Pagliari, S. Pagliari, F. Carotenuto, M. Minieri, P. Di Nardo, J. Exp. Nanosci. 3 (2008) 97–110.

4 M. Jafari, Z. Paknejad, M.R. Rad, S.R. Motamedian, M.J. Eghbal, N. Nadjmi, A. Khojasteh, J. Biomed. Mater. Res. - Part B Appl. Biomater. 105 (2017) 431–459.

5 J.R. Jones, P.D. Lee, L.L. Hench, Philos. Trans. A. Math. Phys. Eng. Sci. 364 (2006) 263–281.

6 J. Wang, B.H. Lessard, M. Maric, B.D. Favis, Polymer. (2014) 1–7.

7 P.A. George, K. Quinn, J.J. Cooper-White, Biomaterials. 31 (2010) 641–647.

8 M. Guvendiren, J. Molde, R.M.D. Soares, J. Kohn, ACS Biomater. Sci. Eng. 2 (2016) 1679–1693.

9 D.H. Rosenzweig, E. Carelli, T. Steffen, P. Jarzem, L. Haglund, Int. J. Mol. Sci. 16 (2015) 15118–15135.

10 L. F. Francis, Materials Processing: A Unified Approach to Processing of Metals, Ceramics and Polymers. (2016) San Diego, CA: Elsevier.

11 A.E. Jakus, A.L. Rutz, R.N. Shah, Biomed. Mater. 11 (2016) 14102.

12 V. Karageorgiou, D. Kaplan, Biomaterials. 26 (2005) 5474–5491.

13 A.C. Jones, C.H. Arns, A.P. Sheppard, D.W. Hutmacher, B.K. Milthorpe, M.A. Knackstedt, Biomaterials. 28 (2007) 2491–2504.

Appendix 2 Supplementary figures for Chapter 5

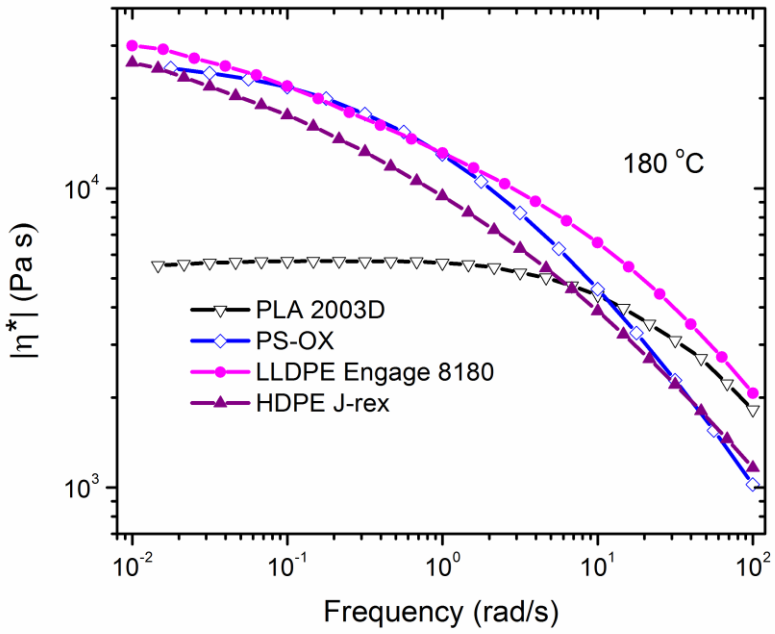

Figure A2-1 Complex viscosities of LLDPE (Engage 8180) and HDPE (J-rex HD KF 251A) at 180℃. LLDPE showed a higher viscosity than PLA and both PSs at the relevant mixing shear rate, ~85 s^{-1}.

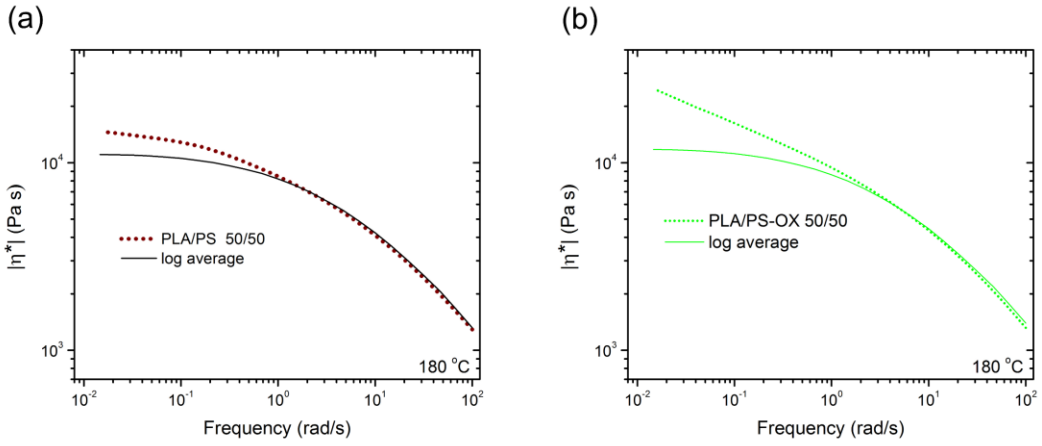

Figure A2-2 Complex viscosities of (a) PLA/PS 50/50 vol.% blend and (b) PLA/PS-OX 50/50 vol.% blend, after 30 min mixing. The solid lines show the log volume average viscosities η_{av}, given by[1, 2]

$$\log(\eta_{av}) = \phi_1 \log(\eta_1) + \phi_2 \log(\eta_2)$$

where ϕ_i and η_i are the volume fractions and viscosities of the two components. The log average viscosities of both blends are in good agreement with the measured blend viscosities at frequency above 1 s^{-1}. In the low frequency region, the complex viscosity of the blends was higher than log average because the interfacial elastic stress contribution was significant.[3]

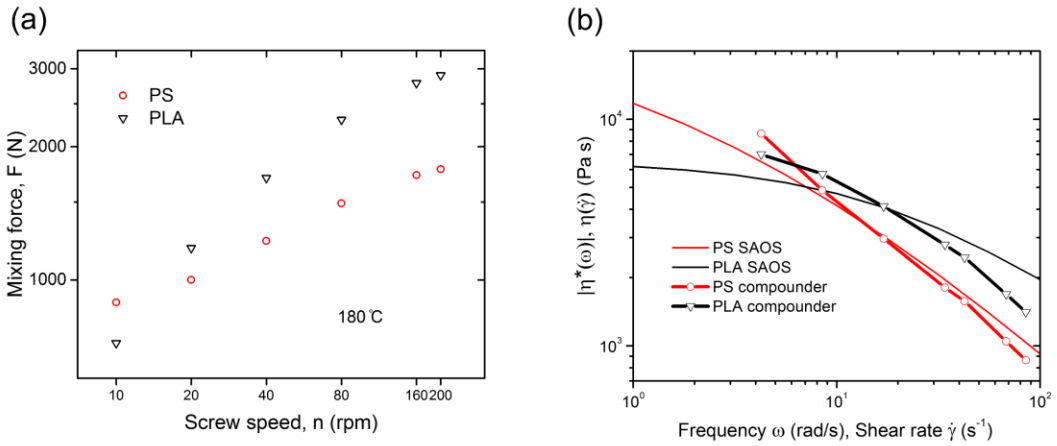

Figure A2-3 (a) Compounder mixing force F as a function of screw speed n for PS and PLA, (b) shear viscosity calculated by[4, 5]

$$\dot{\gamma} = \frac{n}{c_1}$$

$$\eta\,(\dot{\gamma}) = c_2 \frac{F}{n}$$

where $\dot{\gamma}$ defines the average shear rate in the mixing chamber, c_1 and c_2 are constants dependent on compounder geometry and polymer loading. For the Xplore MC5 compounder used in this study, $c_1 = 2.35$ *(rpm) s* and $c_2 = 97$ *(Pa s) (rpm)* N^{-1} at polymer loading of 4 ml. The viscosity estimation from mixing force agrees with small amplitude oscillatory shear (SAOS) results. This supports our claim that at 200 rpm, the average shear rate in the mixing is ~85 s^{-1}.

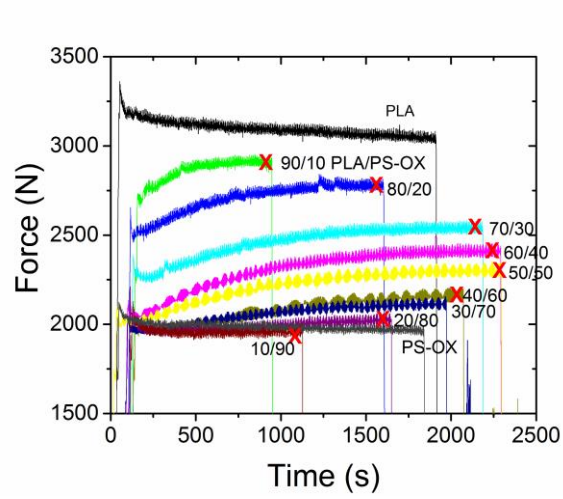

Figure A2-4 Mixing force as a function of mixing time for PLA/PS-OX blends. Polymer loadings were 4 mL in all case. The plateau times plotted in Figure 3a are marked with X.

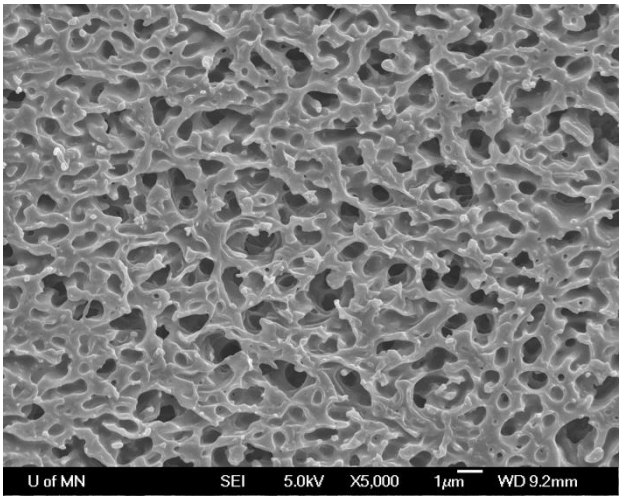

Figure A2-5 Quenched morphology of 50/50 vol.% PLA/PS-OX mixed for 30 min. PS-OX was removed by cyclohexane.

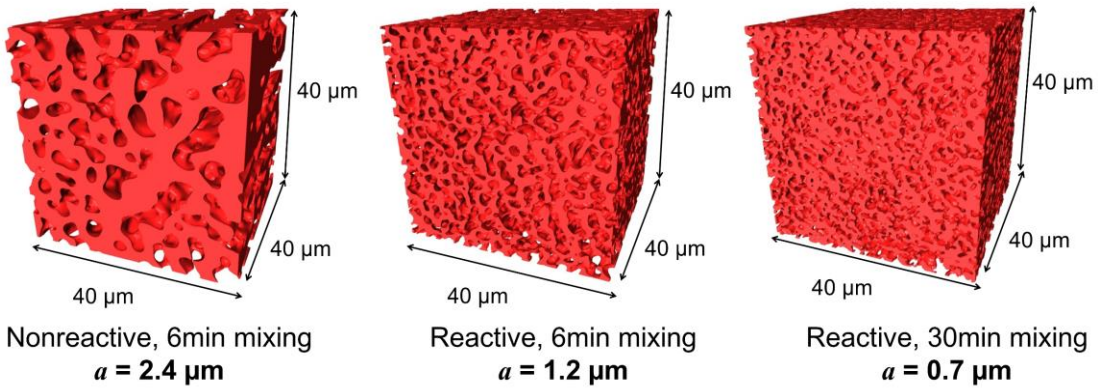

Figure A2-6 3D reconstruction from LSCM images of porous PLA from cocontinuous blends annealed for 3 min. From left to right: 50/50 vol.% PLA/PS mixed for 6 min, 50/50 vol.% PLA/PS-OX mixed for 6 min, 50/50 vol.% PLA/PS-OX mixed for 30 min.

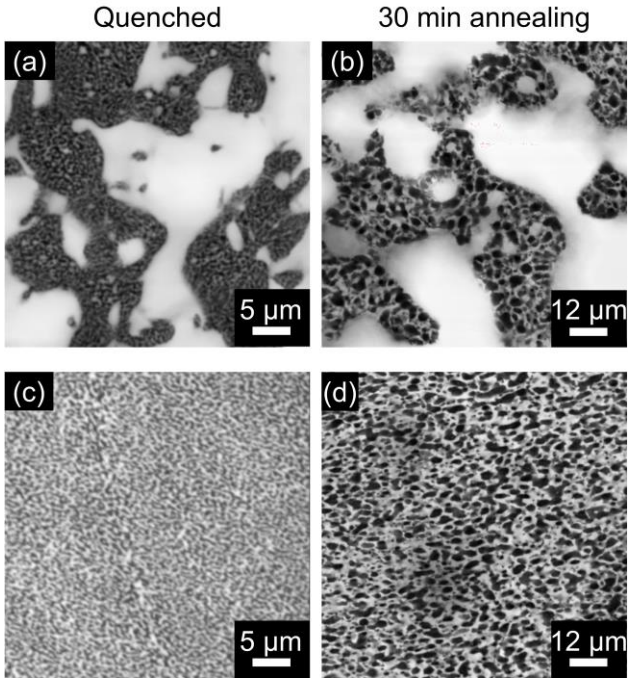

Figure A2-7 LSCM images of (a), (b) 30/30/40 vol.% PLA/PS-OX/LLDPE and (c), (d) 50/50 vol.% PLA/PS-OX blend. The secondary pores in (a) are not as clear as (c) because the primary pores are

much brighter under LSCM. It is evident that the size of secondary pores in (a) and (c) are similar, likewise for the secondary pores in (b) and (d).

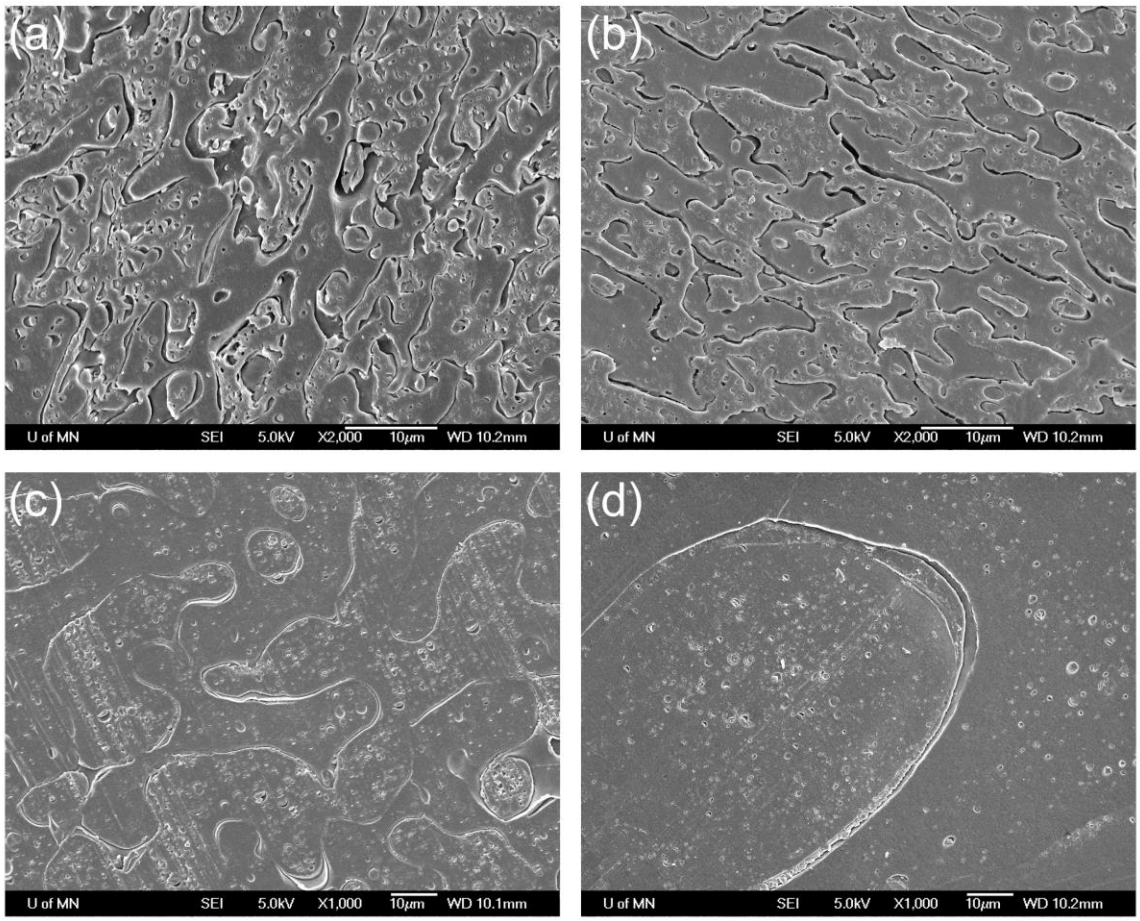

Figure A2-8 Morphology of 45/10/45 vol.% HDPE/PS/PLA blends after (a) 0 min, (b) 3 min, (c) 10 min, and (d) 30 min annealing at 180 °C. PS was washed away with cyclohexane in (a) and (b), but not in (c) and (d). The PS layer between PLA and PE phases can be identified in (d) due to its poor adhesion.

References

1. L.A. Utracki, Melt flow of polymer blends, Polym. Eng. Sci. 23 (1983) 602–609.

2. L.A. Utracki, On the viscosity-concentration dependence of immiscible polymer blends, J. Rheol. 35 (1991) 1615–1637.

3. C.R. López-Barrón, C.W. Macosko, Rheological and morphological study of cocontinuous polymer blends during coarsening, J. Rheol. 56 (2012) 1315.

4. http://www.xplore-together.com/products/software/rheological Accessed on 8/4/2017.

5. M. Maric, C.W. Macosko, Improving polymer blend dispersion in mini-mixers, Polym. Eng. Sci. 41 (2001) 118–130